DTIC FILE COPY ①

AD-A196 820

REPORT DOCUMENTATION PAGE		READ INSTRUCTIONS BEFORE COMPLETING FORM
1. REPORT NUMBER AFIT/CI/NR 88-99	2. GOVT ACCESSION NO.	3. RECIPIENT'S CATALOG NUMBER
4. TITLE (and Subtitle) A COMPUTATIONAL STUDY OF COHERENT STRUCTURES IN THE WAKES OF TWO-DIMENSIONAL BLUFF BODIES		5. TYPE OF REPORT & PERIOD COVERED MS THESIS
		6. PERFORMING ORG. REPORT NUMBER
7. AUTHOR(s) JEFFREY ALAN PEARCE		8. CONTRACT OR GRANT NUMBER(s)
9. PERFORMING ORGANIZATION NAME AND ADDRESS AFIT STUDENT AT: TEXAS TECH UNIVERSITY		10. PROGRAM ELEMENT, PROJECT, TASK AREA & WORK UNIT NUMBERS
11. CONTROLLING OFFICE NAME AND ADDRESS		12. REPORT DATE 1988
		13. NUMBER OF PAGES 122
14. MONITORING AGENCY NAME & ADDRESS(If different from Controlling Office) AFIT/NR Wright-Patterson AFB OH 45433-6583		15. SECURITY CLASS. (of this report) UNCLASSIFIED
		15a. DECLASSIFICATION, DOWNGRADING SCHEDULE

16. DISTRIBUTION STATEMENT (of this Report)

DISTRIBUTED UNLIMITED: APPROVED FOR PUBLIC RELEASE

DTIC
ELECTE
AUG 0 4 1988
S H D

17. DISTRIBUTION STATEMENT (of the abstract entered in Block 20, If different from Report)

SAME AS REPORT

18. SUPPLEMENTARY NOTES

19. KEY WORDS (Continue on reverse side if necessary and identify by block number)

20. ABSTRACT (Continue on reverse side if necessary and identify by block number)

ATTACHED

ABSTRACT

The periodic shedding of vortices from bluff bodies was first recognized in the late 1800's. Currently, there is great interest concerning the effect of vortex shedding on structures and on vehicle stability. In the design of bluff structures which will be exposed to a flow, knowledge of the shedding frequency and the amplitude of the aerodynamic forces is critical. The ability to computationally predict parameters associated with periodic vortex shedding is thus a valuable tool.

In this study, the periodic shedding of vortices from several bluff body geometries is predicted. The study is conducted with a two–dimensional finite–difference code employed on various grid sizes. The effects of the grid size and time step on the accuracy of the solution are addressed. Strouhal numbers and aerodynamic force coefficients are computed for all of the bodies considered and compared with previous experimental results.

Results indicate that the finite–difference code is capable of predicting periodic vortex shedding for all of the geometries tested. Refinement of the finite–difference grid was found to give little improvement in the prediction; however, the choice of time step size was shown to be critical. Predictions of Strouhal numbers were generally accurate, and the calculated aerodynamic forces generally exhibited behavior consistent with previous studies.

vi

A COMPUTATIONAL STUDY OF COHERENT STRUCTURES IN THE

WAKES OF TWO-DIMENSiONAL BLUFF BODIES

by

JEFFREY ALAN PEARCE, B.S. in Aerospace Engr.
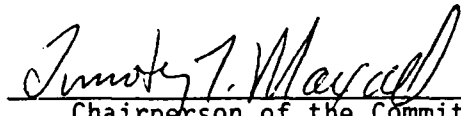
A THESIS

IN

MECHANICAL ENGINEERING

Submitted to the Graduate Faculty
of Texas Tech University in
Partial Fulfillment of
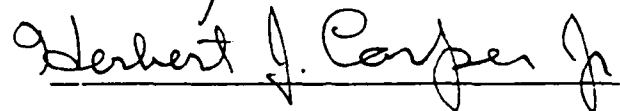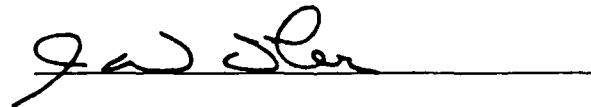the Requirements for
the Degree of

MASTER OF SCIENCE

IN

MECHANICAL ENGINEERING

Approved

_____
Chairperson of the Committee

_____

_____

Accepted

_____
Dean of the Graduate School

August, 1988

ACKNOWLEDGEMENTS

I would like to thank the following persons and organizations for their support. Foremost I would like to thank my advisor, Dr. Timothy T. Maxwell, for his constant support and knowledgeable input. I also wish to thank the other members of my committee, Dr. J. Walt Oler and Dr. Herbert J. Carper, for their support. I am also grateful to Dr. S. Parameswaran for his constant concern and help.

I owe thanks to the United States Air Force and the Air Force Institute of Technology for giving me the opportunity to pursue a graduate degree. Finally, I would like to thank my wife Maryann for her constant, loving, and unconditional support.

TABLE OF CONTENTS

ABSTRACT

The periodic shedding of vortices from bluff bodies was first recognized in the late 1800's. Currently, there is great interest concerning the effect of vortex shedding on structures and on vehicle stability. In the design of bluff structures which will be exposed to a flow, knowledge of the shedding frequency and the amplitude of the aerodynamic forces is critical. The ability to computationally predict parameters associated with periodic vortex shedding is thus a valuable tool.

In this study, the periodic shedding of vortices from several bluff body geometries is predicted. The study is conducted with a two–dimensional finite–difference code employed on various grid sizes. The effects of the grid size and time step on the accuracy of the solution are addressed. Strouhal numbers and aerodynamic force coefficients are computed for all of the bodies considered and compared with previous experimental results.

Results indicate that the finite–difference code is capable of predicting periodic vortex shedding for all of the geometries tested. Refinement of the finite–difference grid was found to give little improvement in the prediction; however, the choice of time step size was shown to be critical. Predictions of Strouhal numbers were generally accurate, and the calculated aerodynamic forces generally exhibited behavior consistent with previous studies.

LIST OF TABLES

LIST OF FIGURES

NOMENCLATURE

a_i	constants
$a_E,\ a_N,\ a_S,\ a_W$	finite-difference coefficients
A	frontal area
b	source term
c	length of rectangular cylinder
C_D	nondimensional drag coefficient
C_L	nondimensional lift coefficient
C_p	pressure coefficient
C_{ps}	base pressure coefficient
d	characteristic length
d'	wake width
D	drag force
E_T	internal energy
g_h	function dependent on λ
h	height of plate above the ground plane
k	kinetic energy of turbulence
l	plate or cylinder height
L	lift force

M	number of cells in a horizontal wall
n	shedding frequency
N	number of cells in a vertical wall
p	static pressure
p_∞	freestream static pressure
P	shedding period
q_∞	dynamic pressure
Q	added heat
R	specific gas constant
Re	Reynolds number
St	Strouhal number
St_∞	function dependent on Re
t	time
Δt	time step
T	temperature
u	x component of velocity
u_{rel}	relative velocity of vortices
U_s	separation velocity
U_∞	freestream velocity
v	y component of velocity
$\mathbf{v}$	velocity vector
w	z component of velocity
W	work done by the system
X	x direction body force

Y	y direction body force
Z	z direction body force
α	relaxation factor
β	aspect ratio of rectangular cylinder
ϵ	dissipation rate of turbulence energy
κ	ratio of U_s to U_∞
λ	ratio of h to l
μ	dynamic viscosity
ρ	density
τ	shear stress
ϕ	general variable

CHAPTER I

INTRODUCTION

Formal recognition of the periodic structures existing in the wakes of bluff bodies is credited to Strouhal. In his now famous work of 1878, Strouhal determined that the shedding of vortices behind a body occurred periodically, and he also gave a crude approximation for the frequency of the vortex shedding. Soon after in 1879, Rayleigh discovered a relationship between the shedding frequency and the flow Reynolds number. However, the most famous contributions to the field of periodic structures in bluff body wakes is credited to von Kármán. Von Kármán formulated a theory on the flow pattern that occurs in the wakes of bluff bodies, that pattern being the familiar Kármán vortex street (Figure 1.1). His theory attempted to predict the geometry of the flow pattern in the wake behind a body as well as other vital parameters, such as the velocity of the vortices and the drag on the body. Though his theory is not complete in that it concentrates only on the wake region and subsequently ignores the exterior potential flow, it is nonetheless a significant contribution to the study of coherent structures in bluff body wakes.

Importance of Vortex Shedding

These pioneering efforts in the study of periodic structures in wakes have many valuable applications. Though the study of the vortex street is essentially a problem

1

in fluid dynamics, its primary applications are related to structural mechanics. Since the vortex street is periodic in nature, the aerodynamic loads on a body which is shedding vortices are also periodic. The frequency of the vortex shedding is a critical parameter, for if the shedding frequency approaches a natural frequency of the structure, potentially damaging large amplitude oscillations can occur. A vivid demonstration of the damaging effects of vortex shedding was provided by the destruction of the Tacoma Narrows Bridge in 1940 (Polodny and Scalzi 1976). In a matter of hours, this bridge was destroyed by the oscillations induced by the periodic shedding of vortices from the bridge's surface.

In line with this example, the study of vortex shedding is important in the design of structures that will be subjected to wind loadings. Also, there is an analog in marine structures, where vortex shedding is a matter of considerable interest. Another field of recent interest is the effect of vortex shedding on the stability of motor vehicles with bluff tail sections. In general, any bluff body subjected to a fluid flow can potentially shed vortices; knowledge of the frequency and amplitude of the associated loading can be vital to stability and structural integrity.

Value of Computational Analysis

The ability to predict various parameters associated with vortex shedding can be of great value. For structures which will be subjected to fluid flow, the possibility of damage due to vortex–induced loading must be considered. Though one could attempt to measure the vortex shedding characteristics experimentally, the ability to do so computationally has many advantages.

The advantages of computational studies are often based on monetary considerations. One fundamental advantage of computational methods is the ability to

construct and test many configurations relatively quickly and inexpensively. The use of fine grids in calculations allows one to achieve a highly detailed picture of the flow field, and greater detail can be achieved by simply refining the grid. In an experimental study, determining complex flow fields may require time consuming testing, which inevitably leads to great expense. In many cases, computer codes have the ability to predict flow in regions of a flow field that are inaccessible by experimental methods.

This study treats the problem of vortex shedding with a two-dimensional finite-difference code. A three-dimensional code is not used for several reasons. First, there was no three-dimensional code available for this study. Also, the addition of another dimension to the calculation domain would greatly increase computer run time. Furthermore, since the primary objective of the study is to simply demonstrate the ability to numerically predict vortex shedding, the added complexity of a third dimension is unnecessary.

Objectives of the Study

The primary objective of this study is to demonstrate the ability of a finite-difference code to predict periodic vortex shedding from various geometries. To demonstrate the abilities of the code, the phenomena of vortex shedding is considered for three basic flow schemes. The three basic schemes consist of the following: a flat plate in a uniform flow which is oriented normal to the plate (Figure 1.2(a)), a flat plate near a ground plane in a uniform flow which is oriented normal to the plate (Figure 1.2(b)), and a rectangular cylinder in a uniform flow which is oriented normal to the cylinder (Figure 1.2(c)). The dependence of the results on the choice of finite-difference grid size, turbulence, and time step size are also examined.

Data for the comparison of computational and experimental results comes from various sources. For the shedding from a flat plate in a open region, the parameters used for the comparison are shedding frequency, drag and lift coefficients, and wake pressure profiles. Experimental data for comparison comes primarily from work by Roshko (1954). For the case of a flat plate near a ground plane, the primary interest is the prediction of shedding frequency. Experimental results are provided by the studies of Strickland et al. (1980) and Matty (1979). Finally, the study of vortex shedding from a rectangular body concerns the prediction of the shedding frequency and the drag coefficient. Data for comparison is extracted from work by Okajima (1982) and Davis and Moore (1982).

FIGURE 1.1: Kármán Vortex Street (Van Dyke 1982).

$$U_\infty \longrightarrow$$

(a) Flat Plate in a Uniform Flow.

$$U_\infty \longrightarrow$$
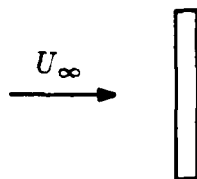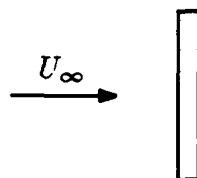
(b) Flat Plate Near a Ground Plane in a Uniform Flow.

$$U_\infty \longrightarrow$$
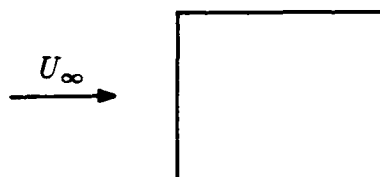
(c) Rectangular Cylinder in a Uniform Flow.

FIGURE 1.2: Basic Flow Configurations.

CHAPTER II

THEORY OF VORTEX SHEDDING

The subsequent discussion covers the aspects of vortex shedding which are relevant to the current study. The basic mechanism of periodic vortex shedding is discussed along with a review of experimental results for each of the three geometries studied. The experimental results presented provide a basis for comparison with the numerical p;edictions.

Basic Parameters

The study of vortex shedding is simplified by the introduction of a number of dimensionless parameters. Several parameters are defined to nondimensionalize the aerodynamic forces, pressure, and vortex shedding frequency.

The fundamental aerodynamic forces known as drag and lift are typically given in a nondimensional form. The nondimensional forms of drag and lift are respectively the drag coefficient, C_D, and the lift coefficient, C_L. Definitions of C_D and C_L are given respectively as

$$C_D = \frac{D}{q_\infty A} \tag{2.1}$$

$$C_L = \frac{L}{q_\infty A} \tag{2.2}$$

7

where

A = frontal area

D = drag force

L = lift force

q_∞ = dynamic pressure.

The dynamic pressure is defined as

$$q_\infty = \frac{1}{2}\rho U_\infty^2 \qquad (2.3)$$

where

U_∞ = freestream velocity

ρ = density.

Pressures are nondimensionalized by introducing the pressure coefficient, C_p, defined as

$$C_p = \frac{p - p_\infty}{q_\infty} \qquad (2.4)$$

where

p = static pressure

p_∞ = freestream static pressure.

Note that $C_p > 0$ indicates that the pressure is greater than freestream pressure, and $C_p < 0$ indicates that the pressure is less than freestream pressure.

Another nondimensional quantity often associated with flow problems is the Reynolds number, Re. The Reynolds number expresses the ratio of inertial to viscous forces and is defined as

$$Re = \frac{\rho U_\infty d}{\mu} \qquad (2.5)$$

where

$d =$ characteristic length

$\mu =$ dynamic viscosity.

The final parameter to introduce is the Strouhal number, St. The Strouhal number is a nondimensional frequency, and it is the primary quantity in the study of vortex shedding. The Strouhal number is defined as

$$St = \frac{nd}{U_\infty} \qquad (2.6)$$

where n is the shedding frequency.

Vortex Formation from Bluff Bodies

A bluff body in a uniform flow can assume two different flow patterns in its wake. At very low Reynolds numbers ($Re < 60$) a stationary, symmetric vortical pattern is formed. This symmetric pattern is a seemingly trivial solution, because it can only be achieved under controlled situations. The solution of interest is the formation of a vortex street in the wake of the body.

The mechanism of wake formation is described similarly by Younis (1988) and Roshko. At the sharp leading edges of the body the flow separates, creating free shear layers. These shear layers continue downstream for a short distance before rolling up into vortices. This flow pattern is inherently unstable, and thus oscillations in the flow field are initiated. Eventually, the vortices from the top and bottom surfaces will alternately be carried downstream forming the familiar pattern of the Kármán vortex street.

Roshko derived certain qualitative relationships pertaining to bluff body wakes. He noted that all bluff body wakes are similar in structure, with the bluffness of a body being related to the dimension of the wake width with respect to the body. In essence, a bluffer body diverges the flow more extensively and creates a larger wake. He also noted an inverse relationship between the shedding frequency and the wake width, indicating that bluffer bodies have lower shedding frequencies. Finally, he noted that a decrease in wake width is accompanied by an increased drag.

Vortex Shedding from a Flat Plate

The shedding of vortices from bluff bodies was studied extensively by Roshko. Among the bodies Roshko studied was the flat plate. Of primary interest was the measurement of shedding frequency from the plate in terms of the Strouhal number. He determined that the Strouhal number for a flat plate remained nearly constant over a wide range of Reynolds numbers. The value of the Strouhal number for a flat plate fell in the range of $0.130 \leq St \leq 0.140$. Experimental Strouhal numbers determined by Roshko are provided as Figure 2.1.

Also of interest was the prediction of aerodynamic forces on the plate, especially drag. Roshko devised a method by which he could determine the drag on a flat plate from one experimental measurement, the base pressure coefficient. He joined the work of Kirchhoff and von Kármán in what was termed the notched–hodograph theory (Roshko 1953). The geometry employed in the notched–hodograph theory is presented in Figure 2.2, with the free streamlines representing the separated shear layers.

The velocity U_s is the separation velocity and is a multiple of the freestream velocity by the relation

$$U_s = \kappa U_\infty \quad . \tag{2.7}$$

Since the velocity U_s exists on the downwind side of the plate, the base pressure coefficient, C_{ps}, is simply

$$C_{ps} = 1 - \kappa^2 \quad . \tag{2.8}$$

To determine κ, the relationship is transformed to read

$$\kappa = \sqrt{1 - C_{ps}} \quad . \tag{2.9}$$

The constant κ is related to the wake width by the curve given as Figure 2.3. Another relation was formed between the relative velocity of the vortices, u_{rel}, and the freestream velocity as

$$\frac{u_{rel}}{U_\infty} = \frac{1}{2} \left(1 \pm \sqrt{1 - \frac{\kappa^2}{2\sqrt{2}}} \right) \quad . \tag{2.10}$$

Finally, the drag can be calculated by the Kármán drag formula

$$C_D = \frac{d'}{l} \left[5.65 \frac{u_{rel}}{U_\infty} - 2.25 \left(\frac{u_{rel}}{U_\infty} \right)^2 \right] \quad . \tag{2.11}$$

The data provided by Roshko for C_{ps} yields drag coefficients in the neighborhood of 1.85.

Vortex Shedding from a Flat Plate
Near a Ground Plane

The study of vortex shedding from a body situated near a ground plane seems to have been exclusively addressed by the related studies of Matty and Strickland

et al. Their study was motivated by a concern about the effects of vortex shedding from heliostats. Though the actual geometry that they were concerned with was not a flat plate, they addressed their concern by performing wind tunnel tests on a flat plate near a ground plane. The basic configuration involved in the study is shown in Figure 2.4.

Their study intended to determine the Strouhal number as a function of the Reynolds number and the height of the plate above the ground plane. Shedding frequencies were determined for the three–dimensional flat plate, and the data they obtained are presented in Figure 2.5. From these data, an equation was derived that approximates the Strouhal number in terms of the dimensionless parameters Re and λ, where

$$\lambda = h/l \quad . \tag{2.12}$$

The equation derived from the study took the following form:

$$St(Re, \lambda) = g_h(\lambda) St_\infty(Re) \quad . \tag{2.13}$$

Their derivation gave the Strouhal number as the product of two independent functions. The function $g_h(\lambda)$ describes the variation in Strouhal number for changes in λ. The function $g_h(\lambda)$ is given as

$$g_h = 1 + a_1 e^{-a_2 \lambda} \sin[a_3(a_4 \lambda - 1)] \tag{2.14}$$

where a_i are constants given as

$$a_1 = \quad 0.518$$

$$a_2 = \quad 4.6$$

$$a_3 = \quad 18.0°$$

$$a_4 = \quad 20.0.$$

A graphical representation of the function $g_h(\lambda)$ is provided as Figure 2.6.

The function $St_\infty(Re)$ is representative of the variation in the Strouhal number with Reynolds number for a flat plate removed from the ground plane. Analytically, the function $St_\infty(Re)$ is given by the simple expression

$$St_\infty = a_5 + a_6/Re \qquad (2.15)$$

where

$$a_5 = \quad 0.121$$

$$a_6 = \quad 407.$$

This function is shown graphically as Figure 2.7. It is important to note that this function was derived for the specific Reynolds number range of $1.4 \times 10^4 \leq Re \leq 1.5 \times 10^5$.

There are a few important features to note about the function $St(Re, \lambda)$. Increasing Reynolds number is accompanied by a decrease in the Strouhal number as indicated by $St_\infty(Re)$. With respect to the function $g_h(\lambda)$, for $0 \leq \lambda < 0.20$ the tendency is for the Strouhal number to increase with increasing λ. For $0.20 \leq \lambda < 0.50$, the Strouhal number decreases for increasing λ. Finally, for $\lambda \geq 0.50$, the Strouhal number appears to be virtually unaffected by the presence of the ground plane.

Vortex Shedding From Rectangular Cylinders

From a practical viewpoint, the rectangular cylinder is a body of considerable interest. Vortex shedding from rectangular bodies is applicable to flows around

automobiles, buildings, and many other bodies of practical interest. These bodies also exhibit interesting behavior with relation to their characteristics while shedding vortices.

The more curious aspects of vortex shedding from rectangular cylinders are related to the Strouhal numbers of such bodies. The basic geometry of the rectangular cylinder is provided as Figure 2.8. The ratio of c/l, which is a critical parameter in determining the characteristics of the flow about a given cylinder, is denoted as β. Okajima provided plots of the variation in Strouhal number with Reynolds number for four values of β ($\beta = 1, 2, 3, 4$). These plots (Figures 2.9–2.12) demonstrate the interesting behavior apparent in the shedding frequency.

For the case $\beta = 1$ (Figure 2.9), there is some variation in the Strouhal number for increasing Reynolds number, but the variation is gradual. However, for the cases of $\beta = 2$ (Figure 2.10) and $\beta = 3$ (Figure 2.11), the behavior is quite different. For $\beta = 2$, there is a discontinuity in the plot at $Re \approx 500$ and a similar discontinuity appears in the plot for $\beta = 3$ at $Re \approx 800$. This discontinuity appears because there are actually two modes of vortex shedding which occur from rectangular cylinders in the range of $2 \leq \beta \leq 3$ (Okajima).

The first mode, which occurs at low Reynolds numbers, is characterized by a reattachment of the flow which separates at the leading edge. The reattached flow then separates at the trailing edge and forms the vortex street. As the Reynolds number is increased, the flow loses the ability to reattach to the surface of the cylinder. Finally, when the Reynolds number reaches a critical value, the separated regions suddenly detach from the surfaces creating a drastic increase in the wake width. As demonstrated by Roshko, an increase in the wake width is accompanied

by a decrease in the shedding frequency. Therefore, this detachment characterizes the second mode of the vortex shedding and is the physical process responsible for the discontinuities which occur in plots for Strouhal number versus Reynolds number.

With respect to the variation in aerodynamic forces on rectangular cylinders, some general trends have been recognized. A study by Davis and Moore indicated an increase in lift and drag for an increase in Reynolds number. Laneville and Yong (1983) were concerned with the variation in the drag for changing β. Their data indicate that the drag increases steadily with increasing β for $\beta < 0.8$. However, for $\beta > 0.8$ the trend suddenly changes and increasing β is accompanied by a decrease in the drag coefficient.
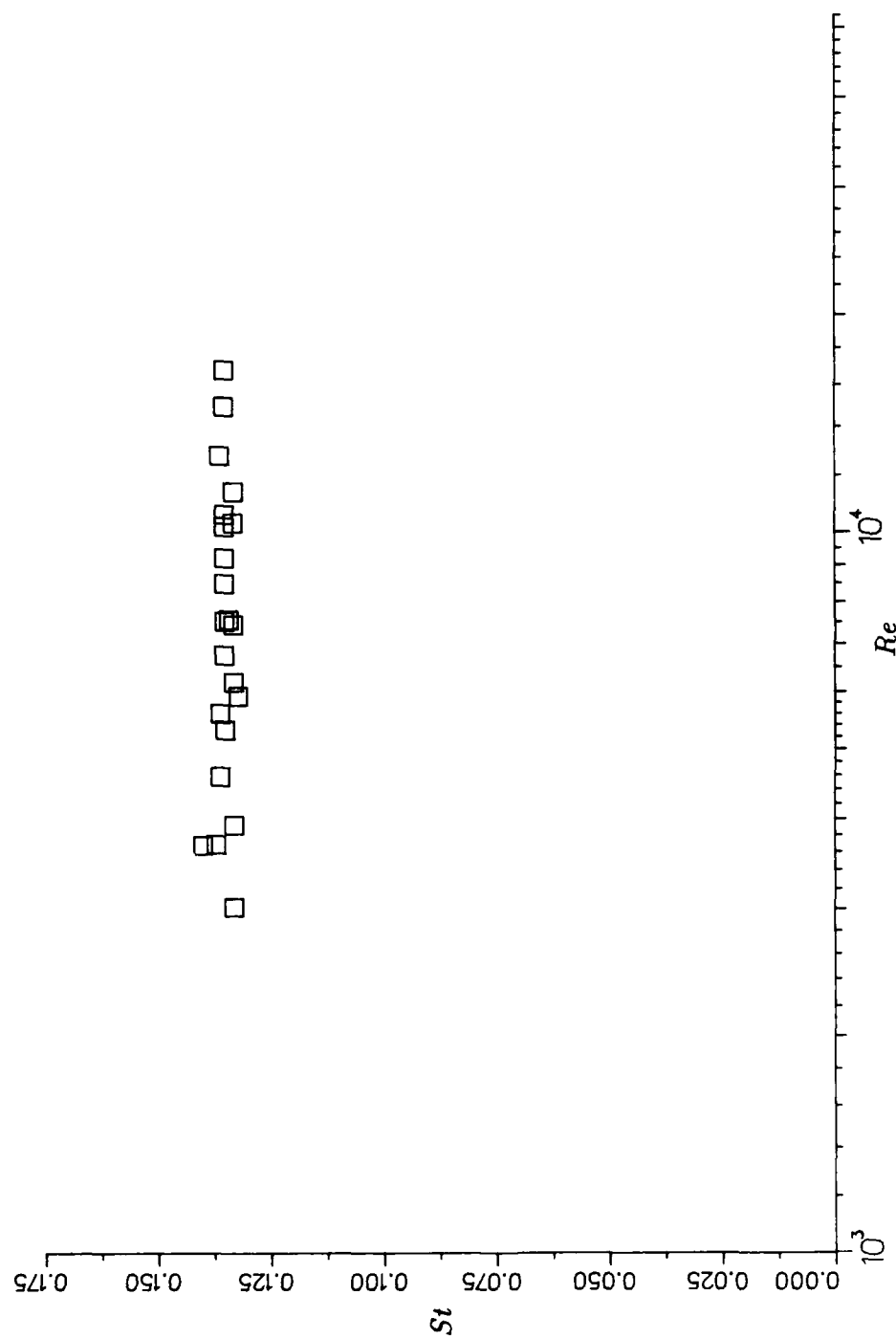
FIGURE 2.1: Strouhal Number vs. Reynolds Number for a Flat Plate (Roshko 1954).
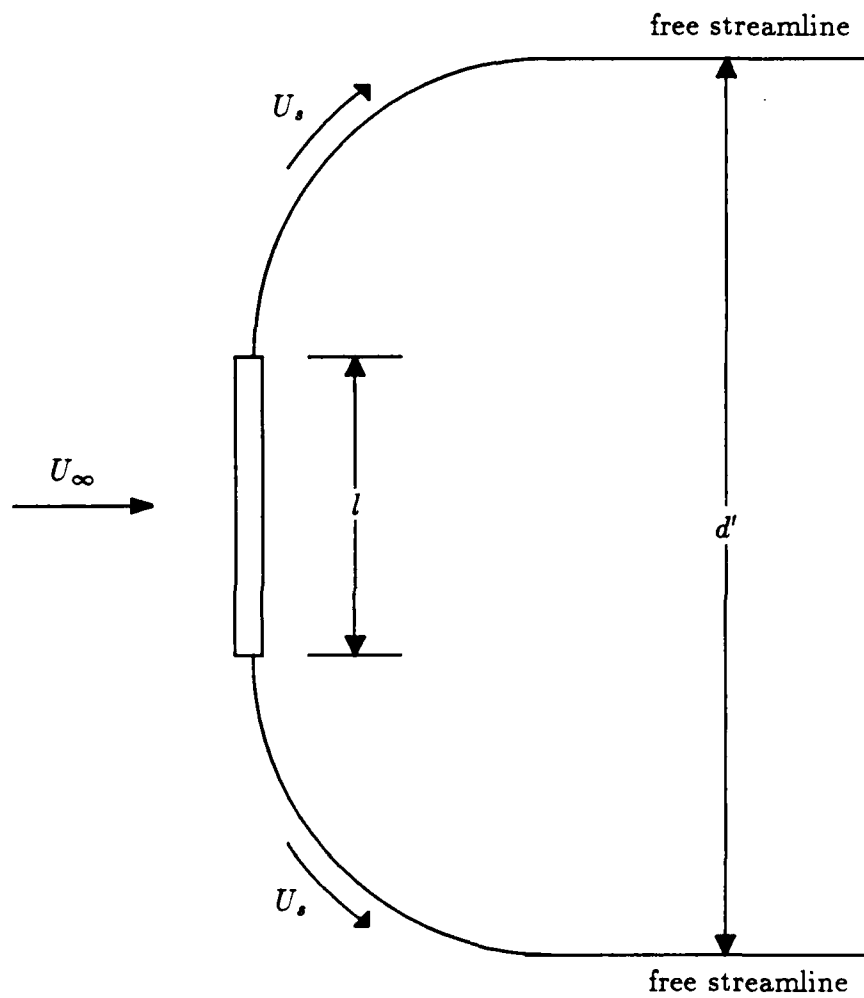
FIGURE 2.2: Geometry for the Notched–Hodograph Theory.
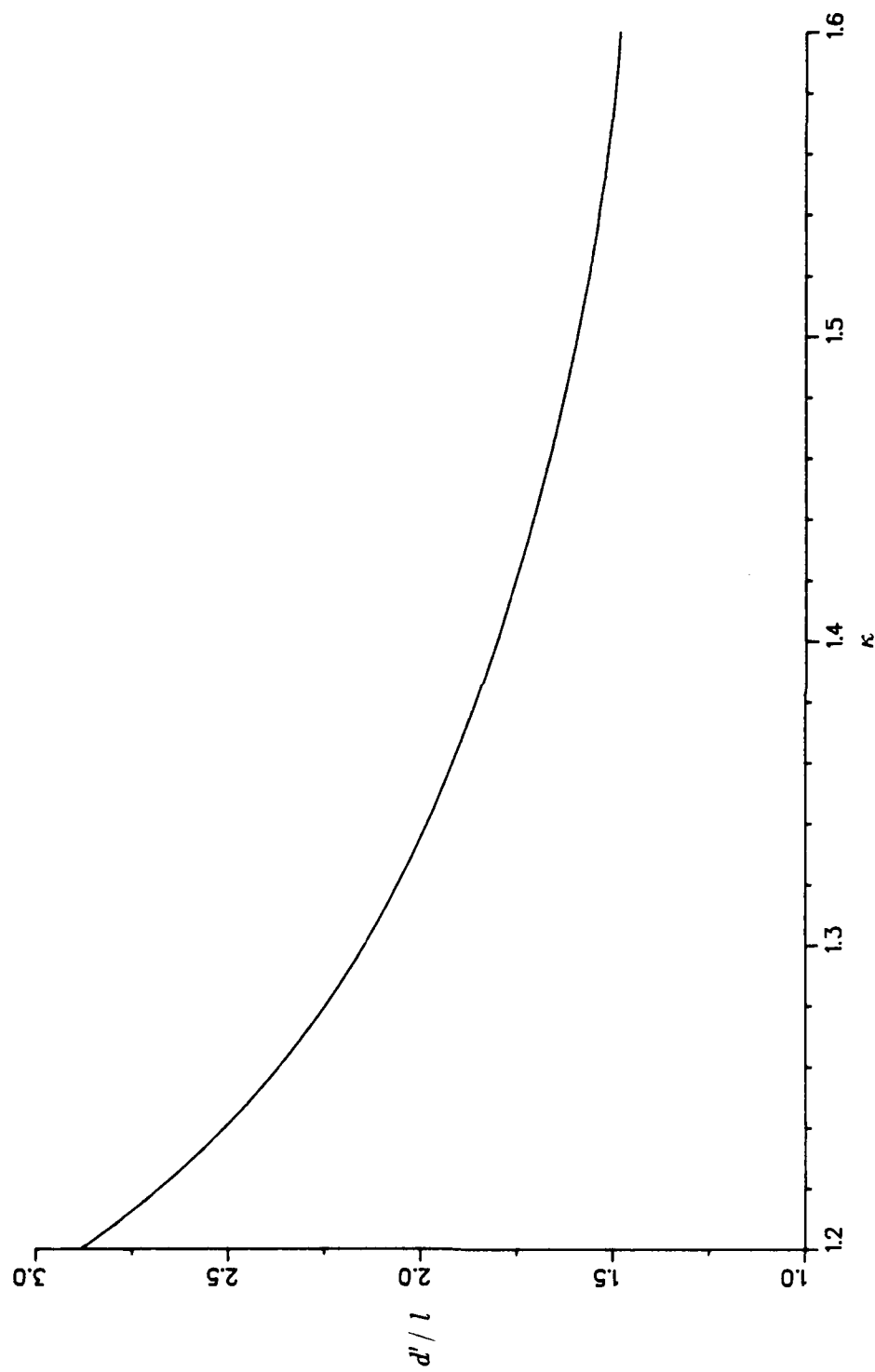
FIGURE 2.3: Relative Wake Width vs. κ (Roshko 1953).
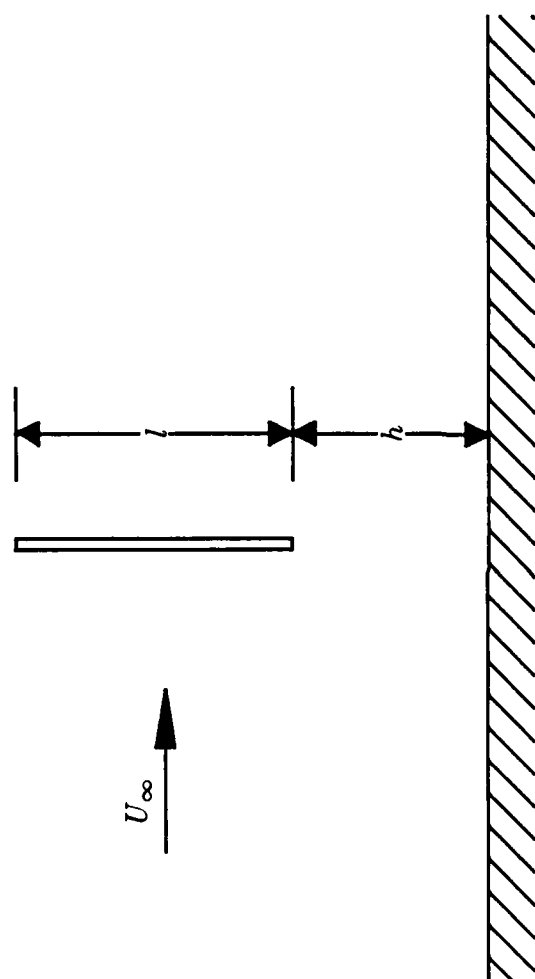
FIGURE 2.4: Geometry for a Flat Plate
Near a Ground Plane.
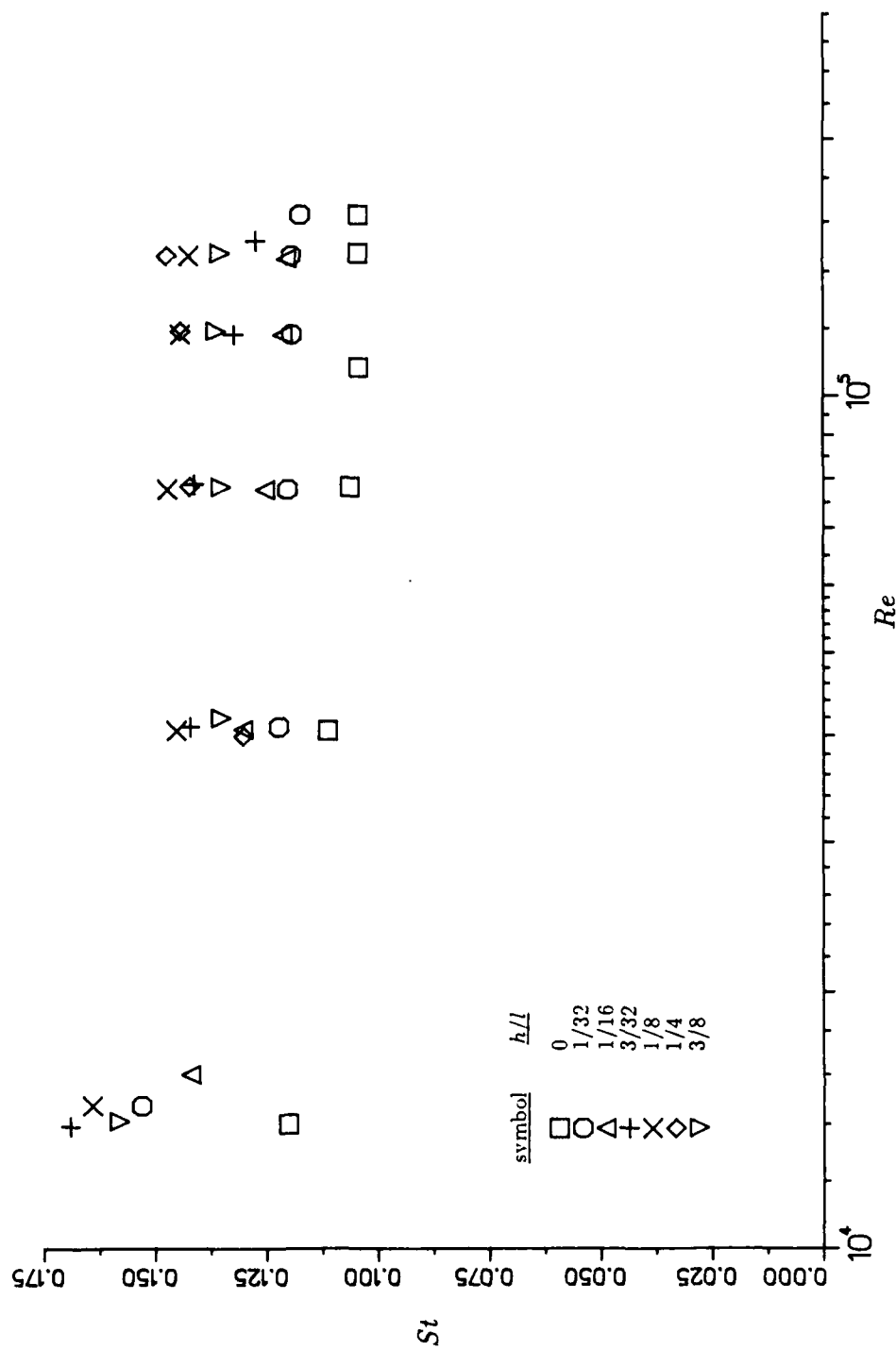
FIGURE 2.5: Strouhal Number vs. Reynolds Number for a Flat Plate Near a Ground Plane.

21
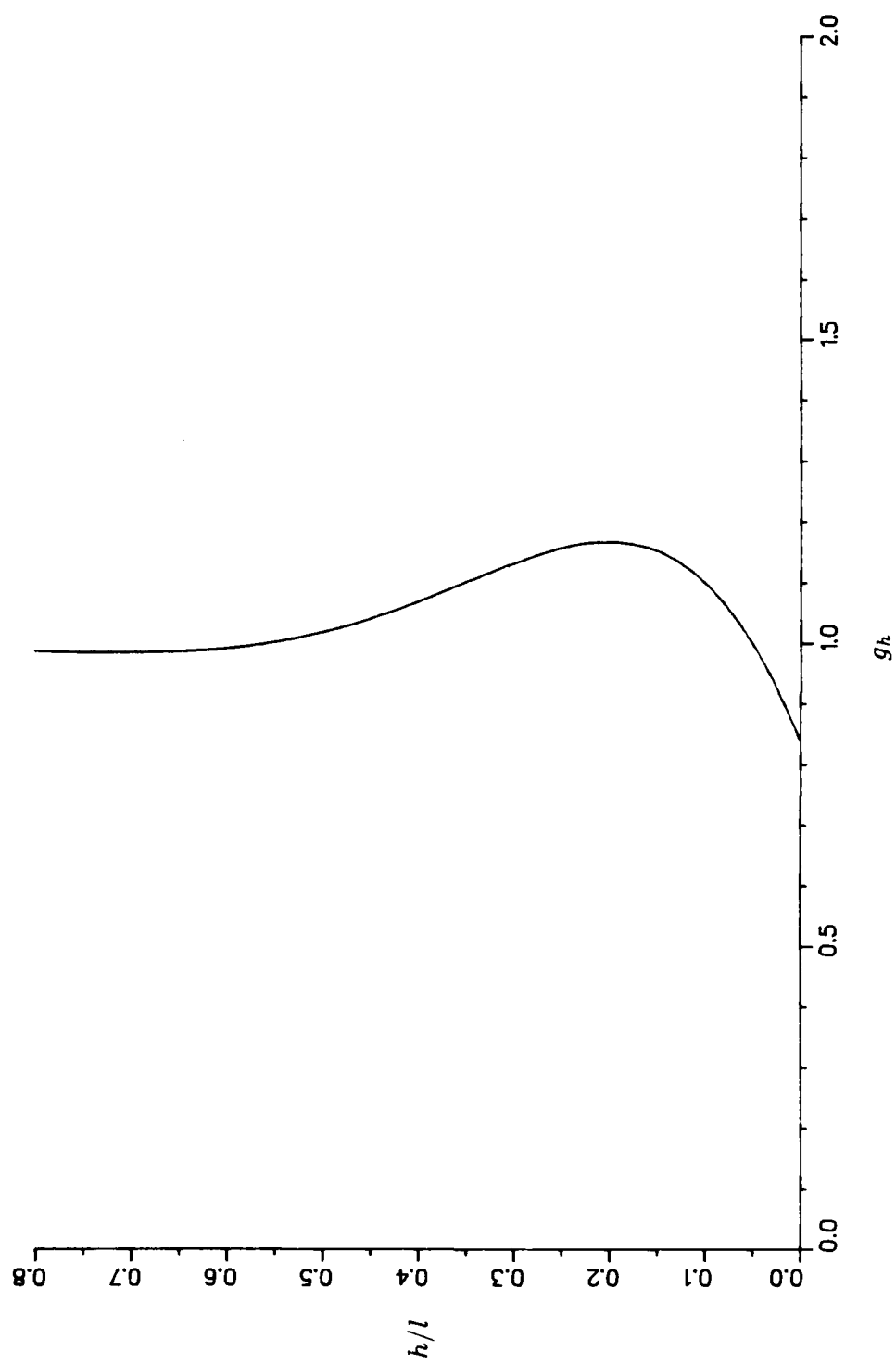
FIGURE 2.6: The Function $g_h(\lambda)$ (Matty 1979).
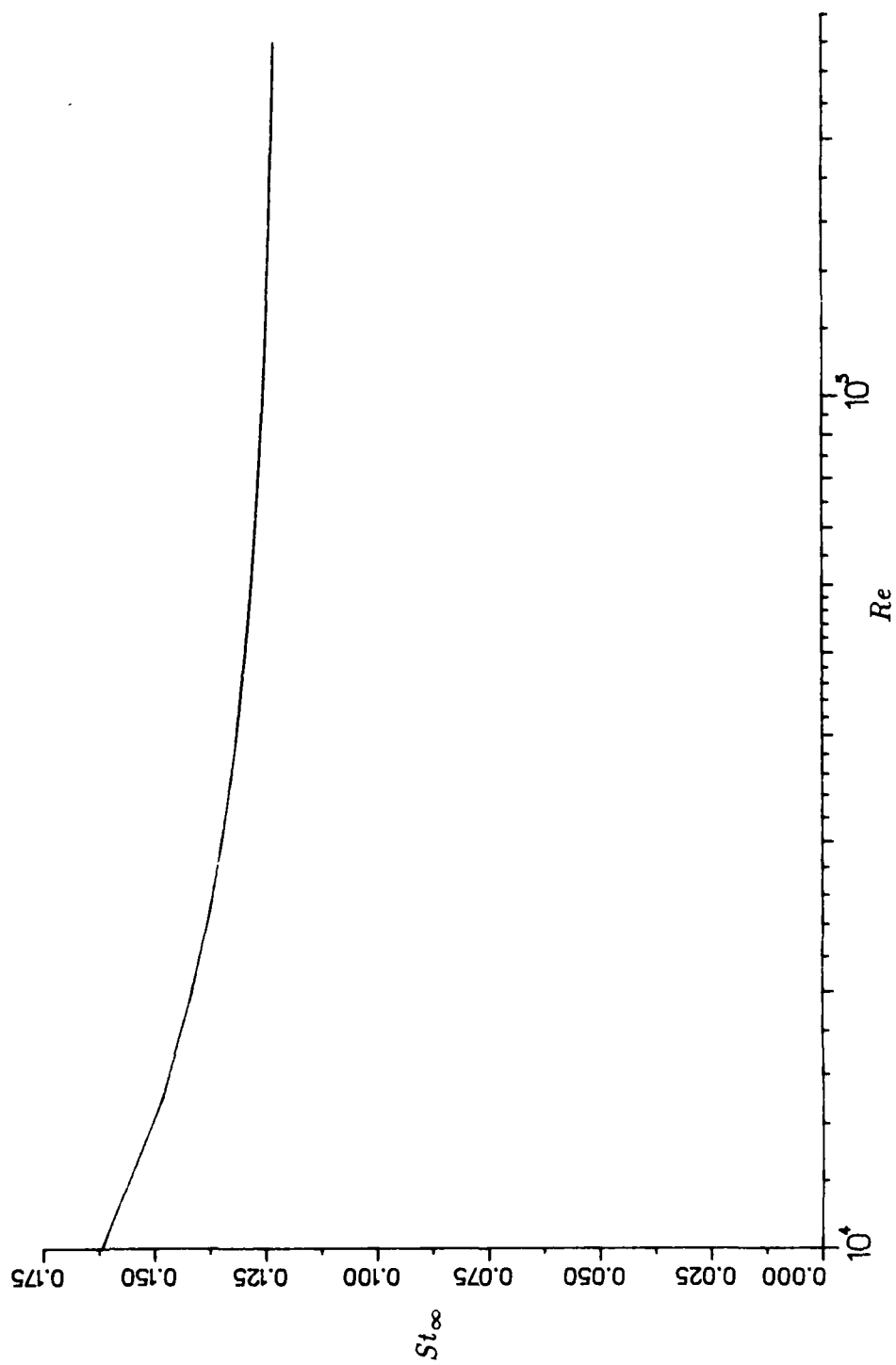
FIGURE 2.7: The Function $St_\infty(Re)$ (Matty 1979).
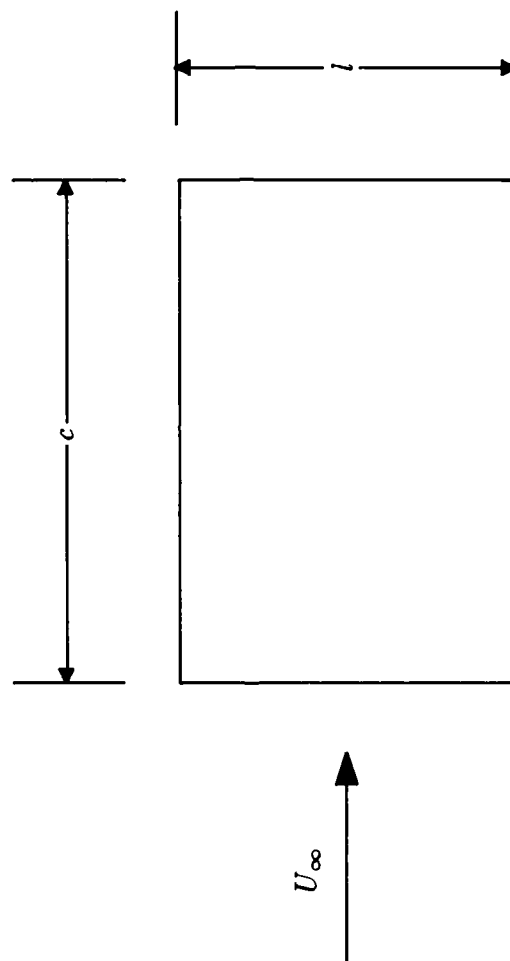
FIGURE 2.8: Geometry for a Rectangular Cylinder.
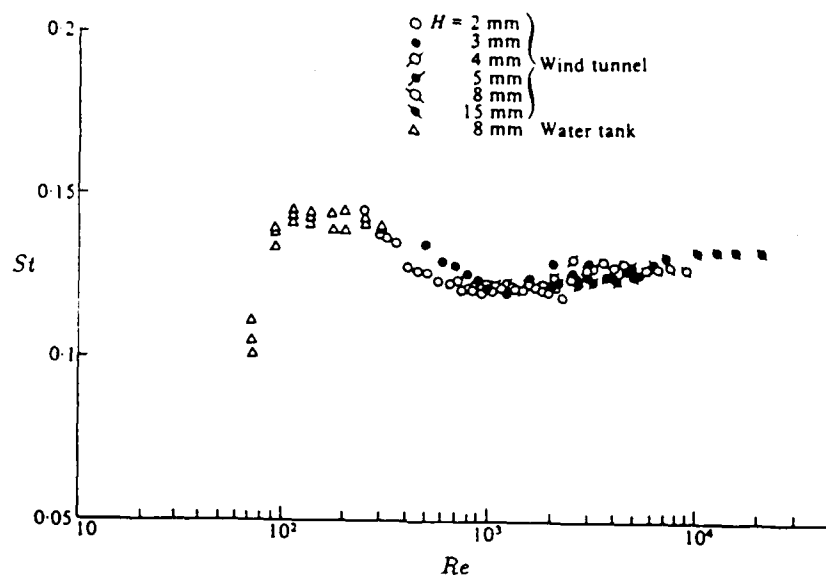
FIGURE 2.9: Strouhal Number vs. Reynolds Number
for a Cylinder with $\beta = 1$ (Okajima 1982).
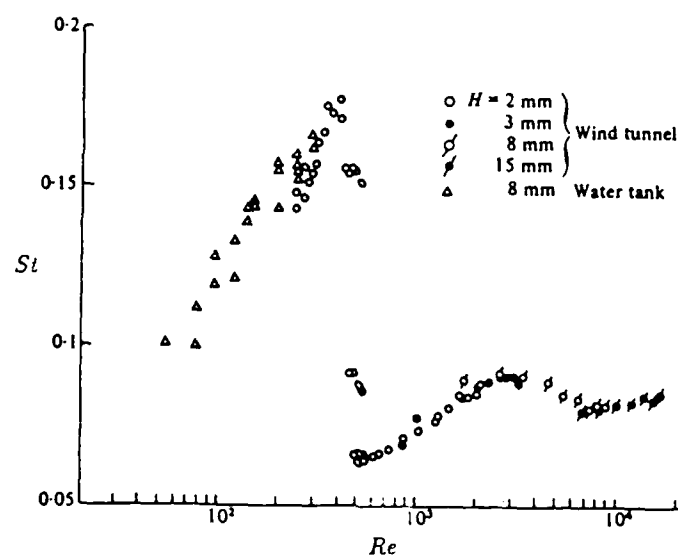
FIGURE 2.10: Strouhal Number vs. Reynolds Number
for a Cylinder with $\beta = 2$ (Okajima 1982).
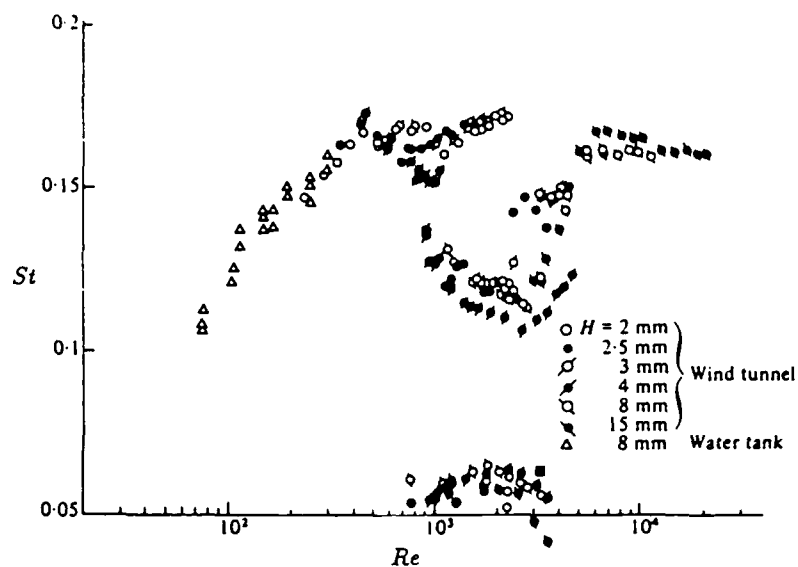
FIGURE 2.11: Strouhal Number vs. Reynolds Number
for a Cylinder with $\beta = 3$ (Okajima 1982).
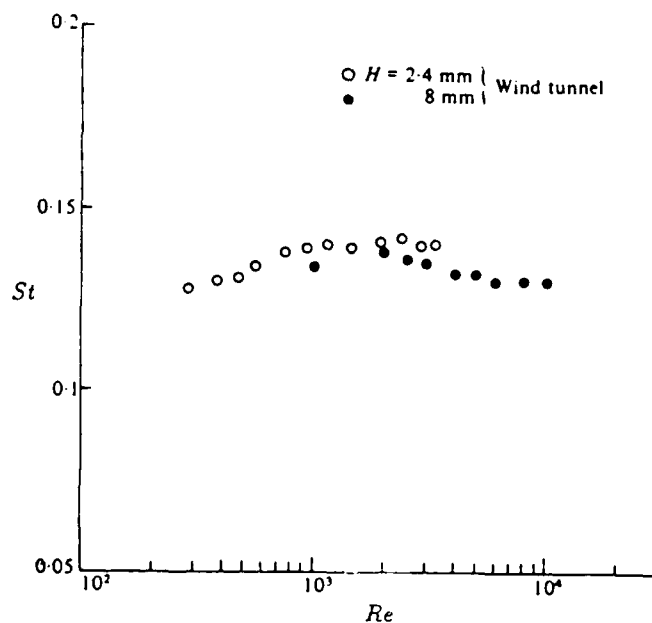
FIGURE 2.12: Strouhal Number vs. Reynolds Number
for a Cylinder with $\beta = 4$ (Okajima 1982).

CHAPTER III

DESCRIPTION OF COMPUTATIONAL ANALYSIS

The field of computational fluid dynamics is currently a field of considerable interest. The basic goal is to predict the distributions of velocity, pressure, temperature and other relevant variables throughout a given flow field. Advantages of computational methods over experimental methods include a greatly reduced cost and the ability to survey areas of a flow field that may be otherwise inaccessible. Furthermore, numerical methods allow the solution of problems which are impossible to solve using classical methods. Computational methods, of course, are not without disadvantages. In some cases, numerical solutions may diverge and yield no useful results. Also, for more complex flows, especially turbulent flows, empirical models are employed that may not suitably represent the physics of a situation. This may lead one to question the validity of computational results. For this reason, a combination of experimental and computational investigations will likely provide the most consistent and useable results. In the following discussion, the computational tools employed in this research are reviewed.

Discretization of Differential Equations

For a homogeneous fluid, a total description of the flow field consists of the distribution of six quantities throughout the flow domain. In Cartesian coordinates,

the six quantities which arise in these equations are the three velocity components, u, v, and w, pressure p, density ρ and temperature T. The required six equations for the solution of any flow problem are fundamental. Three equations are provided by conservation of momentum for each of the three Cartesian coordinate directions (x, y, z). These equations are also commonly known as the Navier–Stokes equations and are given for the x, y, and z directions respectively as

$$
\begin{aligned}
\rho \frac{Du}{Dt} = X - \frac{\partial p}{\partial x} &+ \frac{\partial}{\partial x}\left[\mu\left(2\frac{\partial u}{\partial x} - \frac{2}{3}div\mathbf{v}\right)\right] \\
&+ \frac{\partial}{\partial y}\left[\mu\left(\frac{\partial u}{\partial y} + \frac{\partial v}{\partial x}\right)\right] \\
&+ \frac{\partial}{\partial z}\left[\mu\left(\frac{\partial w}{\partial x} + \frac{\partial u}{\partial z}\right)\right]
\end{aligned}
\tag{3.1}
$$

$$
\begin{aligned}
\rho \frac{Dv}{Dt} = Y - \frac{\partial p}{\partial y} &+ \frac{\partial}{\partial y}\left[\mu\left(2\frac{\partial v}{\partial y} - \frac{2}{3}div\mathbf{v}\right)\right] \\
&+ \frac{\partial}{\partial z}\left[\mu\left(\frac{\partial v}{\partial z} + \frac{\partial w}{\partial y}\right)\right] \\
&+ \frac{\partial}{\partial x}\left[\mu\left(\frac{\partial u}{\partial y} + \frac{\partial v}{\partial x}\right)\right]
\end{aligned}
\tag{3.2}
$$

$$
\begin{aligned}
\rho \frac{Dw}{Dt} = Z - \frac{\partial p}{\partial z} &+ \frac{\partial}{\partial z}\left[\mu\left(2\frac{\partial w}{\partial z} - \frac{2}{3}div\mathbf{v}\right)\right] \\
&+ \frac{\partial}{\partial x}\left[\mu\left(\frac{\partial w}{\partial x} + \frac{\partial u}{\partial z}\right)\right] \\
&+ \frac{\partial}{\partial y}\left[\mu\left(\frac{\partial v}{\partial z} + \frac{\partial w}{\partial y}\right)\right]
\end{aligned}
\tag{3.3}
$$

where

t = time

X = x-direction body force

Y = y-direction body force

Z = z-direction body force

μ = dynamic viscosity

and **v** is the velocity vector

$$\mathbf{v} = u\mathbf{i} + v\mathbf{j} + w\mathbf{k} \quad .$$
(3.4)

A fourth equation is provided by conservation of mass, or the continuity equation, given as

$$\frac{\partial \rho}{\partial t} + \frac{\partial(\rho u)}{\partial x} + \frac{\partial(\rho v)}{\partial y} + \frac{\partial(\rho w)}{\partial z} = 0 \quad .$$
(3.5)

Conservation of energy provides the fifth equation which given in a basic form is

$$\delta Q = dE_T + \delta W$$
(3.6)

where

δQ = quantity of heat added

dE_T = increase in internal energy

δW = work done by the system.

The set of equations is closed by an equation of state, commonly the well known ideal gas law

$$p = \rho R T$$
(3.7)

where R is the specific gas constant. Of course, the use of the ideal gas equation assumes that the fluid is a gas. If this were not the case, an appropriate equation of state would have to be employed.

Theoretically, given six equations for six unknowns the solution to a given problem should be within reach. However, with the exception of very simple problems, this set of equations cannot be solved analytically. It then becomes the task of the computational fluid dynamics algorithm to provide an approximate solution that adequately describes the flow field.

To obtain a solution to a given flow field using a finite–difference scheme, the differential equations that describe the physics of the flow must first be discretized. To discretize the differential equations, one assumes that the flow field is composed of a discrete number of control volumes, and the flow variables stored at each control volume are prevalent for that region in space. The discretization equations are algebraic equations that relate the quantities at a grid location to the quantities at the neighboring grid locations. The equations that are derived to represent conservation of mass, momentum, and energy all follow the same basic form, which is

$$a_P \phi_P = a_E \phi_E + a_W \phi_W + a_N \phi_N + a_S \phi_S + b \tag{3.8}$$

where

a = finite–difference coefficient

b = source term

ϕ = general variable (u, v, T, etc.).

The subscripts identify which point in the field the a or ϕ refers to, as shown in Figure 3.1. The source term b is available to account for any terms which do not

conform readily to this format upon discretization of the differential equation. The most obvious example of a term that is contained in the source term b is the pressure gradient term in the momentum equations.

Among the most important aspects in the derivation of the finite–difference coefficients is the differencing scheme. The differencing scheme provides information on the variation of flow quantities between grid locations. The scheme employed in this research is known as the upwind scheme. In this scheme, the value of a quantity at a given point is assumed to be affected only by the cells which are upstream of the cell, with no influence of the downstream cells being felt. This scheme works well for processes governed primarily by convection, but it is not suitable for flows which are predominantly processes of diffusion. The solution of these discretization equations throughout the flow domain is the task of the finite–difference algorithm. For a detailed description of the finite–difference coefficients and other differencing schemes refer to Patankar (1980).

The FORDC–2 Finite–Difference Code

The basis for the code used in this research is the FORDC–2 (Flow Over Radiator and Condenser — 2 Dimensional) code developed by Carroll, Maxwell and Sun (1985). This code originally treated a flow as two–dimensional, incompressible, steady and elliptic. Modifications have been made to the code to allow the solution of unsteady problems and to speed the solution of the discretization equations.

The algorithm employed in the FORDC–2 code is the SIMPLE (Semi– Implicit Method for Pressure Linked Equations) algorithm described by Patankar (1980). A brief outline of this iterative method follows. The iterative process is started by assuming a pressure field. With the pressure field presumed to be known, one can

solve the momentum equations to obtain the velocities. Next, the pressure correction equation, a form of the continuity equation employed to insure conservation of mass, is solved. Following the solution of the pressure correction equation, the velocities and pressures are adjusted to insure satisfaction of continuity. The solution then proceeds to deal with any other quantities of interest (i.e. temperature). The updated pressure is then used to continue the iterative process. Typically, the iterative process is continued until the flow quantities remain virtually unchanged between iterations indicating a converged solution. However, in the transient case the solution should be valid at each step in time. Flow quantities may well be changing considerably between successive iterations, or time steps, in transient problems.

The FORDC–2 code was modified to speed the solution by altering the method by which the discretization equations are solved. Previously, all of the discretization equations except pressure correction were solved by the ADI (Alternating Direction Iteration) procedure. The program has been altered to allow the solution of all of the discretization equations by Stone's method. Stone's method is a field iterative solver that is claimed to be approximately three times as fast as other available methods. Stone's method requires the selection of a relaxation factor which was set to $\alpha = .93$. For details on the formulation of Stone's method, refer to either Stone (1968) or Carroll (1980).

Finite–Difference Grid

The accuracy of the solution of the finite–difference equations is governed by the approximation involved in determining the variation of a given quantity between neighboring grid locations. With respect to the variation of velocity, this problem can be remedied by employing a staggered grid. The premise of the staggered grid

is that there may be an advantage to storing some quantities at the main grid location while storing other variables elsewhere. A staggered grid is employed in the FORDC-2 code.

A representative segment of the finite-difference grid is shown in Figure 3.1. The grid is constructed in the Cartesian coordinate system in two dimensions (x, y). The capital letters (E, W, N, and S) mark the locations of the main grid points with respect to the point of interest, point P. Note that the symbols for the cells neighboring point P are derived from the points on a compass. It is at the main grid points that the properties of the fluid are stored, with the exception of the velocity components u and v. The dashed lines represent control volume faces, shown as lower case letters, which are the boundaries of the control volume at point P. The u velocity components are stored at the e and w faces and the v velocity components are stored at the n and s faces. It is the storage of the velocities at the control volume faces, removed from the main grid points, that creates the staggered grid. The staggered grid can simply be thought of as three different grids being employed on the same calculation domain: one grid is employed for the primary grid quantities, the second for u velocities, and the third for v velocities.

The advantage to be gained by this grid is that the mass flow across a control volume face can be calculated directly. If the velocities were stored at the main grid points with the other variables, the values of the velocities at the grid faces would arise from an interpolation and introduce an unnecessary approximation in the calculation of the mass flow through a control volume. Since satisfaction of continuity is fundamental to the solution of any flow problem, it is critical to calculate accurate mass flow rates. The employment of the staggered grid aids in the achievement

of that end. This type of grid also allows the direct calculation of the pressure gradient for a given control volume.

The finite–difference grid is constructed for the entire calculation domain by the specification of the control volume face locations. Once the face locations have been identified, the main grid points are placed such that they are centered between the control volume faces in each direction. The spacing between the faces can be either uniform or nonuniform. The advantage of the nonuniform grid is that the grid can be made more dense in areas of interest without making the entire grid dense. This allows one to get more detailed information about the flow field in the areas of interest without increasing computer run time.

Boundary Conditions

The uniqueness of a given problem is determined by the specification of boundary conditions. In the case of pressure and temperature, the boundaries were typically set to take on ambient conditions. However, the boundary conditions imposed on velocities are the primary interest in this case.

The inlet and exit boundary conditions are critical to calculating accurate flow fields. In these studies, the inlet velocity plane is always situated at the location of minimum x, and the outlet velocity plane is always situated at the location of maximum x. The inlet velocity distribution is simply specified to match the desired velocity profile at the inlet of the calculation domain. For these studies, the inlet is always a uniform velocity, U_∞. The exit boundary velocity must be such that the continuity equation is satisfied. This result can be achieved in two manners by the FORDC–2 code. First, the velocity at the exit plane can be specified directly to satisfy conservation of mass. The second scheme available adds some sophistication

to the calculation of the exit velocity profile, but also carries a restriction on the direction of the exiting flow.

The second scheme for setting the exit boundary condition is intended to allow the finite–difference algorithm to calculate the proper exit velocity profile. The scheme involves calculating the mass flow across the plane just ahead of the exit plane, scaling all of the velocities on this plane to match the entering mass flow, and then placing these scaled velocities at the exit plane. In this manner, the velocity profile at the exit is similar to the profile just upstream of the exit and overall continuity is satisfied. However, one must be cautious to place the exit boundary far downstream, for any backflow at the exit will prevent this scheme from working properly.

The other exterior boundaries to the flow are handled by either external walls or symmetry planes. If the boundary is considered to be a wall, the velocity components are set to zero at the wall. However, if the boundary is placed at a fluid–fluid interface, then the proper boundary condition is a symmetry plane or slip wall. The symmetry boundary condition is imposed by setting the finite–difference coefficient that links the boundary point to an interior cell equal to zero. This insures that the velocity stored at the symmetry boundary has no effect on the flow field. This is typically used in a situation where the boundary could also have been considered to be at freestream conditions. For this reason, the location of a symmetry boundary is typically far from the body about which the fluid is flowing. Of course, if there is an actual symmetry in the flow field, then the symmetry boundary can be used at a symmetry plane to shrink the calculation domain. This allows one to achieve greater resolution in the flow field while still maintaining the same number

of control volumes. A simple example where an actual symmetry plane could be used is the flow between two flat plates, or Poiseuille flow.

Another important consideration, though not technically a boundary condition, is the internal wall. For these studies, internal walls are always considered to be impermeable. The walls are placed at control volume faces since the specification of the wall requires that the velocity component perpendicular to the wall be set to zero. The finite–difference coefficient that links the velocities parallel to the wall on either side of the wall is set to zero. This prevents these velocities from wrongly influencing each other across a wall. Finally, the viscous effects that appear near walls are accounted for by employing a wall function (Nallasamy 1985). The numerical implementation of the wall function is outlined by Carroll et al.

Turbulence Model

The accurate modelling of turbulent flows is a particularly challenging problem. Theoretically, solution of the full Navier–Stokes equations should provide an accurate result with the full effects of turbulence present. The problem lies in the fact that the scale of the turbulent fluctuations are on the order of 10^{-3} that of the primary flow (Rodi 1984). For a two–dimensional flow, this would require an increase in the number of grid points by an order of 10^6 to handle the details of the turbulence. Even on the fastest of today's supercomputers, solution of such a large set of equations would require prohibitive amounts of memory, time, and money.

To account for the effects of turbulence without attempting the solution of the full Navier–Stokes equations one employs empirical turbulence models. The Navier–Stokes equations are converted into time averaged equations by assuming that the flow quantities are composed of a mean value and a fluctuating value

$$\phi = \bar{\phi} + \phi' \tag{3.9}$$

where

$\bar{\phi}$ = mean value of ϕ

ϕ' = fluctuating component of ϕ.

Typically it is the mean values of the flow which are of interest. This formulation spawns additional terms for which extra relations must be derived. For the momentum equation, these additional terms are known as the Reynolds stresses. It is the task of the turbulence model to express these terms as functions of the mean flow quantities.

The turbulence model employed in the FORDC-2 program is perhaps the most popular turbulence model used in the computational fluid dynamics codes, the k-ϵ model. The basis of this model is that the turbulent flow can be characterized by two quantities, the kinetic energy of turbulence, k, and the dissipation rate of turbulence energy, ϵ. The solution of the differential equations for k and ϵ allows the calculation of a turbulent, or eddy viscosity, μ_t. The eddy viscosity is added to the laminar viscosity to yield an effective viscosity,

$$\mu_{eff} = \mu + \mu_t \quad . \tag{3.10}$$

It is this variation in the local viscosity which accounts for the presence of turbulence in a flow. This model was derived empirically, and expectedly does not work well for all flow situations. For a more detailed description of the k-ϵ turbulence model refer to Rodi or Nallasamy.
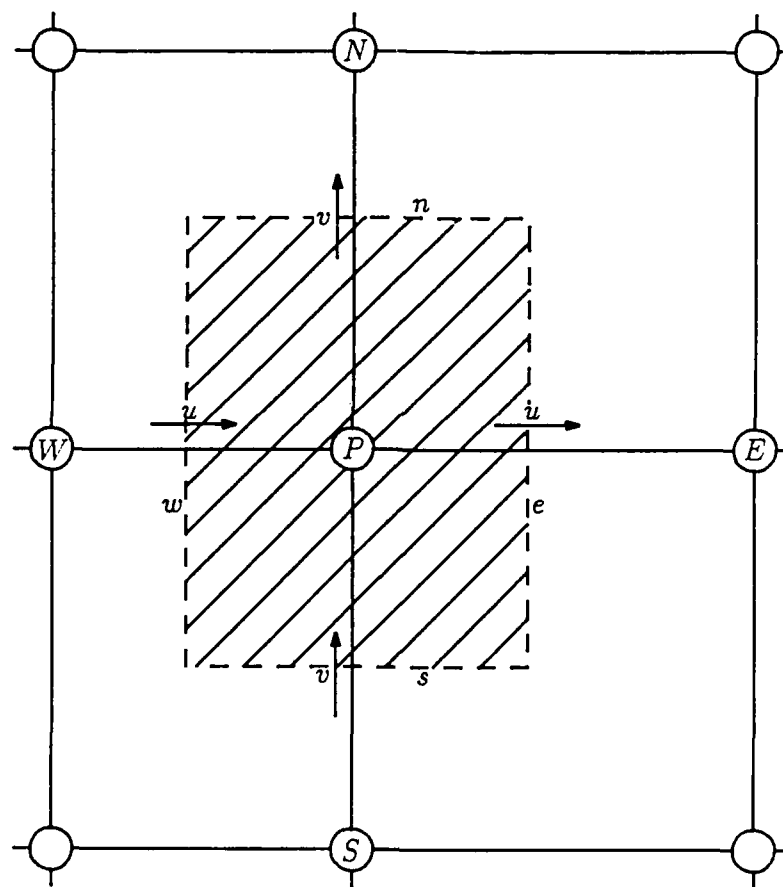
FIGURE 3.1: Representative Segment of a
Finite–Difference Grid.

CHAPTER IV

DETERMINATION OF AERODYNAMIC FORCE COEFFICIENTS AND SHEDDING FREQUENCY

The following discussion outlines the methods for calculating various parameters associated with a given flow. The methodology for calculating the drag coefficient C_D, the lift coefficient C_L, and the Strouhal number St are discussed.

Drag Coefficient

In the most general treatment, the aerodynamic forces experienced by a body are the result of the distribution of shear stress and pressure on the surface of the body. The drag force is the force experienced by the body in a direction parallel to the freestream velocity. For the case of a flat plate, if one considers the plate to be infinitesimally thin the effects of shear and pressure on the width of the plate can be neglected. Therefore, the drag on a plate which is normal to the freestream direction is simply a function of the pressure distribution on the plate.

Referring to Figure 4.1 one can immediately write the drag force as

$$D = \int_0^l p_f(y)dA - \int_0^l p_b(y)dA \quad . \tag{4.1}$$

This calculation of drag is dependent on a knowledge of the continuous distribution of the pressure force over the surface of the plate. However, in the computational scheme the surface of the plate has been broken into a discrete number of elements, N. An example of the discretized pressure distribution is given in Figure 4.2. Defining the depth of the plate as a unit 1, the differential area then becomes

$$dA = dy \cdot 1 = dy \quad . \tag{4.2}$$

One can then write the drag in terms of the discretized pressures as

$$D = \sum_{i=1}^{N} (p_f - p_b)_i \Delta y_i \quad . \tag{4.3}$$

This expression can be simplified by denoting the pressure differential as

$$\Delta p_i = (p_f - p_b)_i \tag{4.4}$$

which gives an expression for the drag

$$D = \sum_{i=1}^{N} \Delta p_i \Delta y_i \quad . \tag{4.5}$$

This expression can be further simplified by noting that the plate is discretized into elements of equal length Δy_i. This yields the simplified drag expression

$$D = \Delta y \sum_{i=1}^{N} \Delta p_i \quad . \tag{4.6}$$

The task is then to cast the drag force in terms of a drag coefficient. Recall that the definition of the drag coefficient is

$$C_D = \frac{D}{q_\infty A} \quad . \tag{4.7}$$

Substituting the expressions for the drag and the area yields

$$C_D = \frac{\Delta y \sum_{i=1}^{N} \Delta p_i}{q_\infty l} \quad . \tag{4.8}$$

Note that since all of the Δy_i are equal that an arithmetic average for Δp_i can be written as

$$\Delta \bar{p}_i = \frac{\sum_{i=1}^{N} \Delta p_i}{N} \tag{4.9}$$

or similarly

$$\sum_{i=1}^{N} \Delta p_i = N \Delta \bar{p}_i \quad . \tag{4.10}$$

Substituting equation 4.10 into equation 4.8 yields the result that

$$C_D = \frac{N \Delta y \Delta \bar{p}_i}{q_\infty l} \quad . \tag{4.11}$$

By noting that $N \Delta y$ is simply the plate length l, a final expression for the drag coefficient can be written as

$$C_D = \frac{\Delta \bar{p}_i}{q_\infty} \quad . \tag{4.12}$$

Lift Coefficient

The lift force is defined as that force which acts on body in a direction normal to the freestream velocity. For the case of an infinitesimally thin flat plate which is

oriented normal to the freestream direction, the lift is due only to the shear forces which act on the surface of the flat plate.

Figure 4.3 shows the distribution of the shear stress $\tau(y)$ on the surface of a flat plate. The shear stress for a Newtonian fluid in the coordinate system defined in Figure 4.3 is

$$\tau_y = \mu \frac{dv}{dx} \quad . \tag{4.13}$$

The velocity gradient dv/dx can be computed by simply dividing the v velocity that neighbors the surface by the distance between the velocity location and the surface. The gradient may be calculated in this manner because the velocity at the surface must be zero.

Turning now to the calculation of the lift force, one can immediately write that

$$L = \int_0^l \tau_{y_f}(y)dA + \int_0^l \tau_{y_b}(y)dA \quad . \tag{4.14}$$

Proceeding in the same manner as that used in the calculation of C_D, the lift for equal Δy_i can be written as

$$L = \Delta y \sum_{i=1}^N (\tau_{y_f} + \tau_{y_b})_i \quad . \tag{4.15}$$

Recalling the definition of the lift coefficient as

$$C_L = \frac{L}{q_\infty A} \tag{4.16}$$

the lift and area expressions can be substituted to yield

$$C_L = \frac{\Delta y \sum_{i=1}^{N} (\tau_{y_f} + \tau_{y_b})_i}{q_\infty l} \quad . \tag{4.17}$$

Again, due to the uniformity of the Δy_i terms the arithmetic average of the shear stresses can be written as

$$(\bar{\tau}_{y_f} + \bar{\tau}_{y_b}) = \frac{\sum_{i=1}^{N} (\tau_{y_f} + \tau_{y_b})_i}{N} \quad . \tag{4.18}$$

By substituting equation 4.18 into equation 4.17 and recognizing that $N\Delta y$ is l, the lift coefficient can be written as

$$C_L = \frac{(\bar{\tau}_{y_f} + \bar{\tau}_{y_b})}{q_\infty} \quad . \tag{4.19}$$

Finally, one may put the expression for C_L in terms of the simplest quantities and eliminate the $\bar{\tau}_y$ terms. Referring to Figure 4.4, the average shear stresses can be written as

$$\bar{\tau}_{y_f} = \mu \frac{\bar{v}_f}{\delta x_f} \tag{4.20}$$

$$\bar{\tau}_{y_b} = \mu \frac{\bar{v}_b}{\delta x_b} \quad . \tag{4.21}$$

Substituting equations 4.20 and 4.21 into equation 4.19, a final expression for C_L in terms of the variables calculated in the program is given as

$$C_L = \mu \frac{(\bar{v}_f/\delta x_f) + (\bar{v}_b/\delta x_b)}{q_\infty} \quad . \tag{4.22}$$

Aerodynamic Forces on a Rectangular Cylinder

With the lift and drag on a flat plate resolved, the task now is to extend those forces to a rectangular cylinder. The pressure and shear forces which act on the cylinder are shown in Figure 4.5. Note that for the rectangular cylinder lift and drag both have force components due to pressure and shear stress. Recalling the definitions of C_D and C_L once more, and using the forms of the lift and drag forces given in the previous section, the lift and drag coefficients on the rectangular cylinder are easily derived.

Drag on the cylinder oriented normal to the freestream velocity is due to the pressure on the front and back surfaces and the shear stresses on the upper and lower surfaces. Once again the spacing of the Δx_i and Δy_i terms is uniform, with N elements composing a vertical surface and M elements composing a horizontal surface. An expression for the drag in terms of average pressures and stresses can be written immediately as

$$D = N(\bar{p}_f - \bar{p}_b)\Delta y + M(\bar{\tau}_{x_u} + \bar{\tau}_{x_l})\Delta x \quad . \tag{4.23}$$

Recalling that $N\Delta y$ is l and $M\Delta x$ is c, the drag coefficient becomes

$$C_D = \frac{(\bar{p}_f - \bar{p}_b)}{q_\infty} + \frac{(\bar{\tau}_{x_u} + \bar{\tau}_{x_l})c}{q_\infty l} \quad . \tag{4.24}$$

Lift on the cylinder is due to the pressure on the upper and lower surfaces and the shear stresses on the front and back surfaces. The lift can then be written as

$$L = M(\bar{p}_l - \bar{p}_u)\Delta x + N(\bar{\tau}_{y_f} + \bar{\tau}_{y_b})\Delta y \quad . \tag{4.25}$$

The lift coefficient is then

$$C_L = \frac{(\bar{p}_l - \bar{p}_u)c}{q_\infty l} + \frac{(\bar{\tau}_{y_f} + \bar{\tau}_{y_b})}{q_\infty} \quad . \tag{4.26}$$

The expressions for calculating C_D and C_L for both a flat plate and a rectangular cylinder perpendicular to the freestream flow have been determined. These equations are the relations programmed into the FORDC–2 code for the determination of the aerodynamic force coefficients.

Shedding Frequency

The method for determining the shedding frequency is derived from the work by Younis (1988). He proposed to determine the shedding frequency by examining the periodic fluctuations in three fundamental quantities. He determined the frequency n by examining

1. the axial velocity at two locations behind the body as shown in Figure 4.6, the velocities being denoted by u_1 and u_2,

2. the drag coefficient C_D, and

3. the lift coefficient C_L.

For the slightly more complex case of a rectangular cylinder, the axial velocity is measured at four locations as shown in Figure 4.7 because of the possibility of vortices being shed from either the front or rear of the cylinder. Note that the flow field must be allowed to reach a cyclic state before the frequency can be determined by this method.

The shedding frequency can be extracted directly from plots of either u_1, u_2, C_D, or C_L versus time. This method, with one exception, assumes that vortices are shed at the same frequency at which the aforementioned quantities fluctuate.

Knowledge of the shedding frequency immediately leads to the Strouhal number by the relation

$$St = \frac{nd}{U_\infty} \quad .$$
(4.27)

Younis notes that the drag oscillates at twice the frequency of the lift, which oscillates at the shedding frequency. Plots of the fluctuations in C_D and C_L provided by Younis are given as Figure 4.8 and clearly demonstrate the higher frequency oscillation in the drag. Similar plots obtained in this research for a flat plate at $Re = 7826$ are given in Figures 4.9–4.12, and the higher frequency oscillation of the drag is again evident.
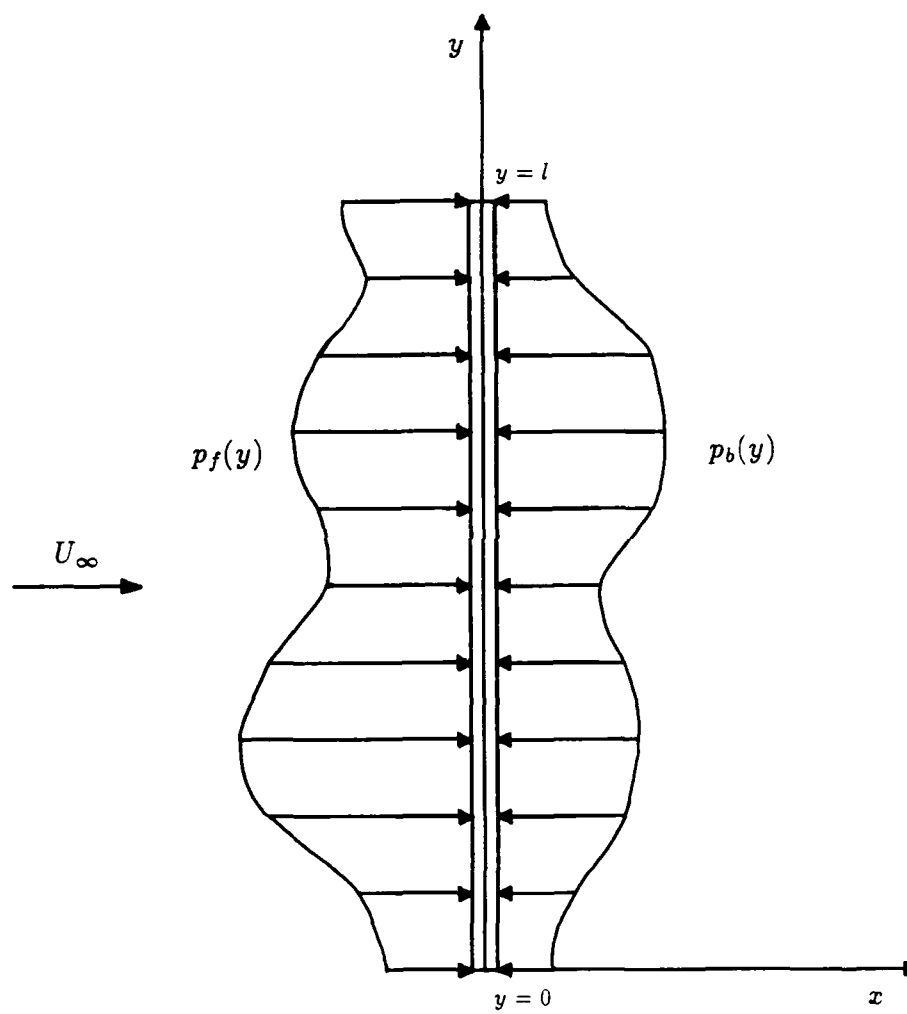
FIGURE 4.1: Pressure Distribution on a
Thin Flat Plate.
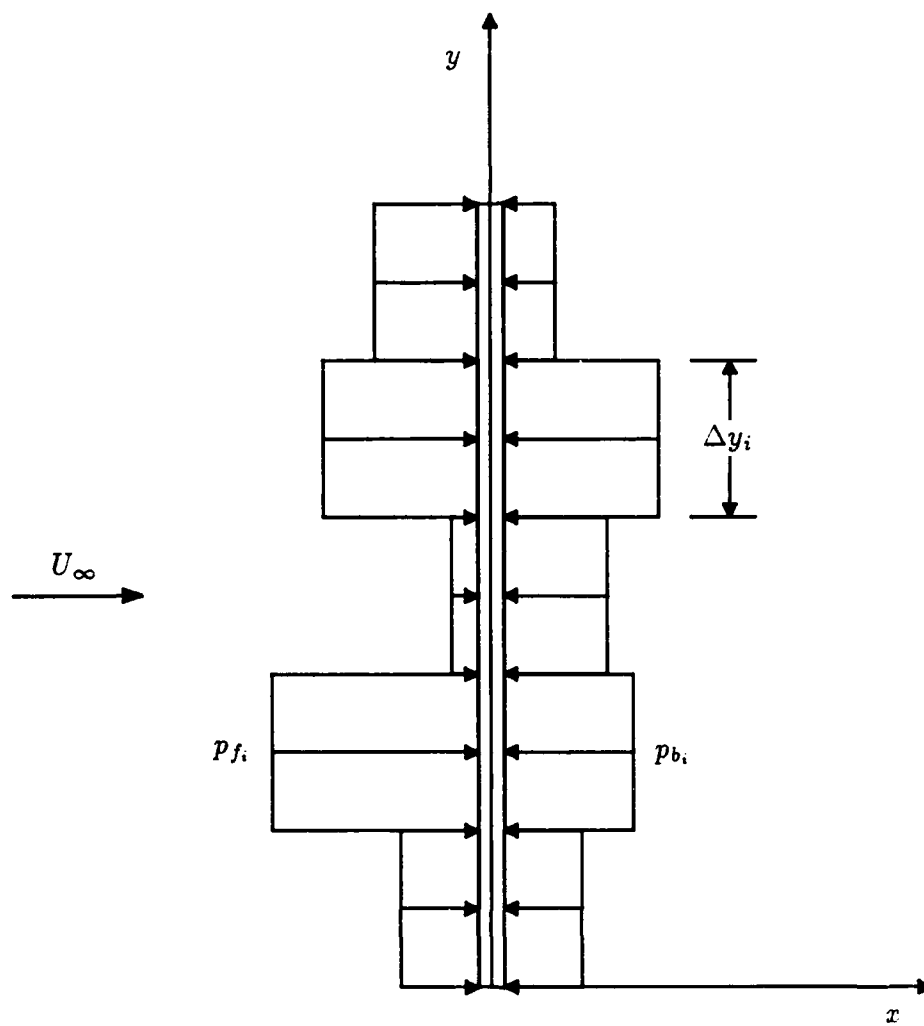
FIGURE 4.2: Discretized Pressure Distribution
on a Thin Flat Plate.
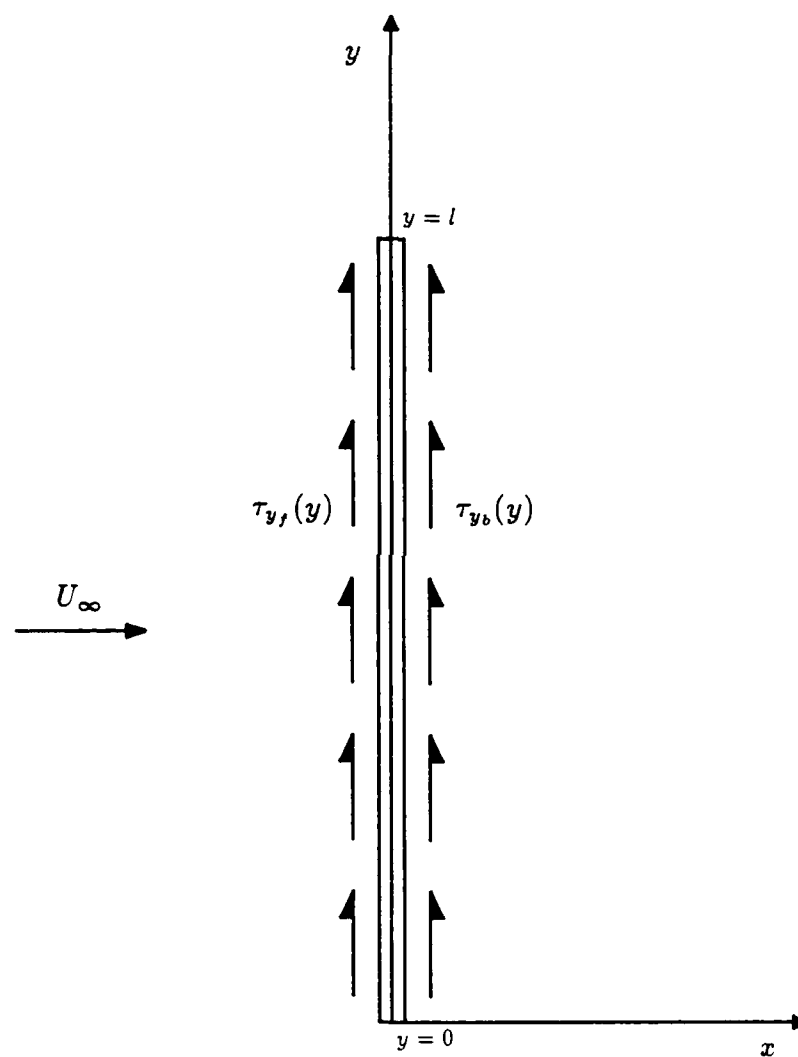
FIGURE 4.3: Distribution of Shear Stress
on a Thin Flat Plate.
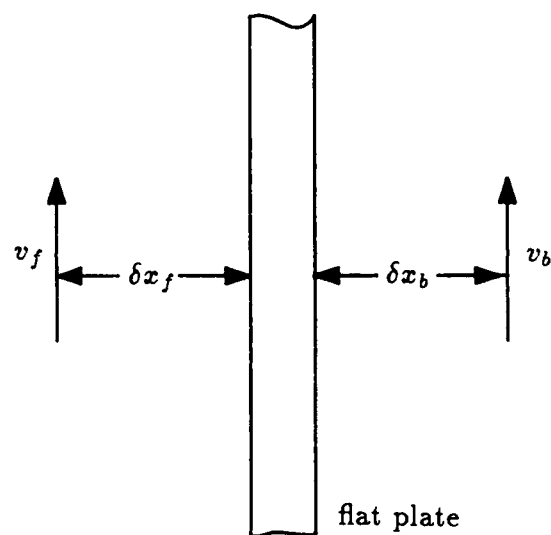
FIGURE 4.4: Geometry for the Calculation of
Wall Shear Stress.
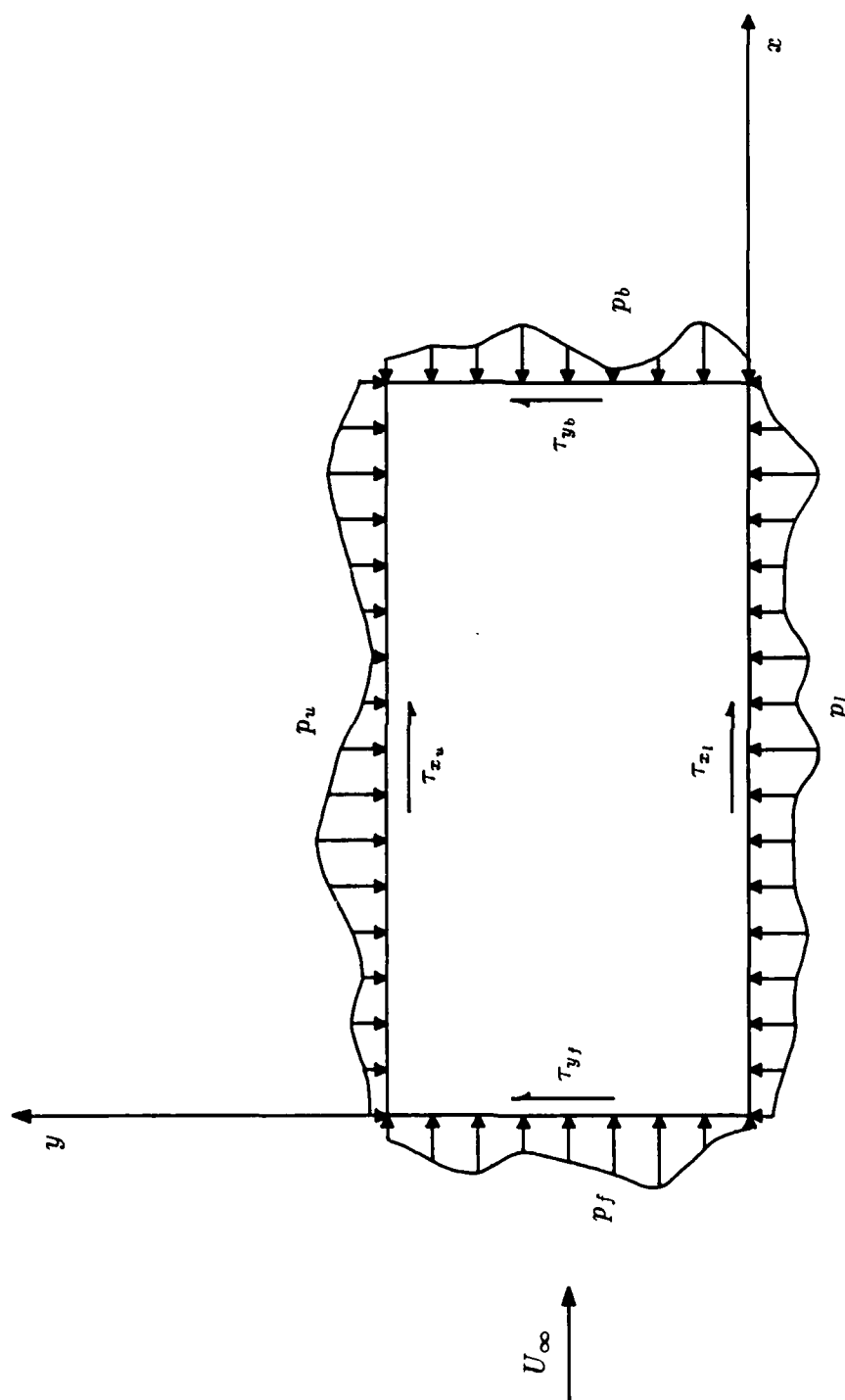
FIGURE 4.5: Dis ation of Pressure and Shear Stress on a Rectangular Cylinder.

U_∞
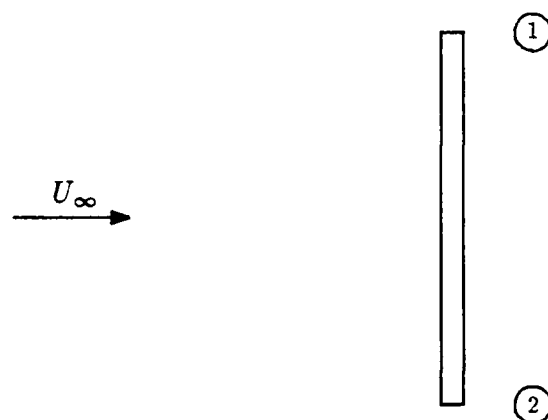
FIGURE 4.6: Locations for Transient Velocity
Measurements for a Flat Plate.

U_∞
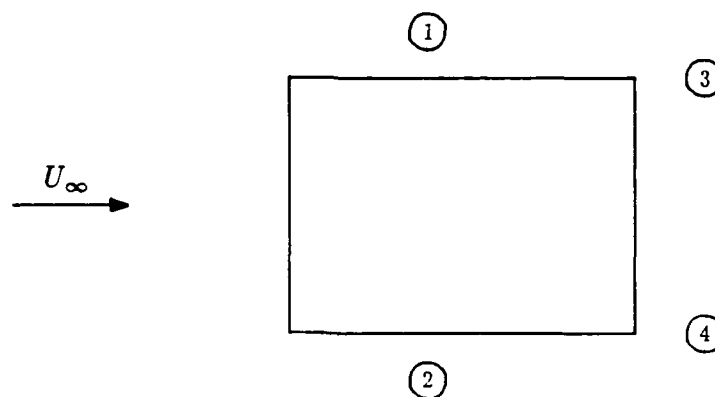
FIGURE 4.7: Locations for Transient Velocity Measurements
for a Rectangular Cylinder.
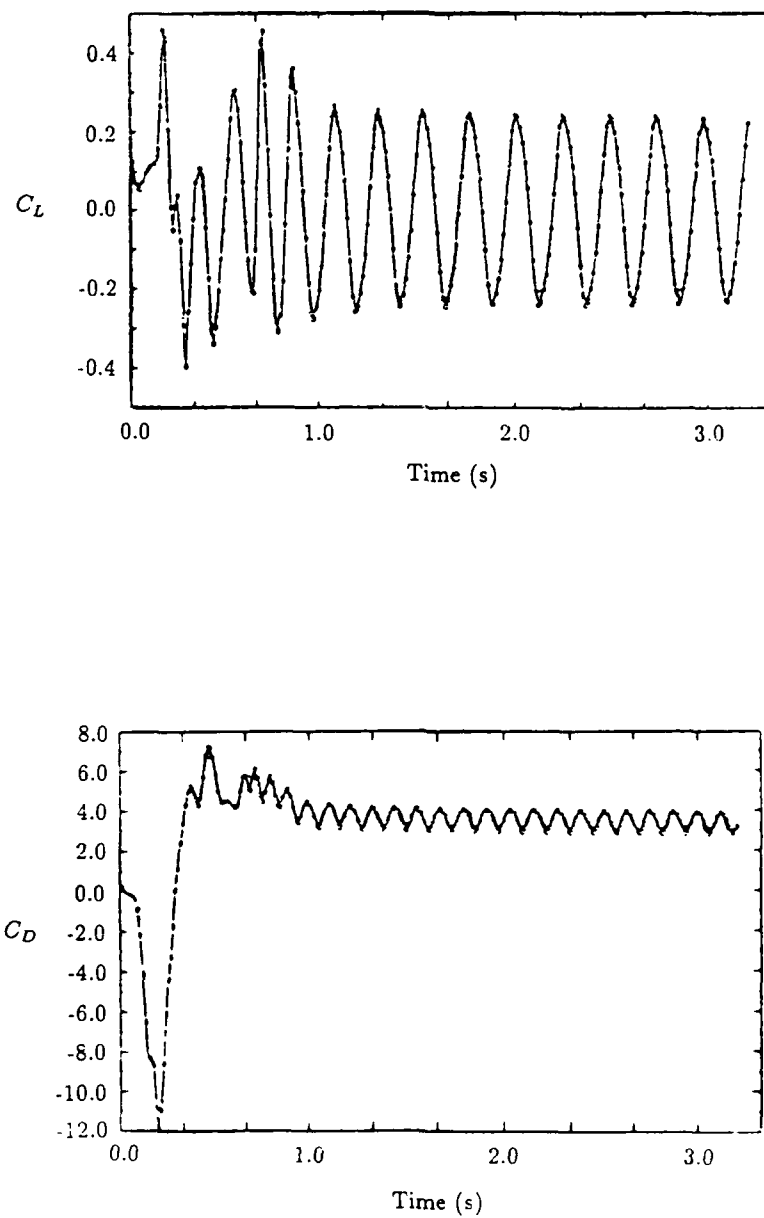
FIGURE 4.8: Variation in Aerodynamic Force Coefficients
Over Time (Younis 1988).
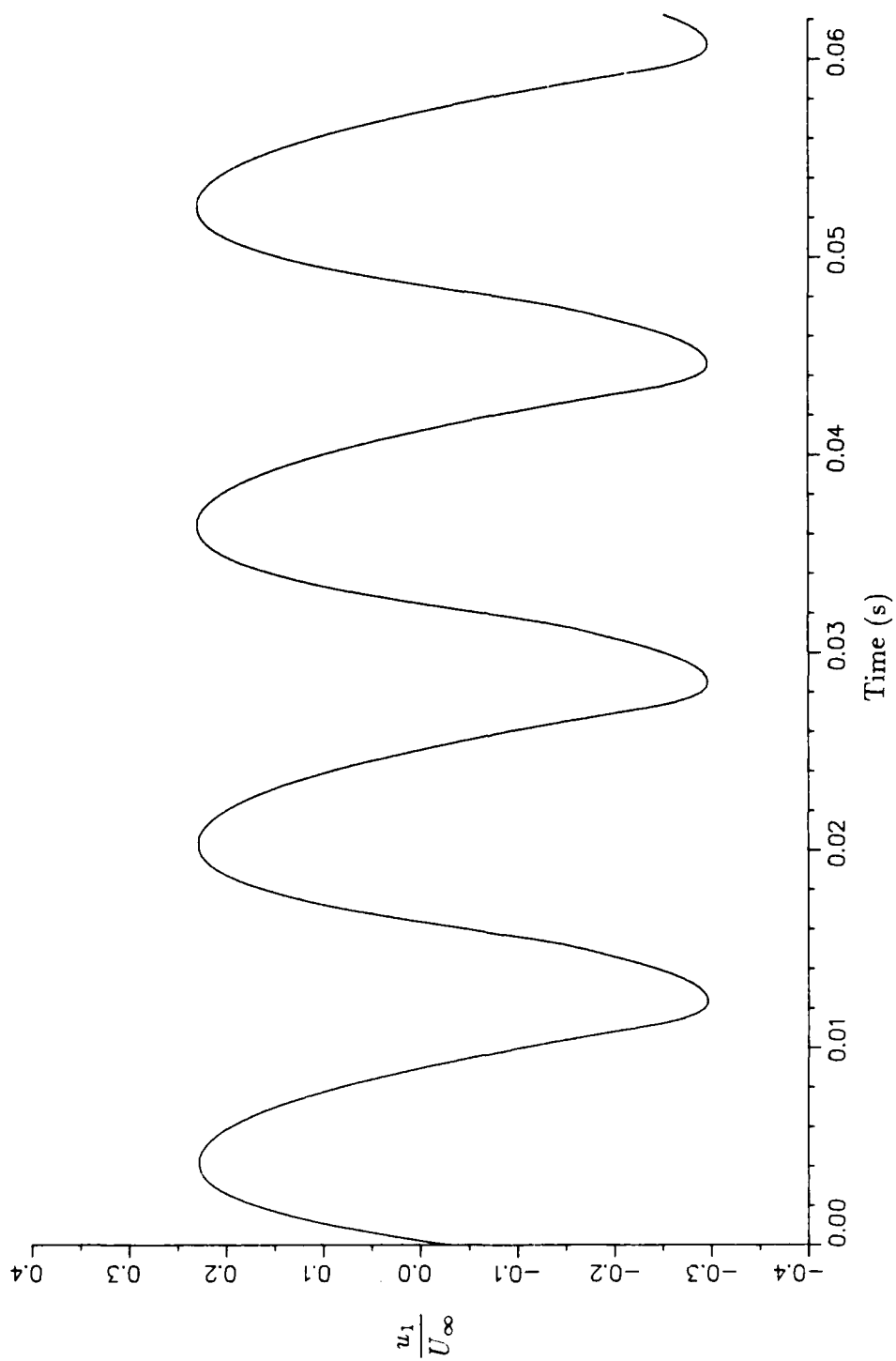
FIGURE 4.9: Variation in $u_1/U\infty$ Over Time
for $Re = 7826$.
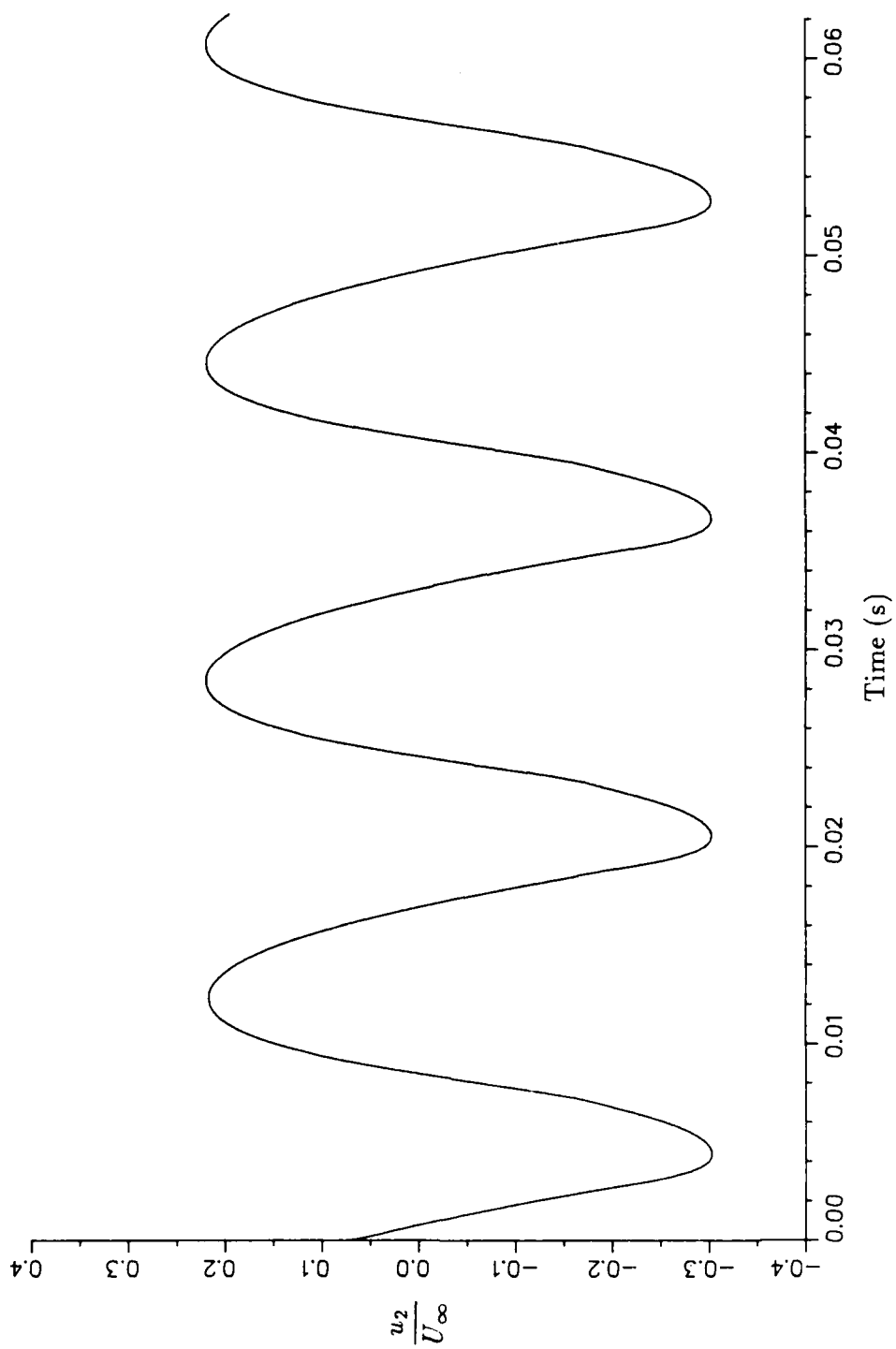
FIGURE 4.10: Variation in u_2/U_∞ Over Time for $Re = 7826$.
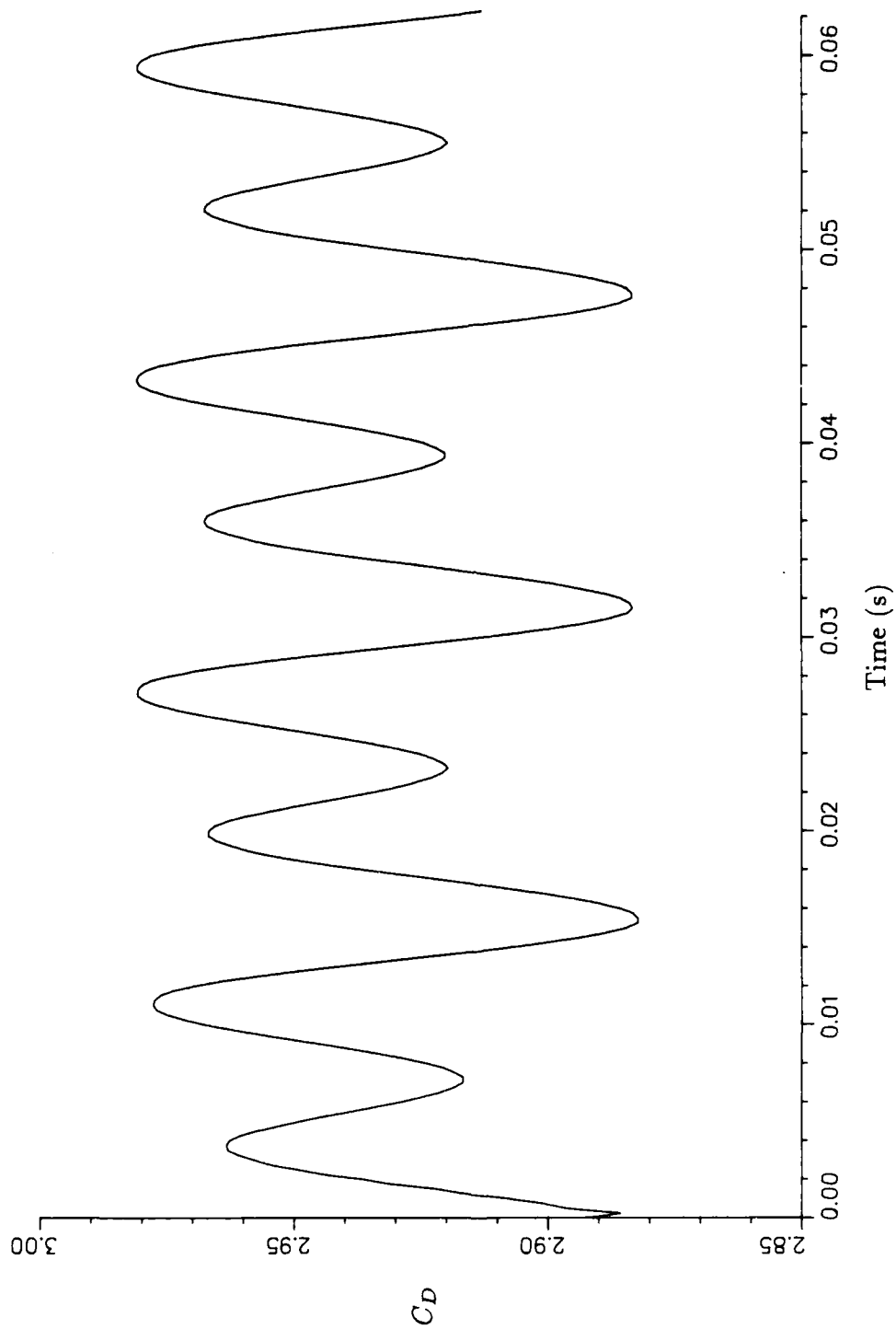
FIGURE 4.11: Variation in Drag Coefficient Over Time for $Re = 7826$.
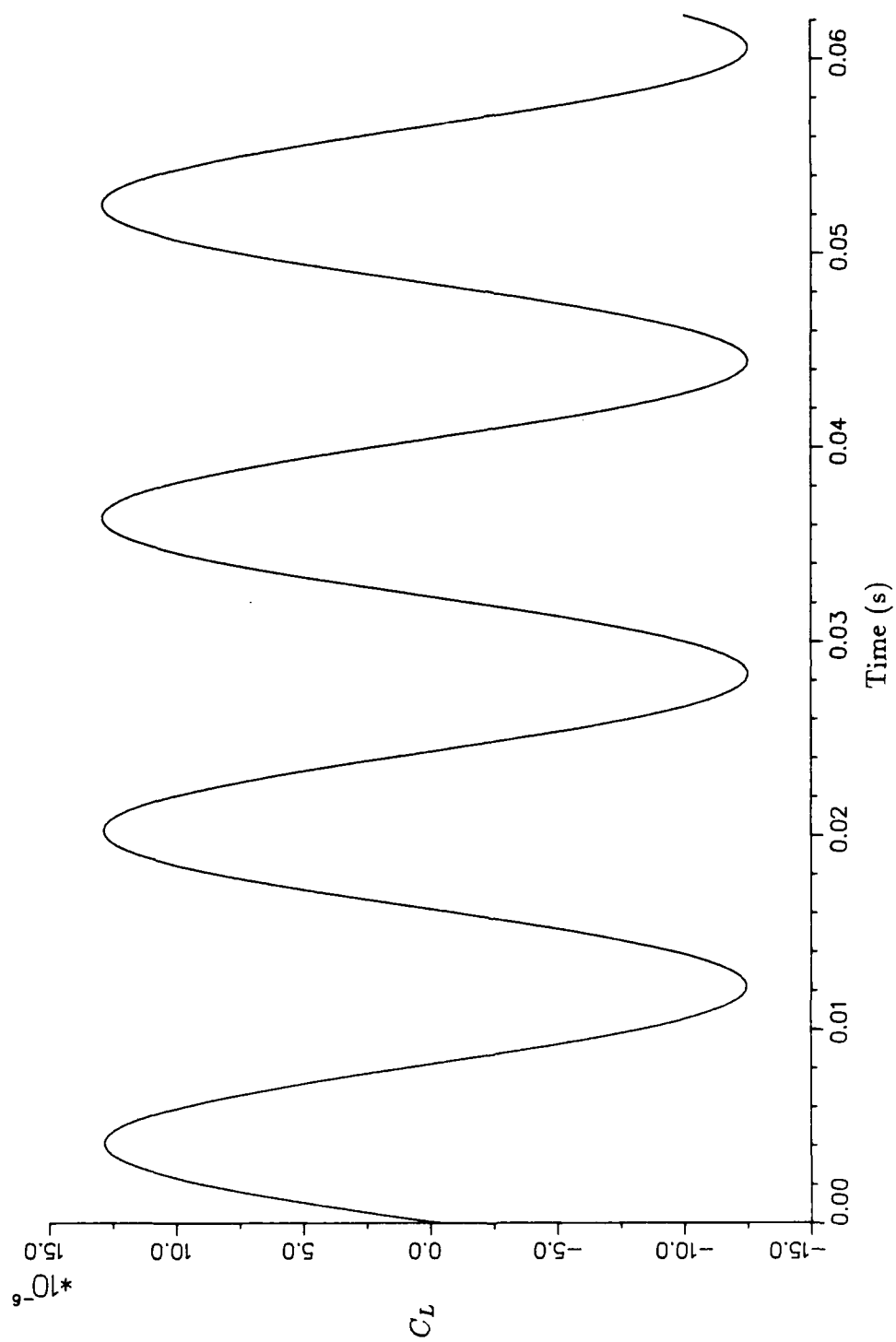
FIGURE 4.12: Variation in Lift Coefficient Over Time for $Re = 7826$.

CHAPTER V

RESULTS FOR VORTEX SHEDDING
FROM A FLAT PLATE

The subsequent discussion describes the results obtained for the case of vortex shedding from a flat plate in a uniform flow. Several comparisons are made with data obtained by Roshko for this geometrical configuration. The effects of changing parameters associated with the finite–difference solution of the flow field are also examined.

Computational Setup

The numerical prediction of vortex shedding from a flat plate in a uniform flow was achieved on for different grid configurations. The coarser of the grids used in the study was a 60 × 50 uniform grid as shown in Figure 5.1. Overall physical dimensions of the calculation domain were 0.06 m × 0.03 m. The flat plate was composed of 10 vertical cells, had a length of 0.006 m, and was centered vertically within the calculation domain. The spacing between the plate and the upper and lower boundaries was approximately two plate lengths. An inlet boundary was provided at approximately 2.5 plate lengths upstream of the plate, and the exit boundary was placed approximately 7.5 plate lengths downstream of the plate.

A finer grid was also employed in the solution of this problem. The second grid was a highly nonuniform 150 × 80 grid as shown in Figure 5.2. Nonuniformity was introduced to concentrate the control volumes in the area of greatest interest, that area being the region directly downstream of the plate. Also, the nonuniformity allows for the placement of relatively large cells near the boundaries which locate the boundaries farther away from the plate to reduce the influence of boundary conditions. The overall dimensions of the calculation domain were 0.175 m × 0.140 m. The flat plate was composed of 16 equally spaced vertical cells which gave a plate length of 0.0102 m. Vertical spacing between the plate and the outer boundaries was approximately 6.4 plate lengths at both the top and bottom. Upstream of the plate by about two plate lengths was an inlet boundary, and approximately 15 plate lengths downstream of the plate was an exit boundary.

Boundary conditions for the two grid sizes were similar in nature. The upper and lower boundaries were assigned a symmetry (slip wall) condition. The inlet boundary was a uniform flow directed normal to the plate with the magnitude of the velocity being varied from 0.3 m/s to 3.0 m/s to achieve a range of Reynolds numbers of approximately $2000 \leq Re \leq 30000$. The exit boundary was set by allowing the boundary to assume a velocity profile similar to the one directly upstream as described in Chapter III.

The FORDC-2 program was executed on the VAX 8650 and VAX 11/780 computers available at the Texas Tech computing facilities. The problem was solved isothermally with the calculated variables being u, v, and p. Runs were also made for the coarse grid case with the k-ϵ turbulence model included in the solution, which results in the addition of the variables k and ϵ to the process. Turbulence

was employed to determine whether there was a significant difference in the results between the turbulent and laminar cases. The different grids were employed to examine the effects of a refined grid on the solution and to determine whether the extra effort required to create and run the more complex grid was justified. Finally, the time step, Δt, was adjusted on a case by case basis to ensure convergence of the transient solution.

Method of Inducing Vortex Shedding

A significant problem arose in computationally simulating the Kármán vortex street. Geometrically, the problem has a symmetry about the horizontal line which bisects the flat plate. Since the finite–difference model is simply a mathematical model, the flow field that results would share this symmetry about the horizontal bisector. This symmetry would seemingly exclude the vortex street pattern from the set of possible solutions.

Fortunately, this problem can be overcome by removing the symmetry in the initial conditions. To make the flow initially asymmetric, a perturbation was added to the flow in the form of a momentum source. The momentum source was included for the first three time steps and was located at a control volume directly behind and at the upper limit of the plate. The location of the source was approximately the same location at which the transient velocity, u_1, was measured as shown in Figure 4.6. Inclusion of this momentum source proved to be an adequate method of introducing asymmetry to the flow; consequently, the vortex street was predicted by the program.

Qualitative Analysis of Transient
Vector Fields

Prediction of the Kármán vortex street by the FORDC-2 program is clearly demonstrated by Figures 5.3–5.7. These figures show the absolute velocity vectors for equally separated increments in time. The five plots progress by steps of a quarter of the vortex shedding period, P, to show the progression of the vector field with time. Absolute velocity vectors are displayed simply because the vortex shedding pattern is far more apparent when shown in this manner. The velocity vectors are transformed by the simple relation

$$\mathbf{v_{abs}} = \mathbf{v} - \mathbf{U_\infty} \quad . \tag{5.1}$$

At $t = 0$ (Figure 5.3), the familiar alternating vortex pattern of the vortex street is clearly visible. In fact, the pattern shown has much the same character as that given in Figure 1.1. There is a pronounced spreading of the vortices in the vertical direction as they move downstream. Also note that the vortices seemingly grow in size as they progress downstream. These characteristics indicate that the finite–difference code accurately predicts the vortex shedding pattern.

Progressing to $t = 1/4P$ (Figure 5.4), notice that the entire flow pattern from $t = 0$ has moved downstream. There is also a disturbance at the top of the plate which is the beginning of the formation of the next vortex. At $t = 1/2P$ (Figure 5.5), the vortex on the top of the plate has formed and is clearly recognizable. As expected, at $t = 1/2P$ the vector field appears to be a mirror image about the horizontal bisector of the field at $t = 0$. The vector field at $t = 3/4P$ (Figure 5.6) indicates the beginning of the formation of a new vortex at the bottom of the plate.

Finally, at $t = P$ (Figure 5.7) the vector field appears to be the same field calculated at $t = 0$. Therefore, the vector field has cyclicly progressed back to its initial state, and the predicted vortex shedding is indeed periodic.

Comparison of Numerical and Experimental Strouhal Numbers

Among the most critical parameters associated with periodic vortex shedding is the Strouhal number. Roshko provided extensive data on the Strouhal numbers for different geometries, including the flat plate. Figure 5.8 offers a quantitative comparison of the experimental results of Roshko with the results from this study. The data presented graphically are also given in tabular form as Tables 5.1 and 5.2.

A quick examination of Figure 5.8 indicates that the numerical model predicted Strouhal numbers comparable to those measured by Roshko. However, a closer examination reveals some important trends in the data. For the detailed 150×80 grid, the prediction of Strouhal number was quite accurate up to a Reynolds number of approximately 10^4. For Reynolds numbers greater than 10^4, the model seemed to lose accuracy as the predicted Strouhal number decreased. In any case, the error between the predicted and experimental results never exceeded 15 percent.

For the case of the 60×50 grid the same trend was not apparent. For the entire Reynolds number range, the coarser grid appears to have predicted Strouhal numbers more consistent with Roshko's results. The Strouhal numbers predicted on the coarse grid were generally greater than those predicted on the fine grid. Addition of the $k-\epsilon$ turbulence model generally caused a slight increase in the Strouhal number; however, that trend was not substantiated for all cases.

Overall, the results were favorable, especially when compared with the work done by Younis. In a similar study, Younis predicted Strouhal numbers for a flat plate in a range of 0.165–0.185. Younis' values would appear to be an overestimate of the Strouhal number when compared with the experimental data provided by Roshko. Overestimation of the Strouhal was not a problem encountered in the current study.

Comparison of Numerical and Experimental
Wake Pressure Profiles

Roshko provided experimental results for the time averaged pressure distribution on the centerline of the wake. His data was for the specific Reynolds number of $Re = 14500$, and the data was given in terms of the nondimensional quantities C_p and x/l. The quantity x is measured from the plate with positive x extending downstream. A comparison with Roshko's data was made for both grid sizes and for the case where turbulence was included.

Figure 5.9 gives the variation in C_p with downstream distance for the fine grid. The most obvious difference between the computational and experimental curves is the magnitude of the suction predicted by the numerical model just downstream of the plate. The numerical model predicted a base pressure coefficient nearly twice as large as Roshko measured. Note that the numerical model predicted the minimum pressure to occur at $x/l \approx 0.7$ where the experimental results indicate that the minimum pressure occurs at $x/l \approx 2.0$. Minimum pressure values were also quite different, with the predicted minimum taking a value approximately twice that of the experimental result. However, this does not necessarily indicate an error in the numerical model, because Roshko cited difficulties in obtaining the wake pressure

measurements. Furthermore, note that the agreement between the curves for $x/l >$ 2.0 was quite good.

The anomalies cited for the fine grid solution are also apparent in the coarse grid solution as shown in Figure 5.10. The predicted base pressure coefficients for the two grids are almost identical. Minimum pressure for the two cases also occurred at nearly the same value of x/l, though the coarse grid solution did not predict as low a value of C_p as did the fine grid solution. The primary difference between the solutions for the two grid lies in the accuracy of the solution for values of $x/l > 2.0$. For this region, the fine grid solution was much closer to the experimental solution than was the coarse grid solution. Nonetheless, the coarse grid solution did approximate this part of the curve with reasonable accuracy.

The addition of turbulence to the coarse grid solution appears to make little difference in the solution. The pressure profile for the turbulent case (Figure 5.11) is virtually identical to the laminar case. This result indicates that the addition of turbulence has little effect on the prediction of wake pressures.

Comparison of Numerical and Experimental Aerodynamic Force Coefficients

Measurement of the time averaged lift and drag coefficients was carried out for each case run. As expected, the average lift coefficient, $C_{L_{avg}}$, was zero for all runs though instantaneous values of lift were nonzero. The zero value of lift was expected since this case is for a flat plate at zero angle of attack.

A graphical display of the calculated average drag coefficients is given as Figure 5.12. Also included on the plot are drag coefficients derived from Roshko's data and the equations given in Chapter II. Note the extreme difference between the

numerical solution and the experimental/theoretical values provided by Roshko. The numerical values of C_D exceed Roshko's values by more than 50 percent, and this may well be tied to the much lower base pressure predicted by the computations. However, also note that the predicted values agree favorably with the numerical results of Younis who found C_D's in the range of 3.25–3.65.

From a numerical standpoint there were also significant differences in the predicted drag coefficients. The fine grid solution estimated drag coefficients on the order of 10 percent greater than the coarse grid. This fact may be related to the lower minimum pressure found in the wake for the fine grid solution. Turbulence appeared to have little effect on the prediction of drag, though its addition did seem to generally increase the drag coefficient by about 1 percent.

<div align="center">Effect of Iterative Time Step Size</div>

From a numerical standpoint, the selection of the iterative time step Δt can be critical. Figure 5.13 presents the variation in the predicted Strouhal number for various iterative time step sizes. The horizontal line indicates the experimentally measured Strouhal number for this particular Reynolds number, $Re = 14500$. A best fit linear approximation of the data is also displayed. Note that the curvature in the curve fit is due to the logarithmic axis.

From this figure one can clearly see the dependence of the solution on the time step. The prediction of the Strouhal number deteriorates markedly as the time step is increased. For this particular case, any further increase in the time step above Δt = .0008 led to divergence of the solution. Also note that as $\Delta t \to 0$ the predicted solution asymptotically approaches the experimental solution. These indicate that the choice of a sufficiently small value of Δt is critical in obtaining accurate solutions.
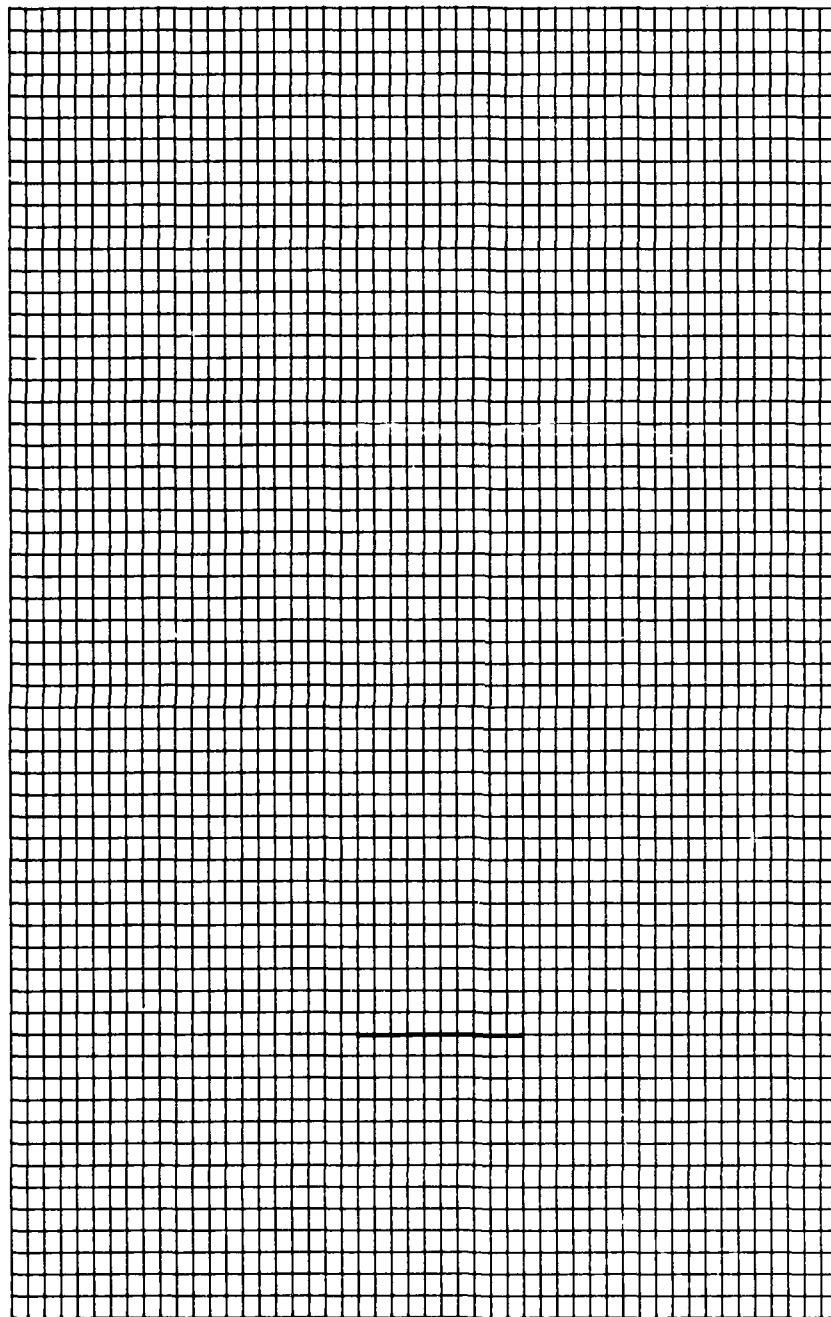
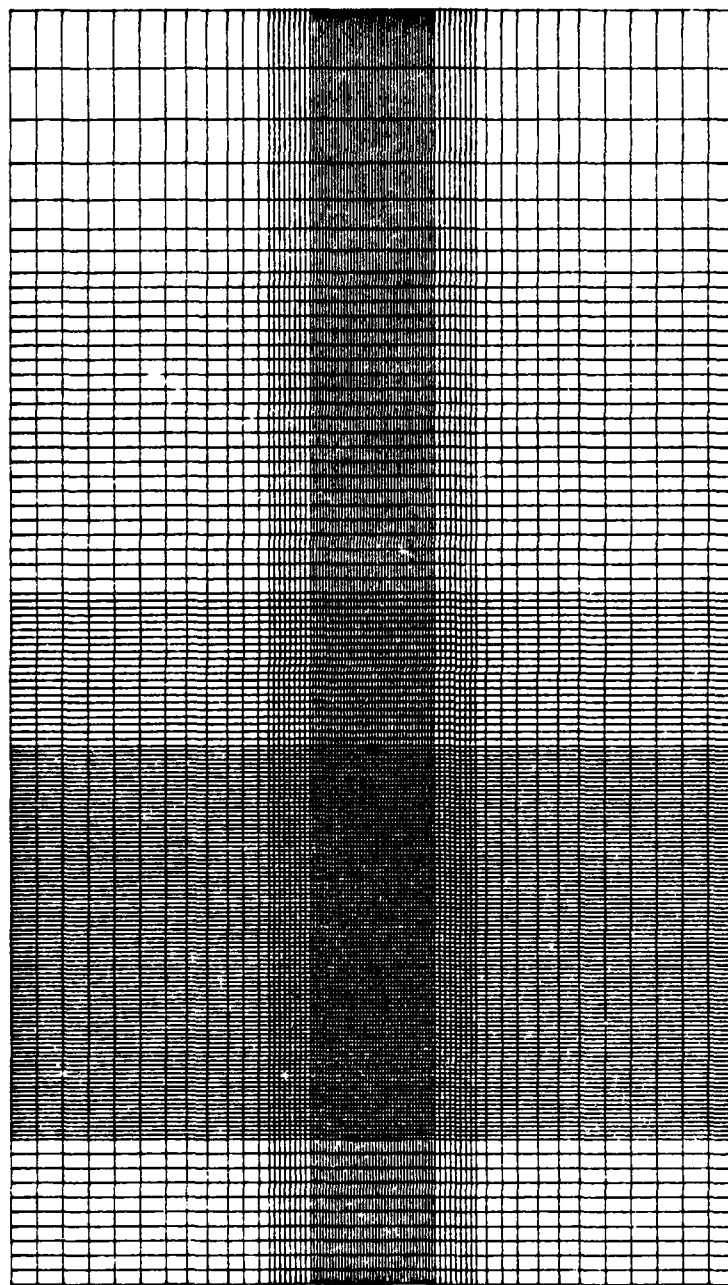FIGURE 5.1: 60×50 Finite–Difference Grid (Coarse Grid).

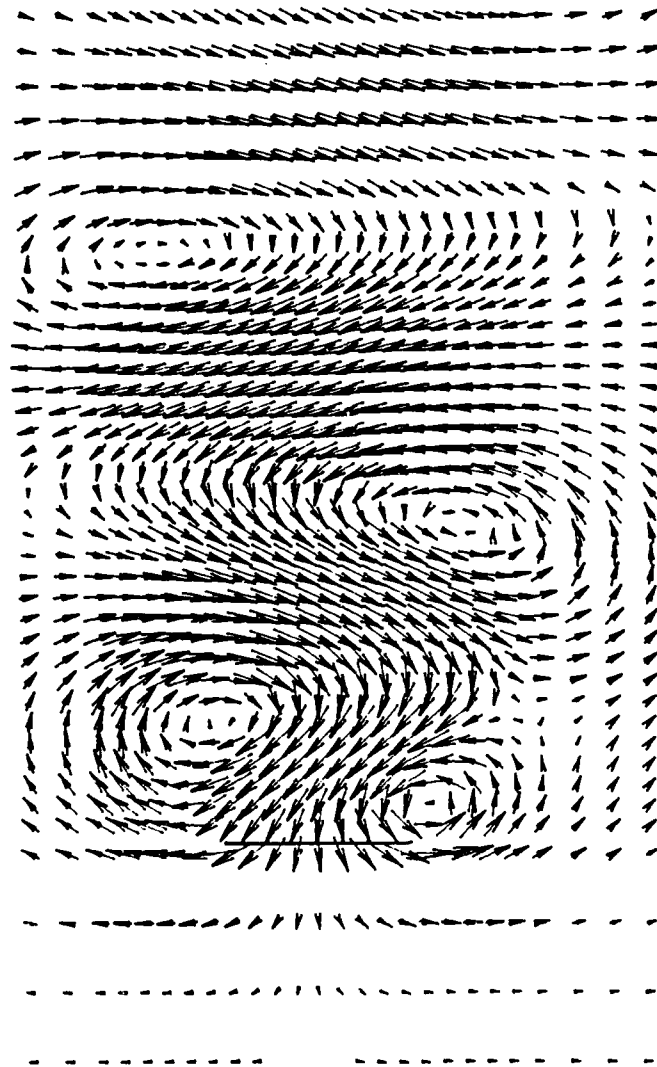FIGURE 5.2: 150 × 80 Finite–Difference Grid (Fine Grid).

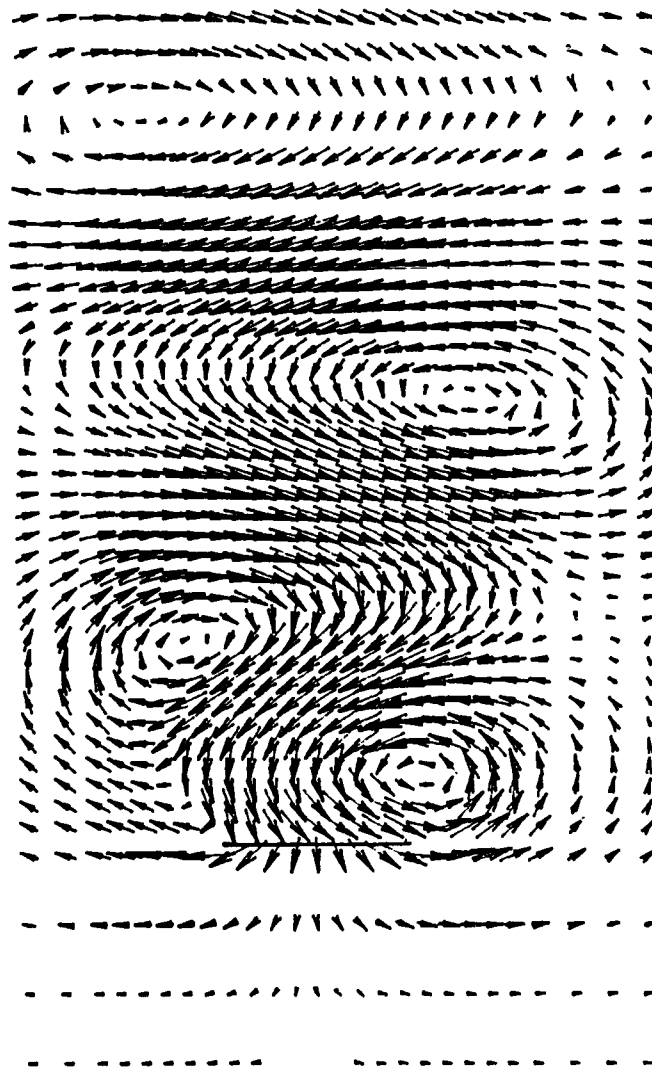FIGURE 5.3: Absolute Velocity Vectors at $t = 0$.

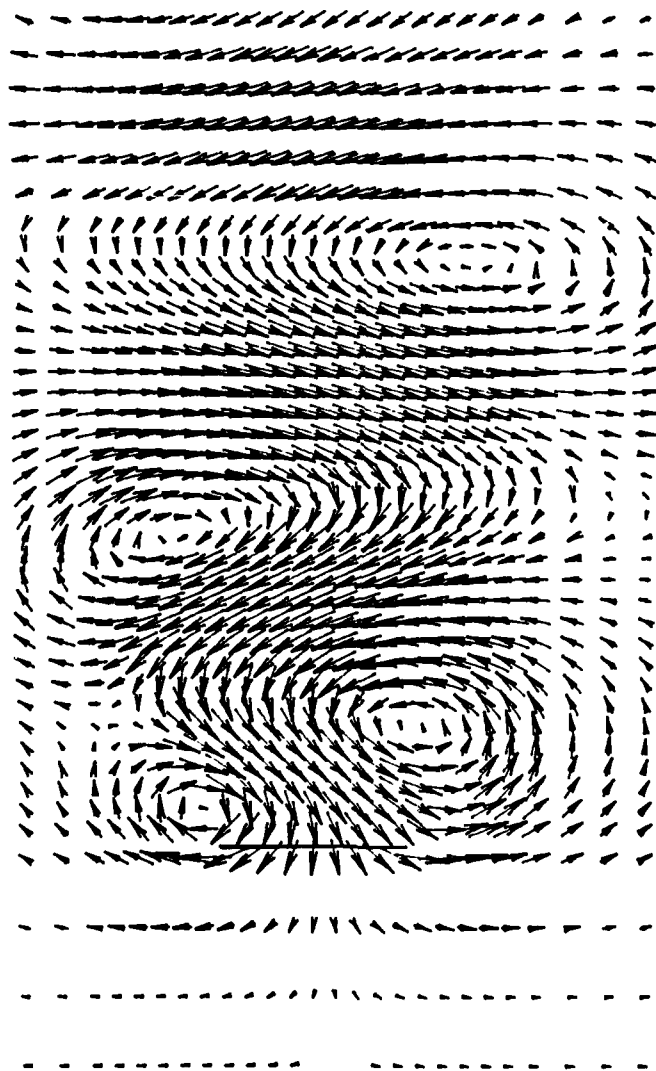FIGURE 5.4: Absolute Velocity Vectors at $t = \frac{1}{4}P$.

FIGURE 5.5: Absolute Velocity Vectors at $t = \frac{1}{2}P$.
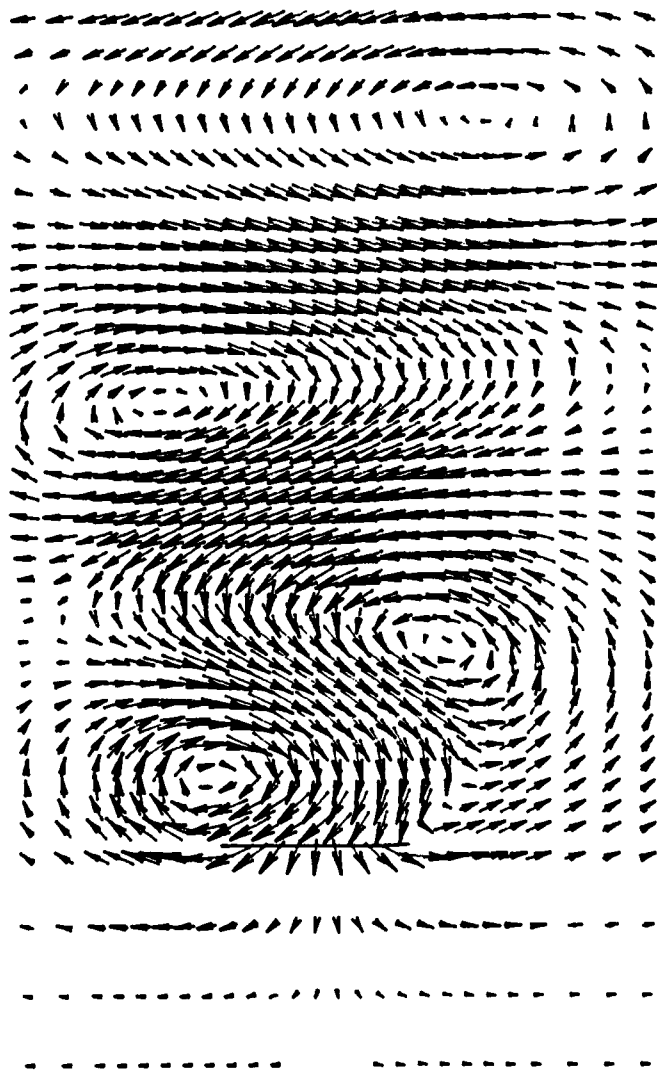
FIGURE 5.6: Absolute Velocity Vectors at $t = \frac{3}{4}P$.
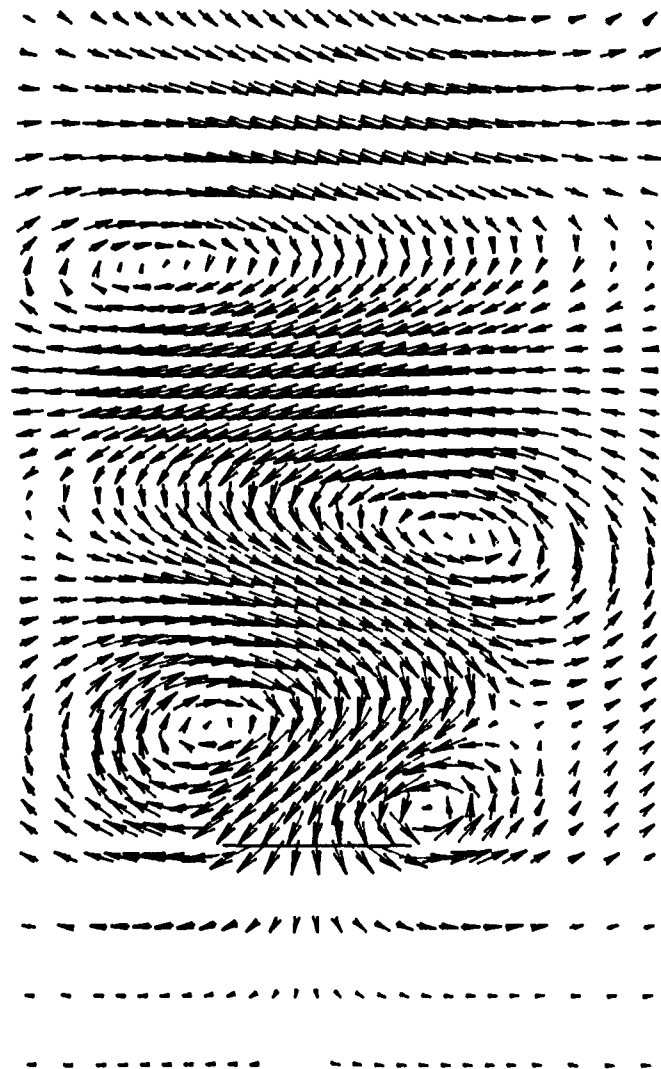
FIGURE 5.7: Absolute Velocity Vectors at $t = P$.
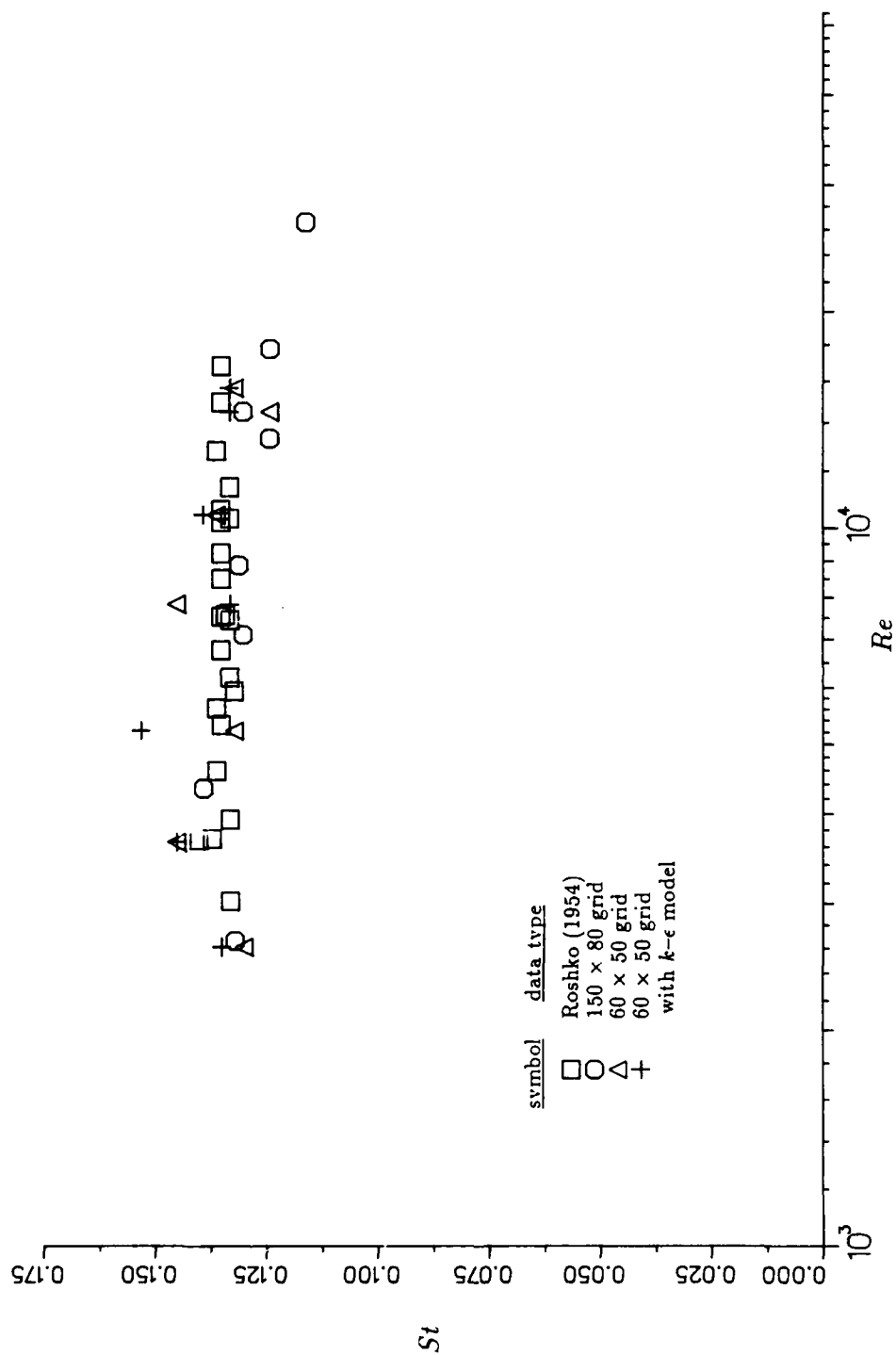
FIGURE 5.8: Strouhal Number vs. Reynolds Number
for a Flat Plate.

TABLE 5.1: Numerical Shedding Frequency and
Aerodynamic Force Data for the
150 × 80 Grid.

U_∞ (m/s)	Re	St	$C_{D_{avg}}$	$C_{L_{avg}}$
0.30	2660	0.132	3.30	0.0
0.50	4435	0.139	3.35	0.0
0.80	7096	0.129	3.30	0.0
1.00	8870	0.132	3.26	0.0
1.50	13304	0.124	3.20	0.0
1.63	14500	0.130	3.23	0.0
2.00	17739	0.124	3.23	0.0
3.00	26609	0.116	3.24	0.0

TABLE 5.2: Numerical Shedding Frequency and Aerodynamic Force Data for the 60×50 Grid.

Flow Condition		Without Turbulence			With Turbulence		
U_∞ (m/s)	Re	St	$C_{D_{avg}}$	$C_{L_{avg}}$	St	$C_{D_{avg}}$	$C_{L_{avg}}$
0.50	2608	0.130	2.93	0.0	0.135	2.96	0.0
0.70	3652	0.145	2.96	0.0	0.145	2.95	0.0
1.00	5217	0.132	2.94	0.0	0.153	2.98	0.0
1.50	7826	0.145	2.96	0.0	0.133	2.95	0.0
2.00	10435	0.136	2.96	0.0	0.139	2.96	0.0
2.78	14500	0.124	2.92	0.0	0.133	2.97	0.0
3.00	15652	0.132	2.93	0.0	0.133	2.93	0.0

FIGURE 5.9: Centerline Wake Pressure Distribution for 150 × 80 Grid at $Re = 14500$.
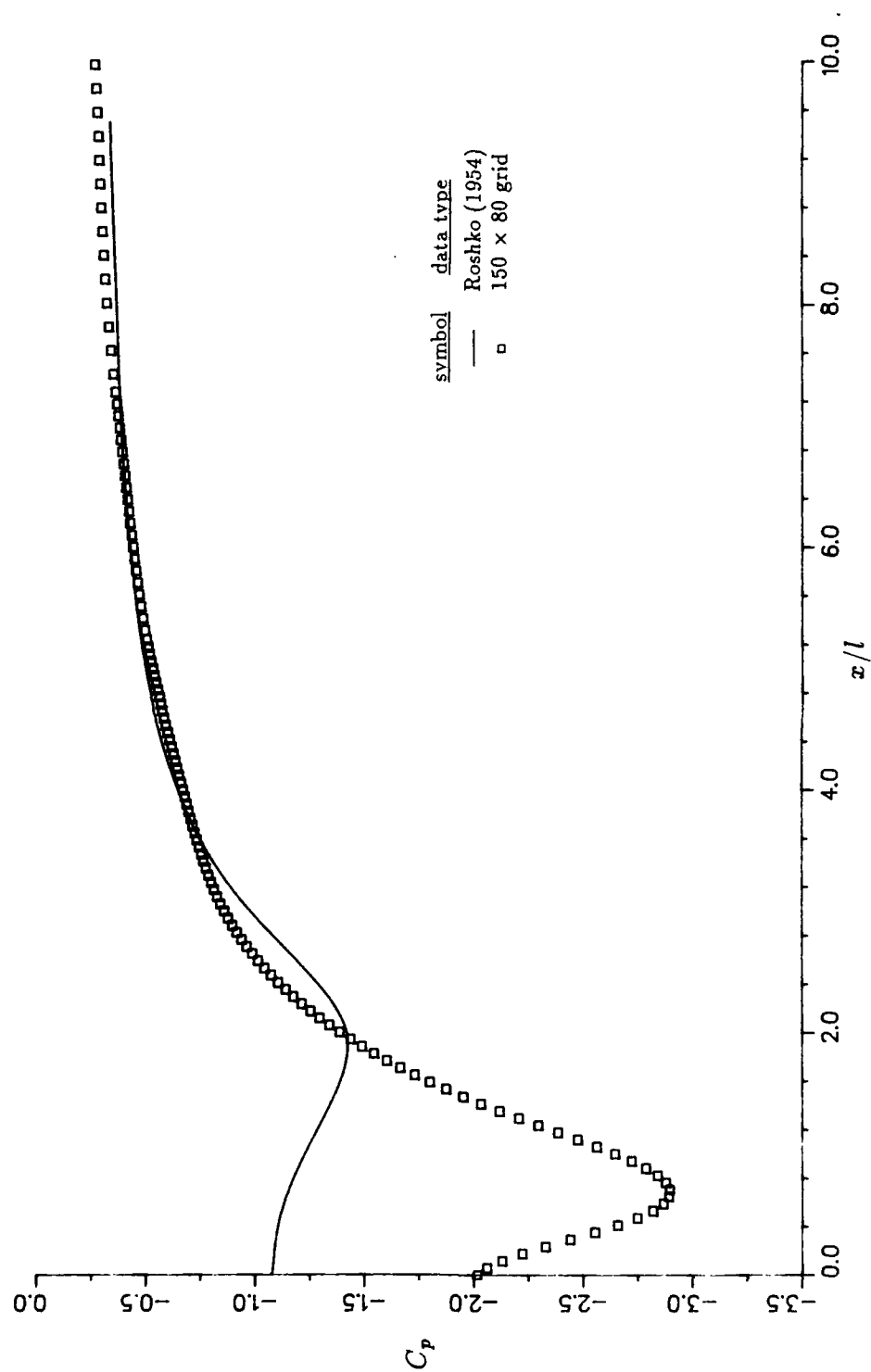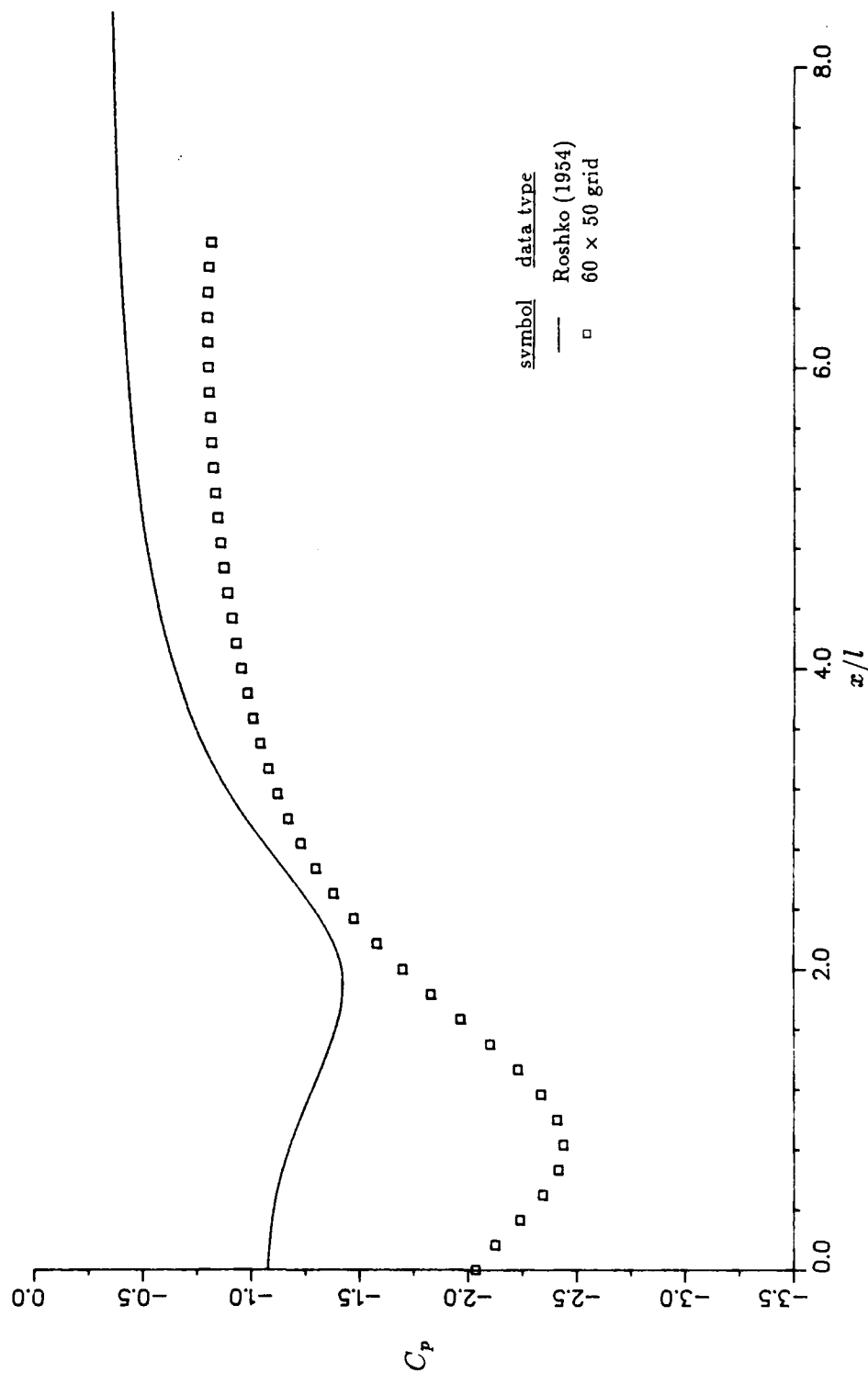
FIGURE 5.10: Centerline Wake Pressure Distribution for 60×50 Grid at $Re = 14500$.
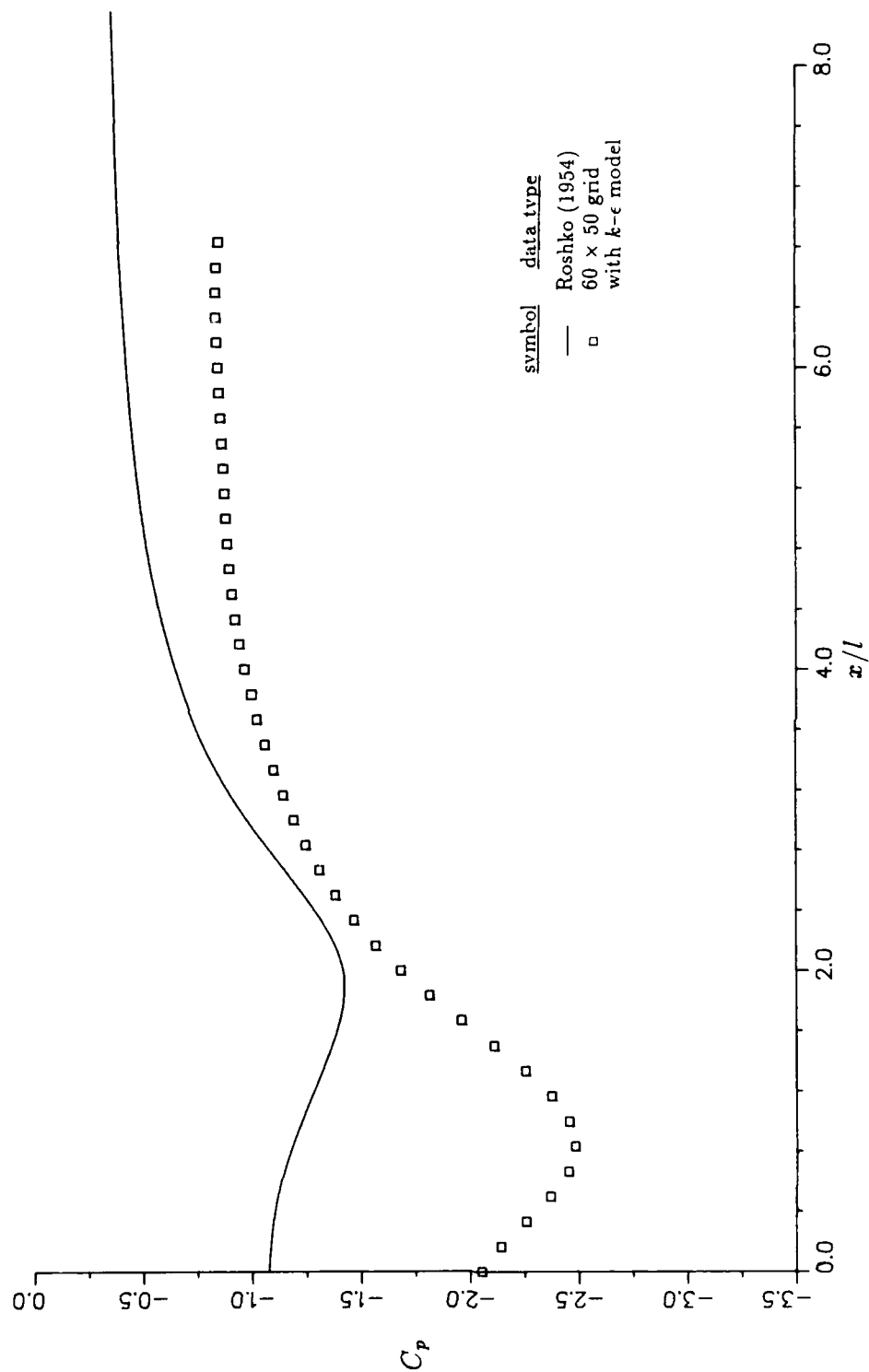
FIGURE 5.11: Centerline Wake Pressure Distribution for 150×80 Grid with k-ϵ Turbulence Model at $Re = 14500$.

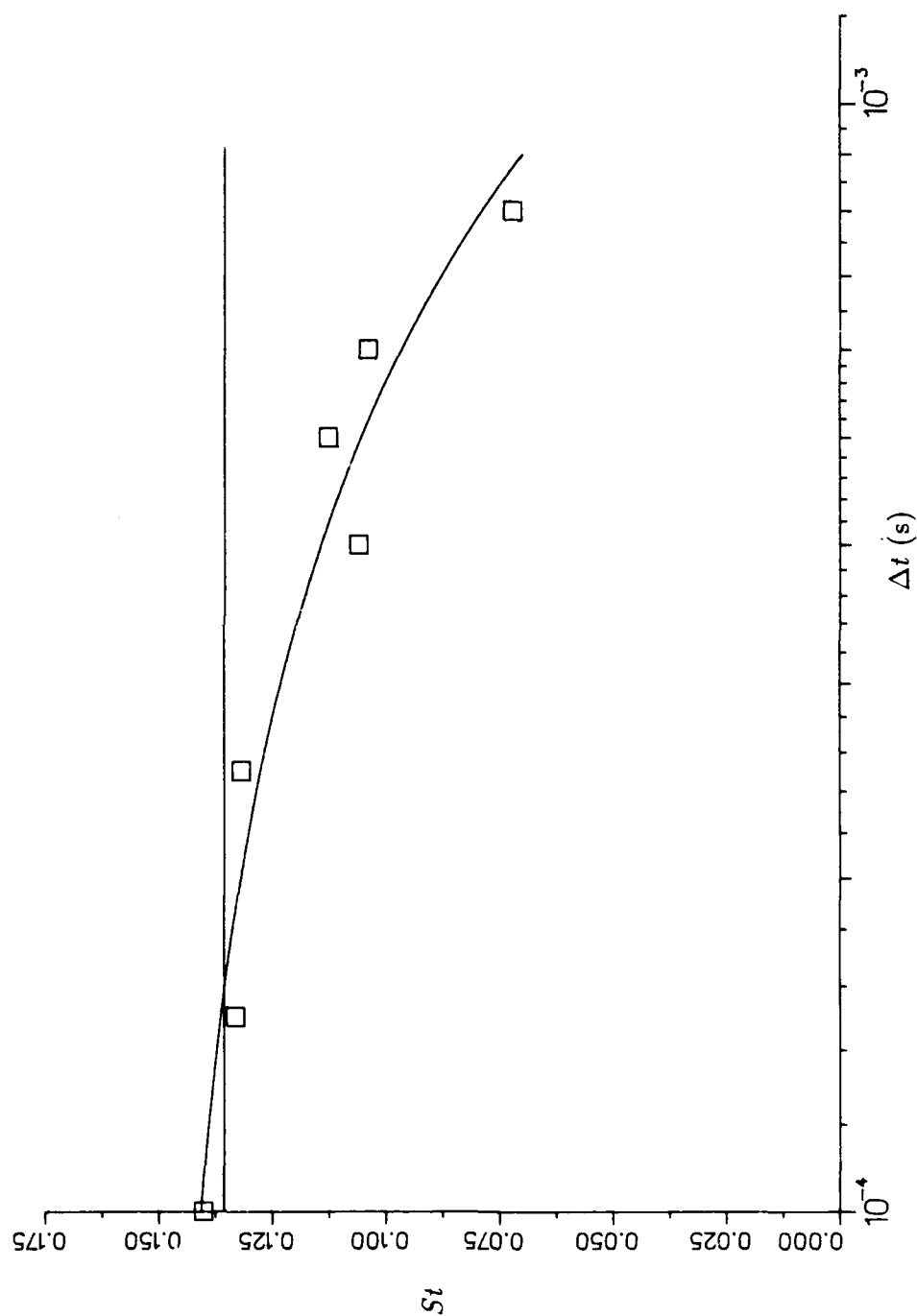FIGURE 5.12: C_D vs. Reynolds Number for a Flat Plate.

FIGURE 5.13: Effect of Iterative Time Step on the Predicted Strouhal Number ($Re = 14500$).

CHAPTER VI

RESULTS FOR VORTEX SHEDDING FROM
A FLAT PLATE NEAR A GROUND PLANE

The following discussion describes the results obtained for the case of a flat plate near a ground plane. A comparison is made between the predicted Strouhal numbers and the function obtained by Matty. The effect of the presence of the ground plane on the aerodynamic force coefficients is also examined.

Computational Setup

The numerical prediction of vortex shedding from a flat plate near a ground plane was carried out on only one grid configuration. This is due to the fact that results in Chapter V indicated that refinement of the grid yielded only limited improvements in the solution. However, the 60×50 grid used in the previous case proved to be unacceptable due to a lack of spacing between the plate and the exit boundary. To remedy this problem, cells were added to the grid downstream of the plate.

The grid employed for this problem was a 80×50 grid as shown in Figure 6.1 with overall dimensions of 0.08 m $\times$ 0.03 m. The plate was composed of 12 vertical cells and had a length of 0.0072 m. The inlet boundary was located approximately two plate heights upstream of the plate, and the exit was located approximately

nine plate heights downstream of the plate. The location of the bottom boundary relative to the plate was governed by the parameter λ which was assigned the values of 0, 1/4, 1/2, and 1. The spacing between the plate and the upper boundary varied between 2 and 3 plate heights for different values of λ.

Boundary conditions for this case were similar to those presented in Chapter V. The primary difference was the placement of an impermeable wall at the bottom boundary. Otherwise, the boundaries remained the same with the exception of the magnitude of the inlet velocities. The inlet velocity was varied between 2.0 m/s and 20.0 m/s to give a range of Reynolds numbers of approximately $1000 \leq Re \leq 15000$. This range of Reynolds numbers was chosen to match the range examined by Matty.

Vortex shedding was induced in the same method explained in Chapter V. Turbulence was not included in this case due to the previous results which indicated that the addition of turbulence was of little consequence. Again, the solution was isothermal, and the calculated variables were u, v, and p.

Qualitative Analysis of the Flow Field

Inducing vortex shedding in the wake of a flat plate near a ground plane was not successful for all cases. For the case of $\lambda = 0$, vortex shedding was never achieved. To achieve vortex shedding, the plate had to be moved to a distance of one plate length from the wall. At this distance from the wall, vortex shedding occurred readily. To achieve shedding for other values of λ, the velocity field of the $\lambda = 1$ case was imposed as an initial condition.

Figure 6.2 and A.2 respectively present representative plots of the velocity vectors and streamlines for an instant in time. This particular plot is for the case of $\lambda = 1$. The main difference to note between this case and the cases presented in

Chapter V is a decrease in the wake width. This is apparently due to the influence of the wall which deters the vortices shed from the bottom of the plate from spreading.

Comparison of Numerical and Experimental
Strouhal Numbers

Data obtained for the various values of λ are provided as Tables 6.1–6.3. A comparison of the predicted Strouhal number data versus the function $St(Re, \lambda)$ obtained by Matty is provided in Figures 6.3–6.5.

For the greatest separation between the plate and the ground plane at $\lambda = 1$ (Figure 6.3), the numerical prediction of the Strouhal number for the entire range of Reynolds numbers was fairly accurate. As the Reynolds number was increased, the numerical solution tended to give a slightly higher value of the Strouhal number than the function $St(Re, \lambda)$. However, the Strouhal number generally decreased for increasing Reynolds number as indicated by Matty's study.

As the value of λ was decreased to $\lambda = 1/2$ (Figure 6.4), the trend changed considerably. Predicted values of the Strouhal number were lower than those given by the function $St(Re, \lambda)$ for low values of the Reynolds number. However, as the Reynolds number was increased the numerical solution was quite accurate. The trend of decreasing Strouhal number with increasing Reynolds number was also supported by the prediction. The results were also similar for $\lambda = 1/4$ (Figure 6.5), though predicted Strouhal numbers slightly underestimated the empirical relation. Nonetheless, the trend of decreasing Strouhal number with increasing Reynolds number was again supported.

The variation in the Strouhal number with λ for a fixed value of the Reynolds number was also examined. Strouhal numbers for $\lambda = 1/4$ were generally greater

than those for $\lambda = 1/2$. Matty's data indicates a similar behavior between these values of λ. However, the predicted Strouhal numbers at $\lambda = 1$ were significantly higher than those at $\lambda = 1/2$, though Matty's study indicates that these values should be nearly equal. The difference here may well lie in the fact that Matty's study was for a three–dimensional plate, while the numerical study was two–dimensional.

Variation in Aerodynamic Forces with Ground Clearance

A variation in the aerodynamic forces was noted for changes in the parameter λ. However, for a given value of λ, there was little apparent dependence of the drag force on the Reynolds number. Figure 6.6 presents the variation in the drag coefficient with λ. The trend for the drag to increase as λ decreases was clearly apparent. At $\lambda = 0$, the drag had attained a value approximately 50 percent greater than that obtained for a flat plate removed from a ground plane. This behavior was expected, for the increase in the drag on a body as it approaches a ground plane is well documented.

An increase in lift also occurred for decreasing ground heights, though the trend was not as prominent as it was for the drag. Figure 6.7 presents the variation in the lift coefficient with λ revealing this relationship. The lift appeared to have a slight dependence on the Reynolds number, with an increase in Reynolds number being accompanied by a decrease in the lift coefficient. However, it must be noted that the magnitude of the lift coefficient was quite small, and the lift may be considered to be insignificant.
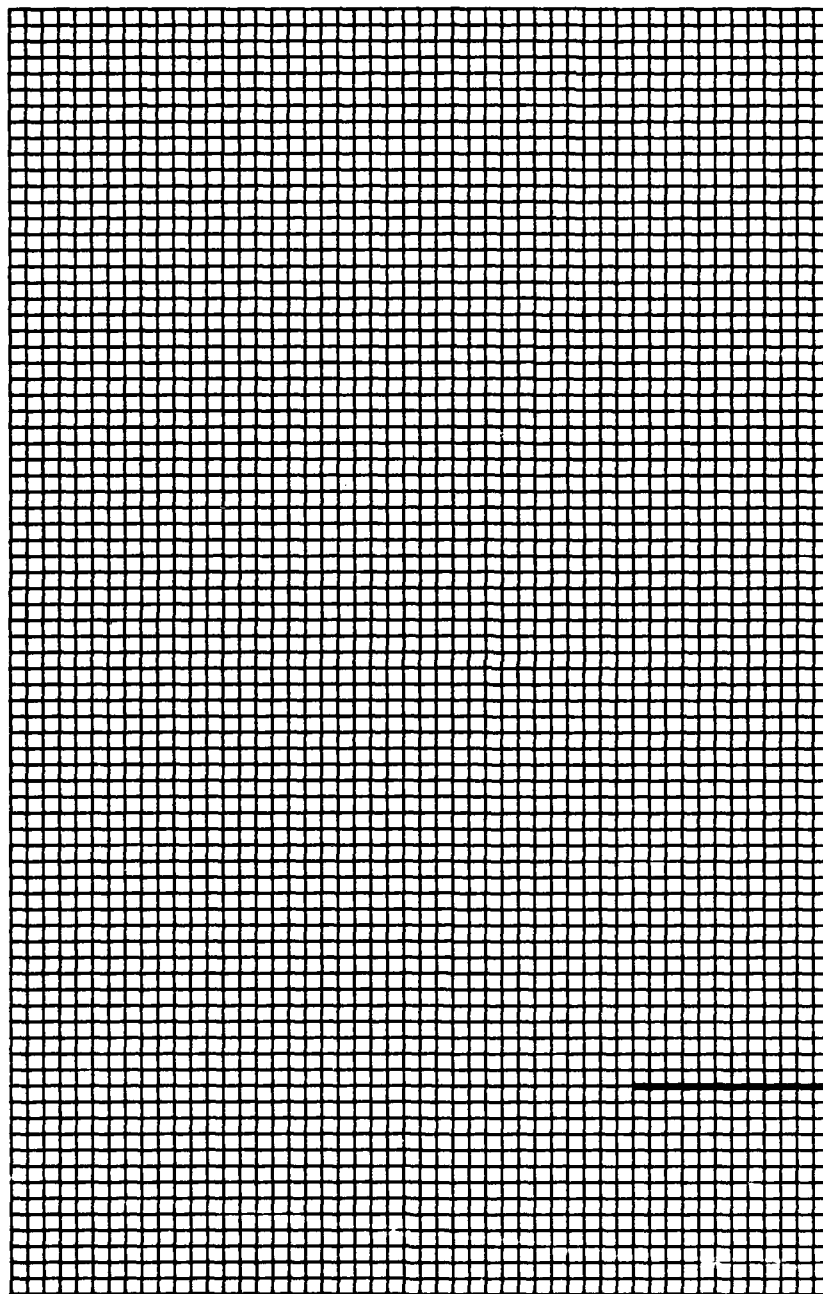
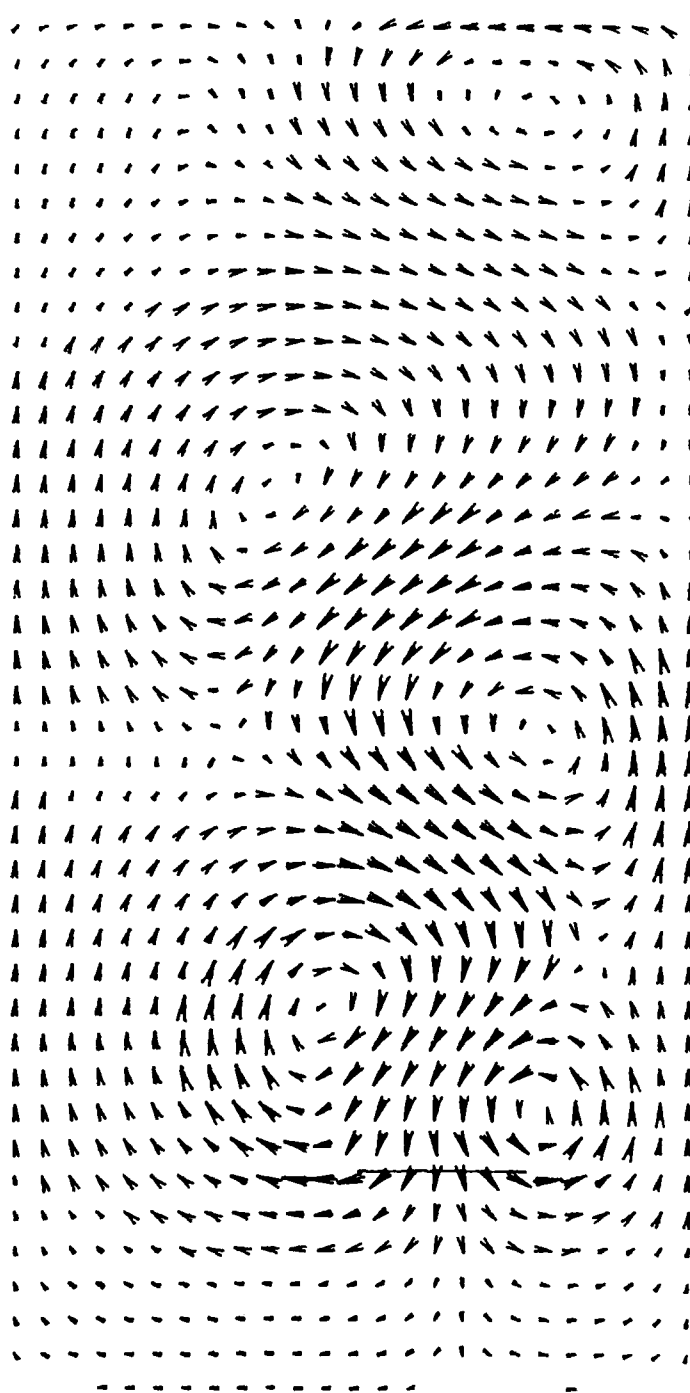FIGURE 6.1: 80×50 Finite-Difference Grid ($\lambda = 0$).

FIGURE 6.2: Absolute Velocity Vectors for $\lambda = 1$.

TABLE 6.1: Numerical Shedding Frequency and
Aerodynamic Force Data for $\lambda = 1$.

U_∞ (m/s)	Re	St	$C_{D_{avg}}$	$C_{L_{avg}} \times 10^{-4}$
2.0	12521	0.148	3.62	2.4
5.0	31304	0.135	3.60	2.4
10.0	62608	0.157	3.61	1.9
15.0	93913	0.160	3.60	1.7
20.0	125210	0.164	3.59	1.5

TABLE 6.2: Numerical Shedding Frequency and
Aerodynamic Force Data for $\lambda = 1/2$.

U_∞ (m/s)	Re	St	$C_{D_{avg}}$	$C_{L_{avg}} \times 10^{-4}$
2.0	12521	0.130	3.72	3.1
5.0	31304	0.127	3.72	2.9
10.0	62608	0.126	3.70	2.7
15.0	93913	0.126	3.69	2.5
20.0	125210	0.117	3.76	2.4

TABLE 6.3: Numerical Shedding Frequency and
Aerodynamic Force Data for $\lambda = 1/4$.

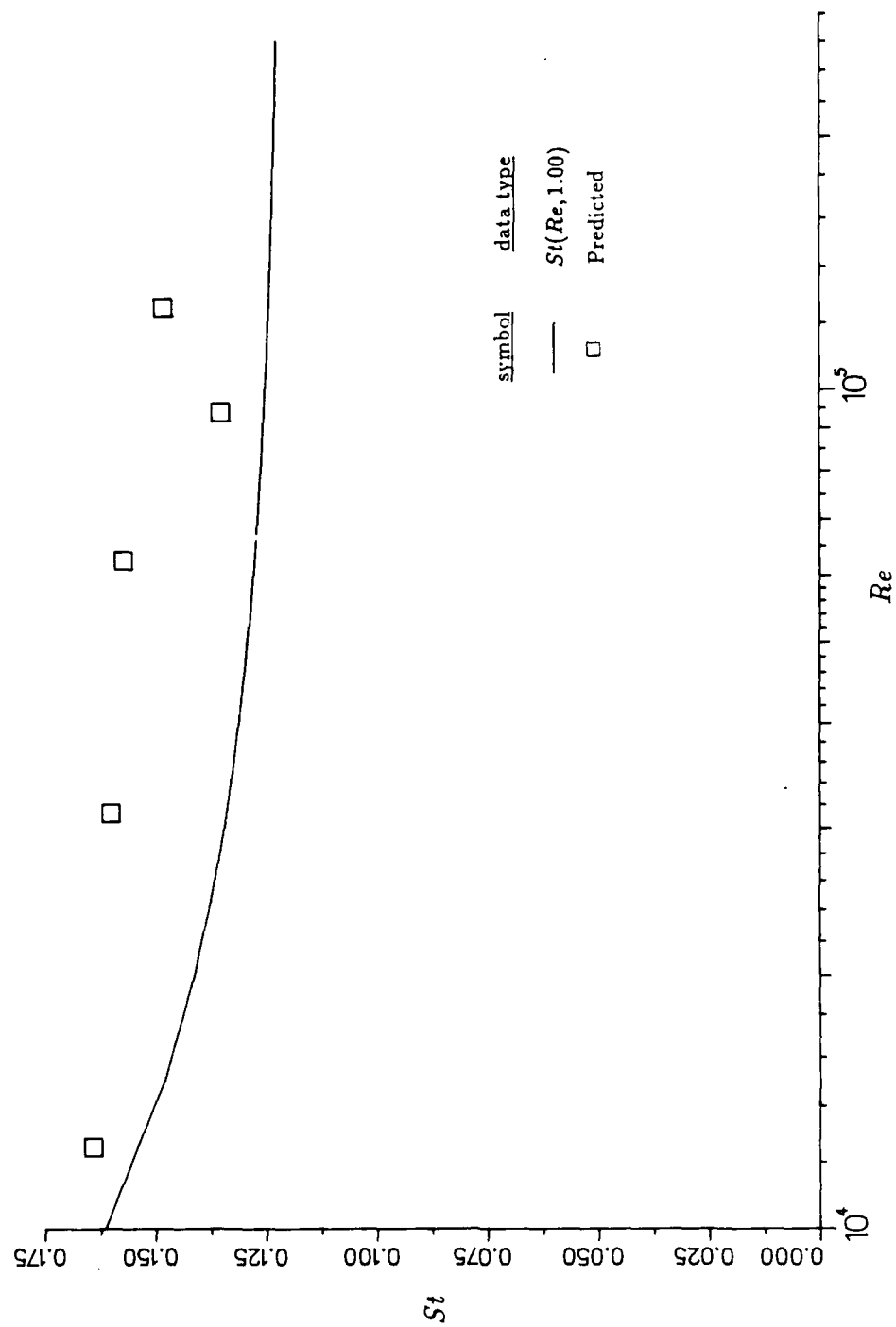| U_∞ (m/s)	Re	St	$C_{D_{avg}}$	$C_{L_{avg}} \times 10^{-4}$
2.0	12521	0.138	4.06	3.3
5.0	31304	0.135	4.07	3.2
10.0	62608	0.132	4.06	2.9
15.0	93913	0.130	4.04	2.7
20.0	125210	0.130	4.06	2.4

FIGURE 6.3: Strouhal Number vs. Reynolds Number
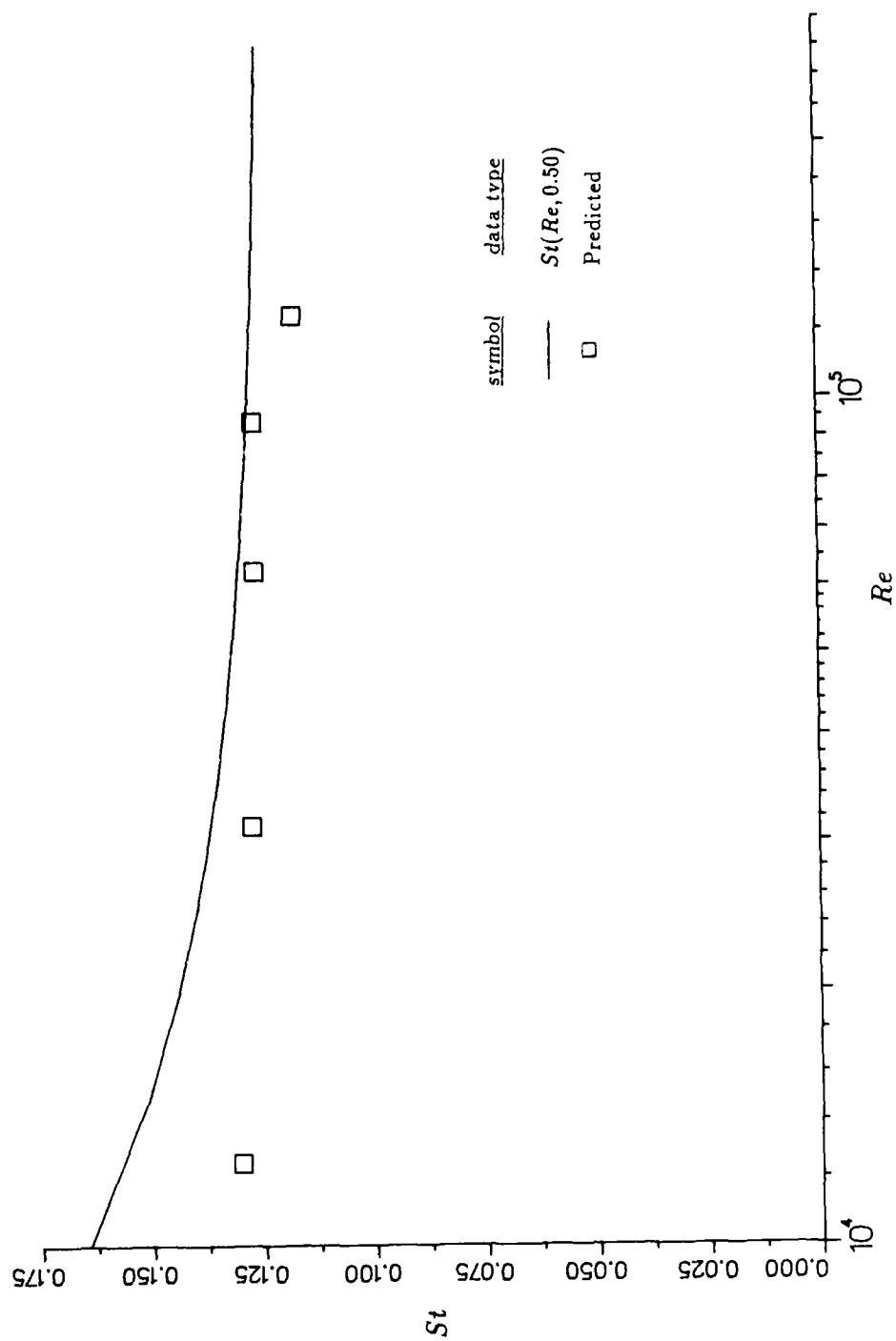for $\lambda = 1$.

FIGURE 6.4: Strouhal Number vs. Reynolds Number
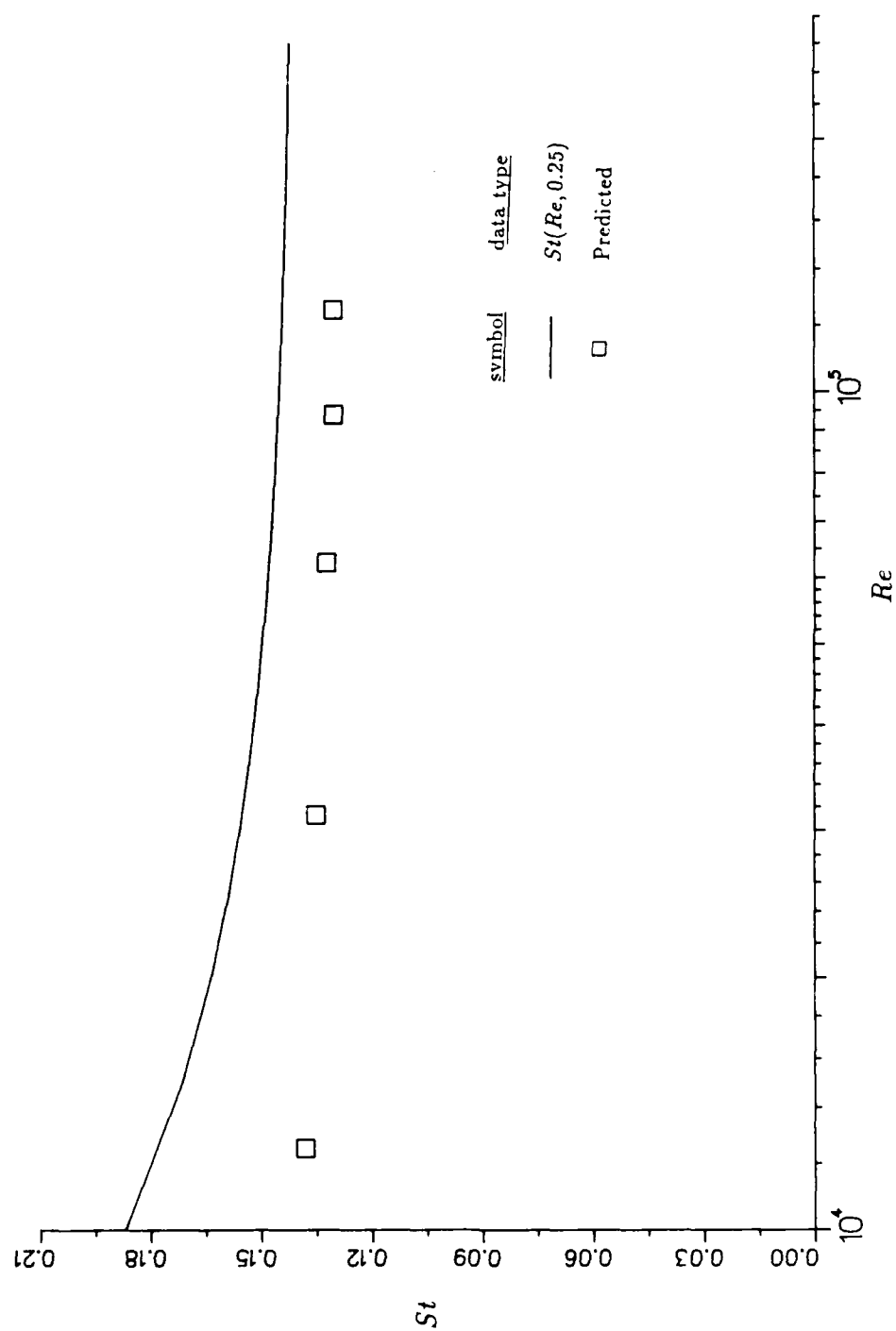for $\lambda = 1/2$.

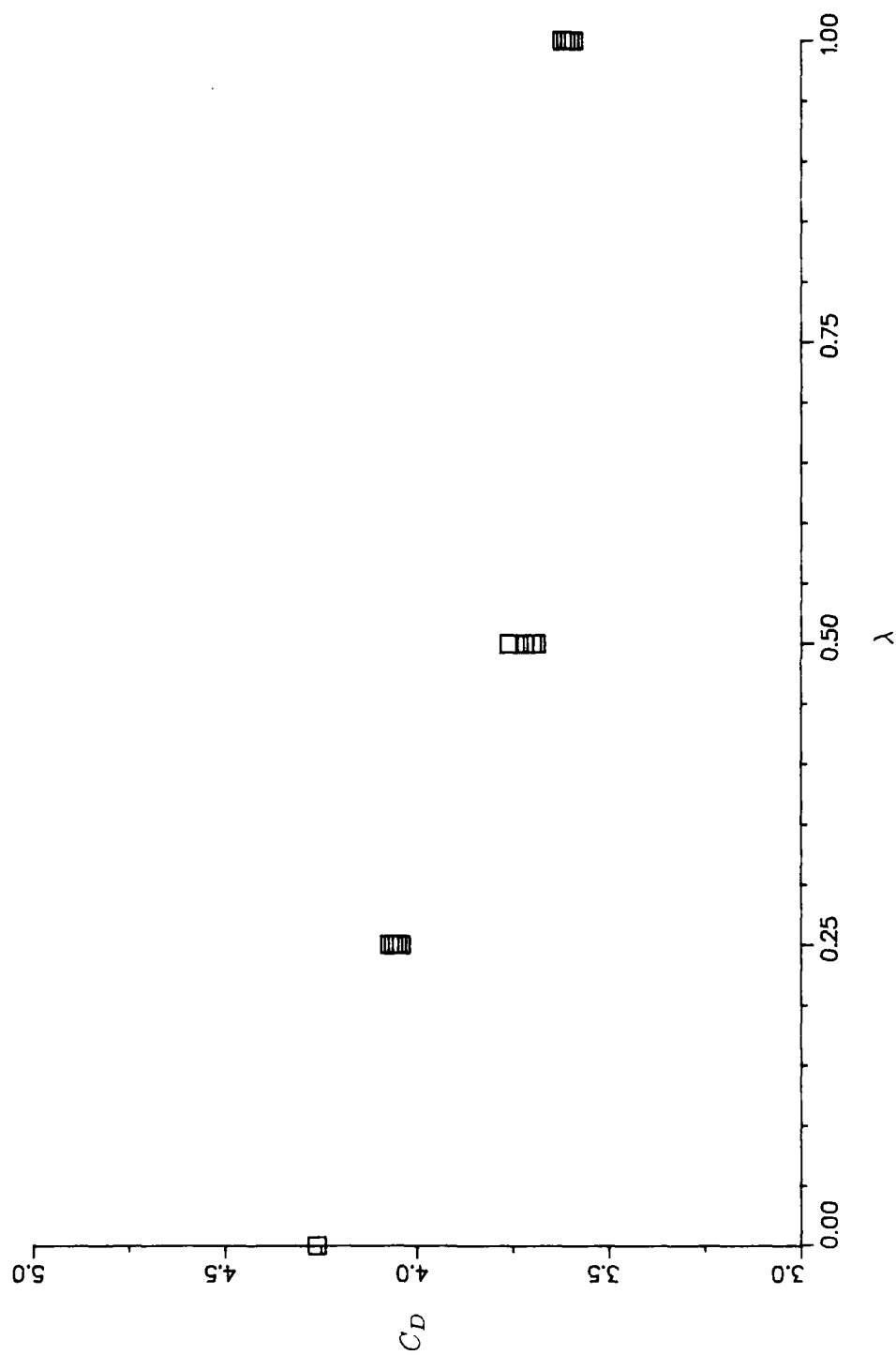FIGURE 6.5: Strouhal Number vs. Reynolds Number
for $\lambda = 1/4$.

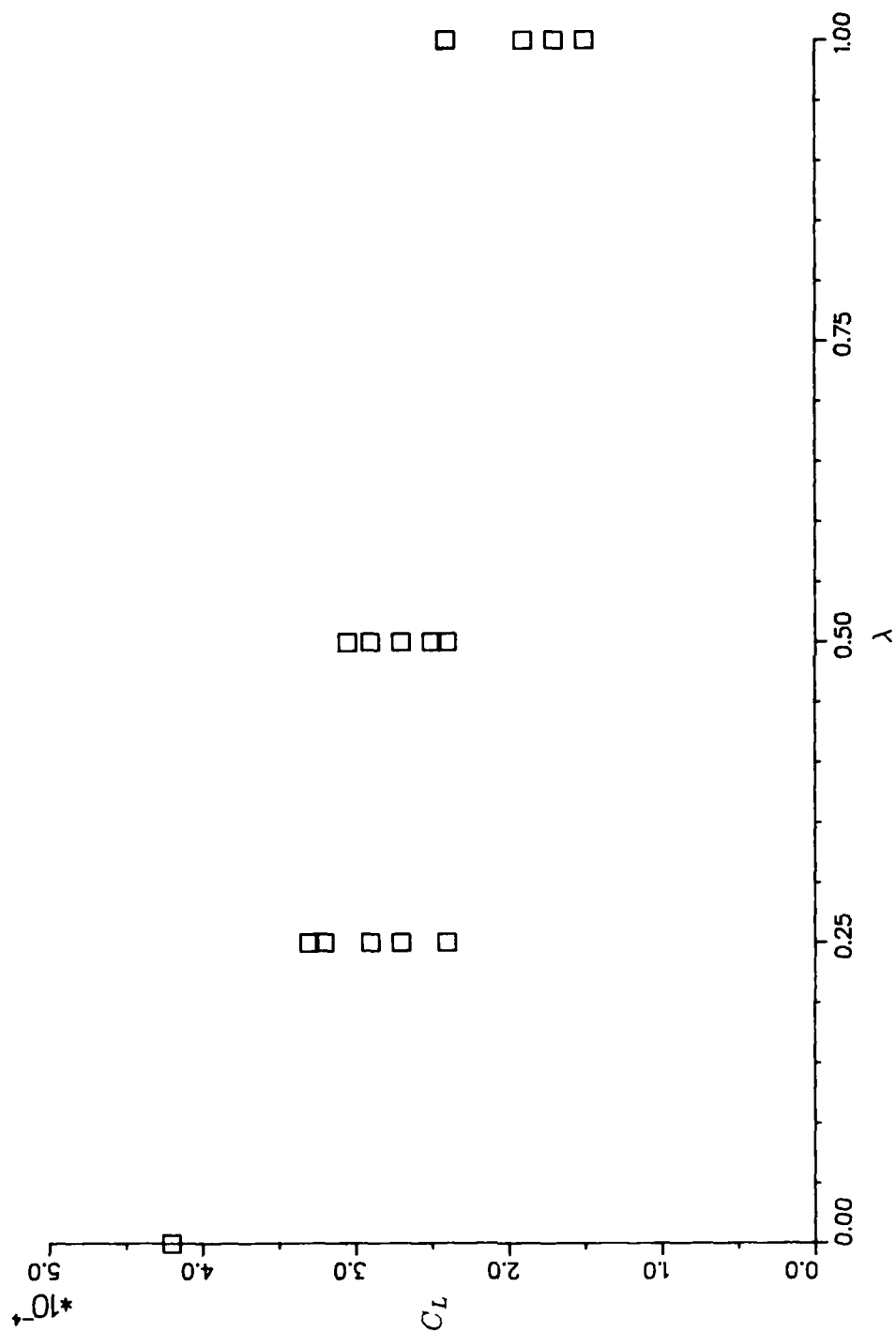FIGURE 6.6: Variation in the Drag Coefficient with Ground Clearance.

FIGURE 6.7: Variation in the Lift Coefficient with Ground Clearance.

CHAPTER VII

RESULTS FOR VORTEX SHEDDING FROM
A RECTANGULAR CYLINDER

The following discussion reviews results of the computational prediction of vortex shedding from rectangular cylinders. Computed Strouhal numbers are compared to experimental values provided by Okajima. Trends in the variations of aerodynamic forces are also explored.

Computational Setup

The numerical prediction of vortex shedding from rectangular cylinders was achieved on the same basic 80 × 50 grid used for the study of a flat plate near a ground plane. The primary differences between the two grids were the placement of the body in the calculation domain and the specification of boundary conditions.

Figure 7.1 presents the finite-difference grid for the specific case of a rectangular cylinder with $\beta = 3$. The study was executed for cylinders of varying length to height ratios, with the β taking on the values 1, 2, and 3. The height of the cylinder was composed of 10 cells giving a height of 0.006 m. The length of the box was composed of either 6, 12, or 18 cells depending on the respective value of β, either 1, 2, or 3. The inlet boundary was located approximately two cylinder heights upstream of the cylinder, and the exit varied from 4.5– 6.5 cylinders heights downstream of the

94

cylinder depending on the value of β. Spacing between the cylinder and the top and bottom boundaries was fixed at approximately two cylinder heights.

Boundary conditions for this case were identical to those for a flat plate in a uniform stream (Chapter V), with the exception of modified inlet velocities. Inlet velocities were varied from approximately 0.04 m/s to 2.80 m/s yielding a Reynolds number range of $200 \leq Re \leq 15000$. This range roughly corresponds to the range of the data presented by Okajima.

Again, the solution was isothermal, and the k–ϵ turbulence model was excluded from the solution process. This provided a solution in terms of the variables u, v, and p.

Qualitative Analysis of the Flow Field

The unusual behavior exhibited in plots of Strouhal number versus Reynolds number for cylinders with aspect rations in the range of $2 \leq \beta \leq 3$ was theorized to be dependent on an overall change in the flow field. It was hoped that the numerical solution of this problem would demonstrate this change in the flow geometry. However, the change in the flow pattern was not at all evident in plots of the velocity vectors and streamlines for the tested cylinders.

Plots of the flow fields for each of the values of β are provided as Figures 7.2–7.4 and Figures A.3–A.5. The plots are all quite similar, and show a pattern very much like that obtained behind a flat plate. These figures are all representative of the flow fields obtained over the entire range of Reynolds numbers for their respective values of β. Unfortunately, the resolution of the solution was not such that the region of reattachment along the cylinder length could be seen for the two latter cases where β took on the values of 2 and 3.

Comparison of Numerical and Experimental
Strouhal Numbers

The most interesting aspect of the shedding of vortices from a rectangular cylinder was the discontinuity that occurred in plots of the Strouhal number versus the Reynolds number. This behavior was predicted by the FORDC–2 code for the expected values of β. Data for these cases is provided in Tables 7.1–7.3.

Figure 7.5 presents the variation in the Strouhal number with Reynolds number for a cylinder with $\beta = 1$. The plot indicates that the Strouhal number was relatively insensitive to the Reynolds number over the entire range of Reynolds numbers. Maximum values of the Strouhal number occurred at minimum values of the Reynolds number. This prediction is supported by the data provided by Okajima which indicates similar trends.

Of greater interest is the case for a cylinder with $\beta = 2$ as shown in Figure 7.6. The Strouhal number increases steadily with increasing Reynolds number up to the point where $Re \approx 600$. The Strouhal number then falls sharply and maintains a fairly constant value over the remainder of the Reynolds number range. This result is in good agreement with experimental results which indicated the same behavior. The prediction of the point where the discontinuity occurred was also very close to the experimental measurements.

The case of the cylinder with $\beta = 3$ shown in Figure 7.7 was similar to the case of $\beta = 2$. Again, the Strouhal number increased with increasing Reynolds number up to a value of $Re \approx 1600$. At this point, the plot then changed discontinuously and the Reynolds number remained reasonably constant over the remainder of the plot. Qualitatively, the behavior of the prediction agrees well with the experimental data provided by Okajima. However, the discontinuity in the plot occurred at a

significantly greater Reynolds number than cited by Okajima. Nonetheless, the prediction of the behavior of the plots of Strouhal number versus Reynolds number for all value of β were reasonably accurate.

Variation in Aerodynamic Force Coefficients

A variation in the aerodynamic force coefficients with both Reynolds number and aspect ratio was indicated by the data. The exhibited trends were more solidly established for drag, with the variation in drag with both Reynolds number and β being quite evident.

Figure 7.8 presents the variation in the drag coefficient for the different values of β. Clearly the drag coefficient decreases for increases in the aspect ratio. This is a trend which was indicated by the study of Laneville and Yong. A variation in drag coefficient with the Reynolds number was also apparent as shown in Figure 7.9. The trend is most clearly seen in the data for the cylinder with $\beta = 2$, where the drag steadily increases with increasing Reynolds number. This is the trend indicated by the data of Davis and Moore. However, this trend was more subtle for the other values of β.

The variations in the lift coefficient with β shown in Figure 7.10 did not exhibit the expected behavior. There are some indications that the lift may increase slightly with increasing β, but the trend is not well established. Even more curious was the variation in the lift with the Reynolds number shown in Figure 7.11. The data in this case clearly indicate that the lift decreases for increases in the Reynolds number. Data provided by Davis and Moore indicates a relationship between the lift and Reynolds number inverse to that derived in this study.
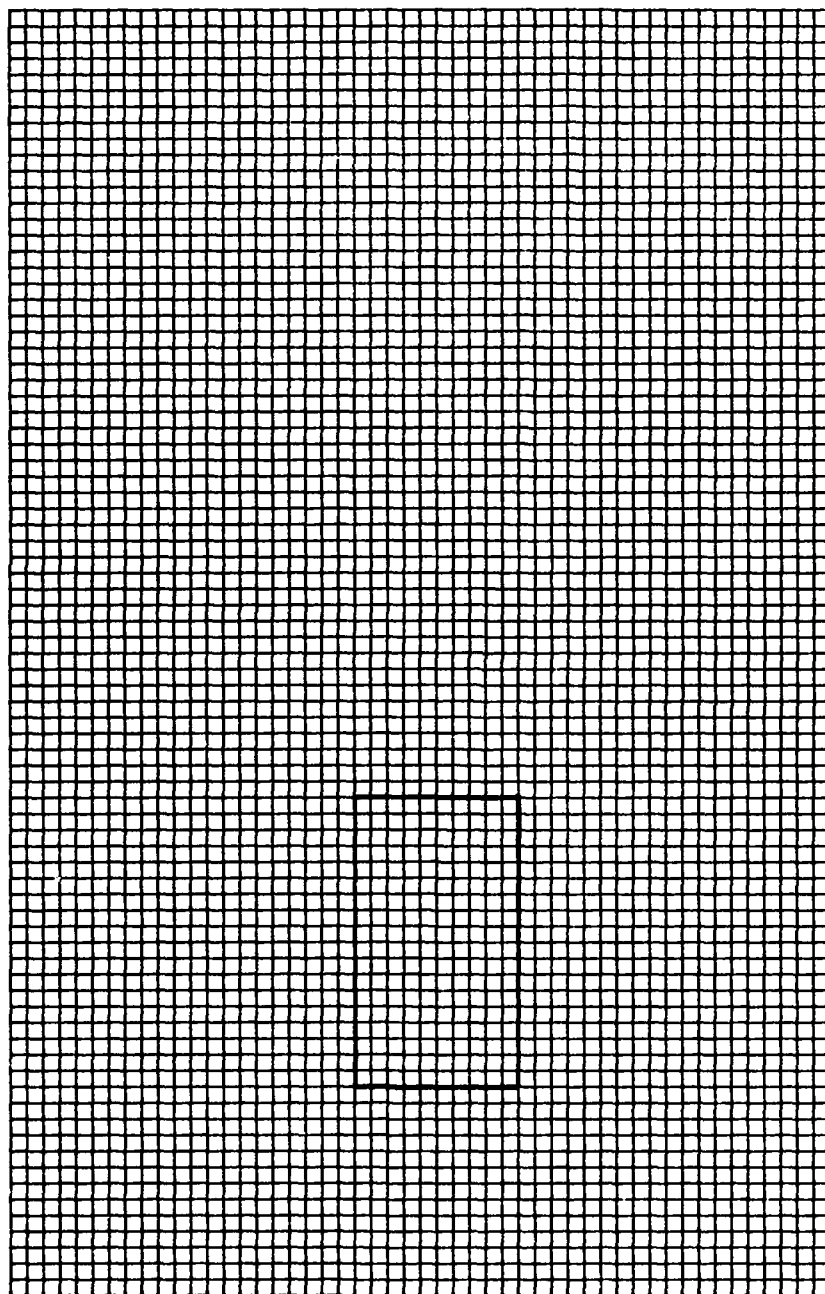
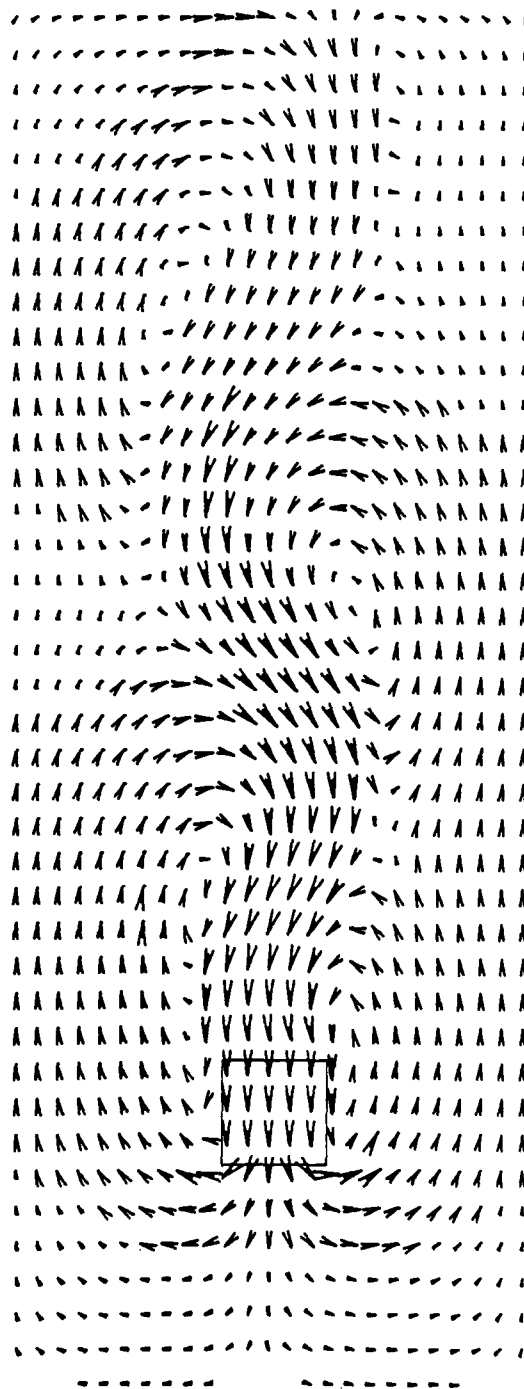FIGURE 7.1: 80 × 50 Finite–Difference Grid ($\theta = 3$).

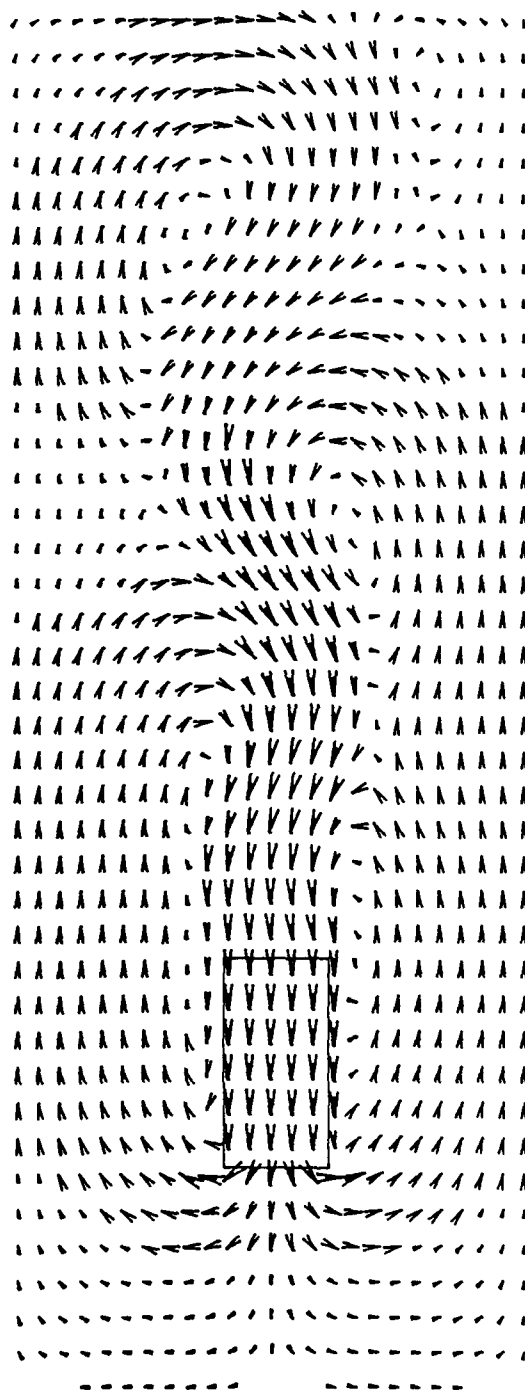FIGURE 7.2: Absolute Velocity Vectors for $\beta = 1$.

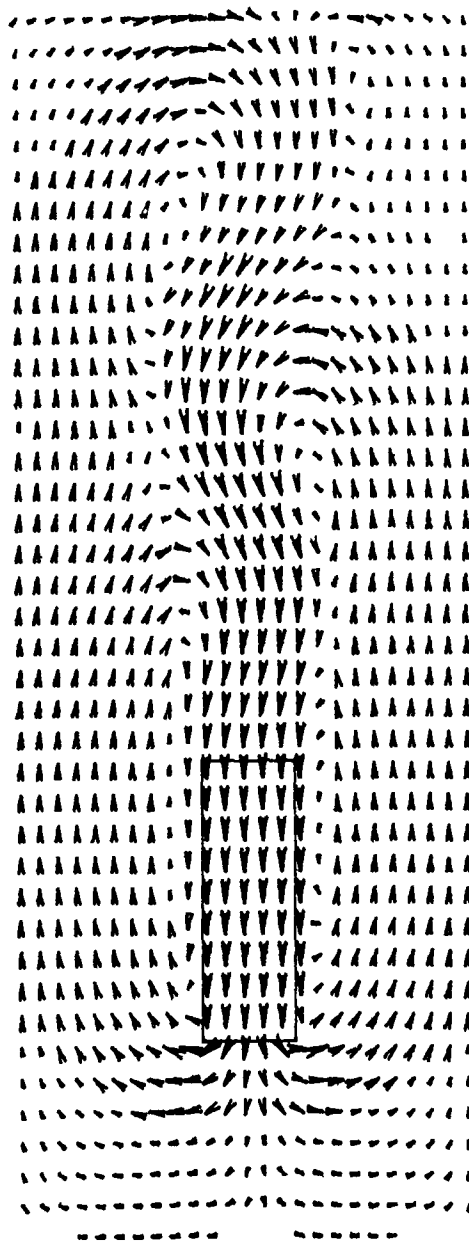FIGURE 7.3: Absolute Velocity Vectors for $\beta = 2$.

FIGURE 7.4: Absolute Velocity Vectors for $\beta = 3$.

TABLE 7.1: Numerical Shedding Frequency and
Aerodynamic Force Data for $\beta = 1$.

U_∞ (m/s)	Re	St	$C_{D_{avg}}$	$C_{L_{avg}}$
0.10	522	0.143	1.88	0.00
0.30	1565	0.143	1.90	0.02
0.50	2609	0.129	1.89	0.00
0.80	4174	0.138	1.89	0.00
1.00	5217	0.130	1.95	0.04
1.50	7826	0.136	1.93	0.00
2.00	10435	0.123	1.90	0.00
2.78	14500	0.138	1.89	0.00

TABLE 7.2: Numerical Shedding Frequency and
Aerodynamic Force Data for $\hat{\beta} = 2$.

U_∞ (m/s)	Re	St	$C_{D_{avg}}$	$C_{L_{avg}}$
0.04	209	0.132	1.53	0.23
0.06	313	0.158	1.63	0.17
0.08	417	0.191	1.67	0.18
0.10	522	0.170	1.69	0.16
0.15	783	0.096	1.72	0.07
0.20	1043	0.107	1.75	0.00
0.30	1565	0.122	1.77	0.04
0.50	2609	0.091	1.79	0.05
∩.80	4174	0.118	1.80	0.04
1.00	5217	0.106	1.80	0.04
1.50	7826	0.124	1.81	0.04
2.00	10435	0.110	1.81	0.06

TABLE 7.3: Numerical Shedding Frequency and
Aerodynamic Force Data for $\beta = 3$.

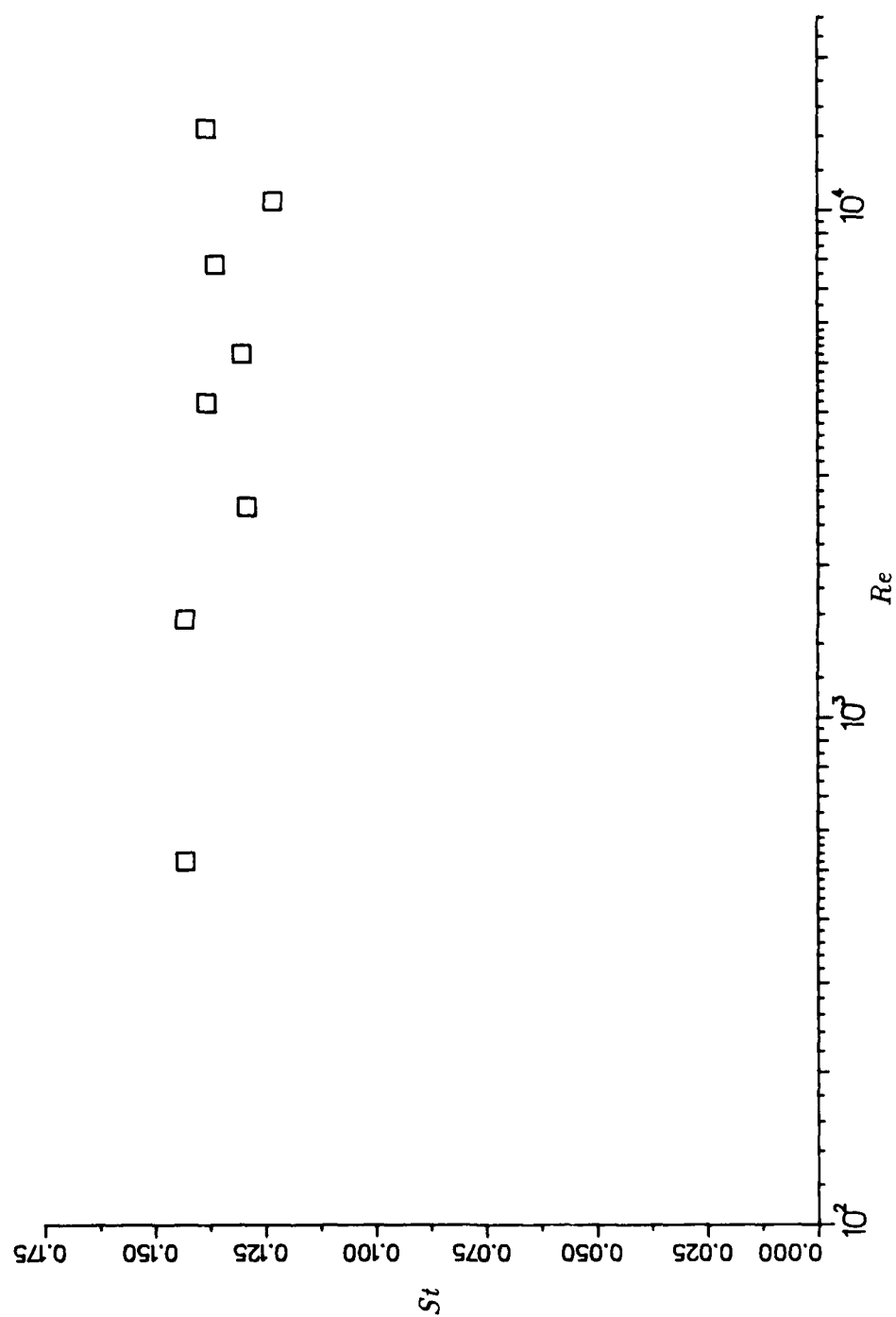| U_∞ (m/s)	Re	St	$C_{D_{avg}}$	$C_{L_{avg}}$
0.08	417	0.144	1.65	0.07
0.10	522	0.143	1.66	0.09
0.20	1043	0.163	1.68	0.09
0.30	1565	0.179	1.69	0.06
0.50	2609	0.150	1.69	0.04
0.60	3130	0.122	1.70	0.02
0.80	4174	0.121	1.70	0.03
1.00	5217	0.129	1.69	0.02
1.25	6522	0.147	1.70	0.02
1.50	7826	0.132	1.68	0.02
2.00	10435	0.115	1.63	0.02

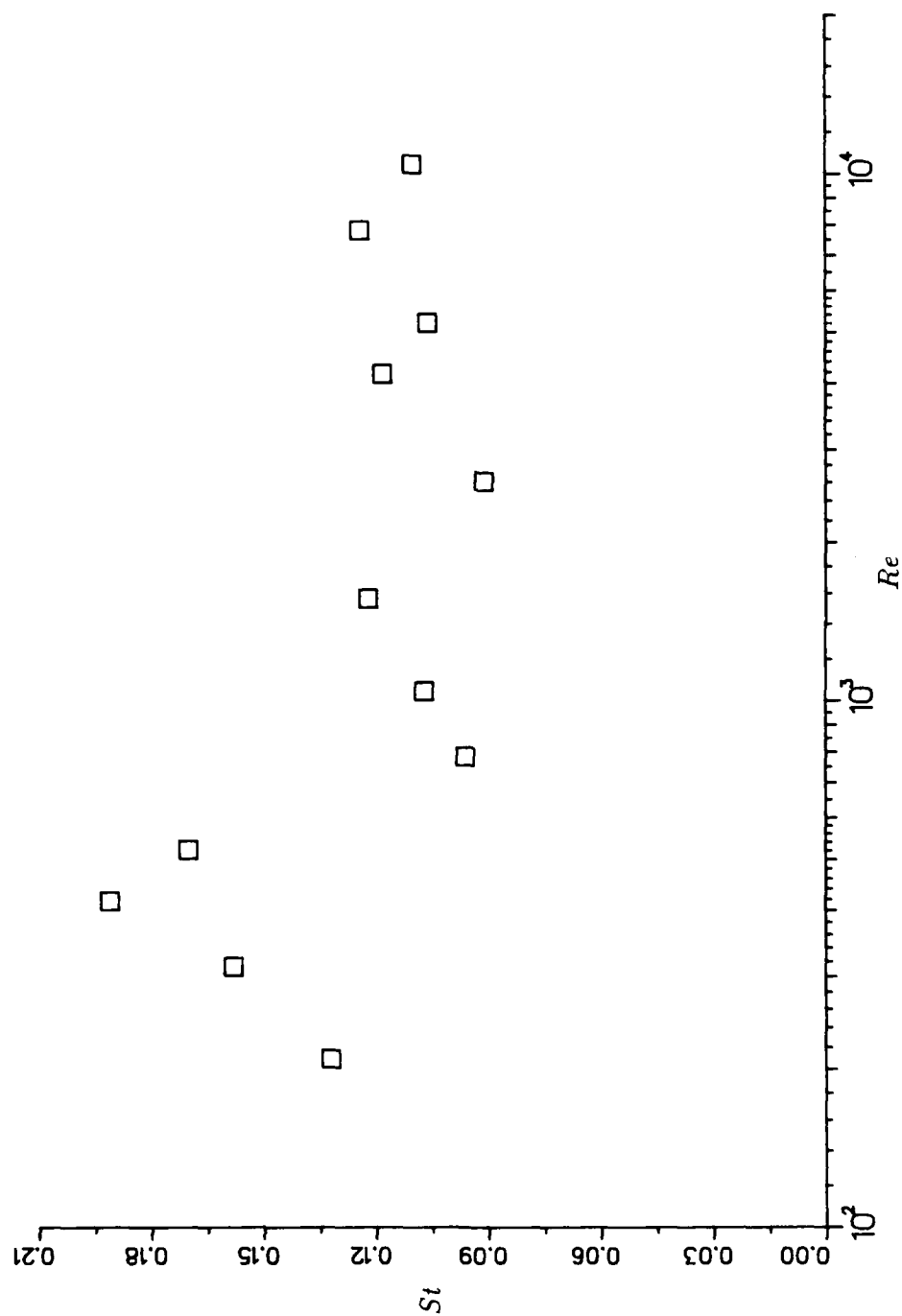FIGURE 7.5: Strouhal Number vs. Reynolds Number for $\beta = 1$.

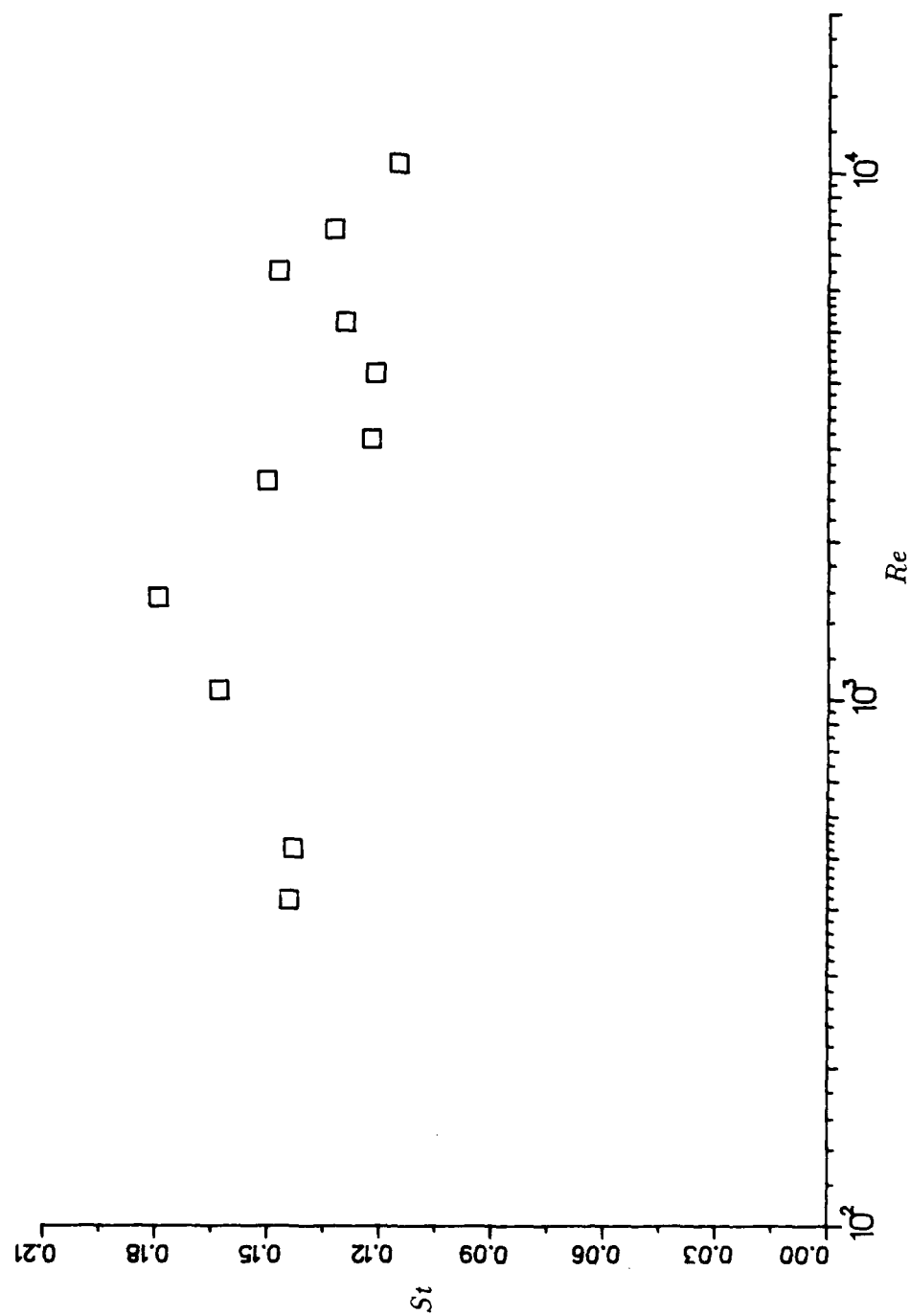FIGURE 7.6: Strouhal Number vs. Reynolds Number for $\beta = 2$.

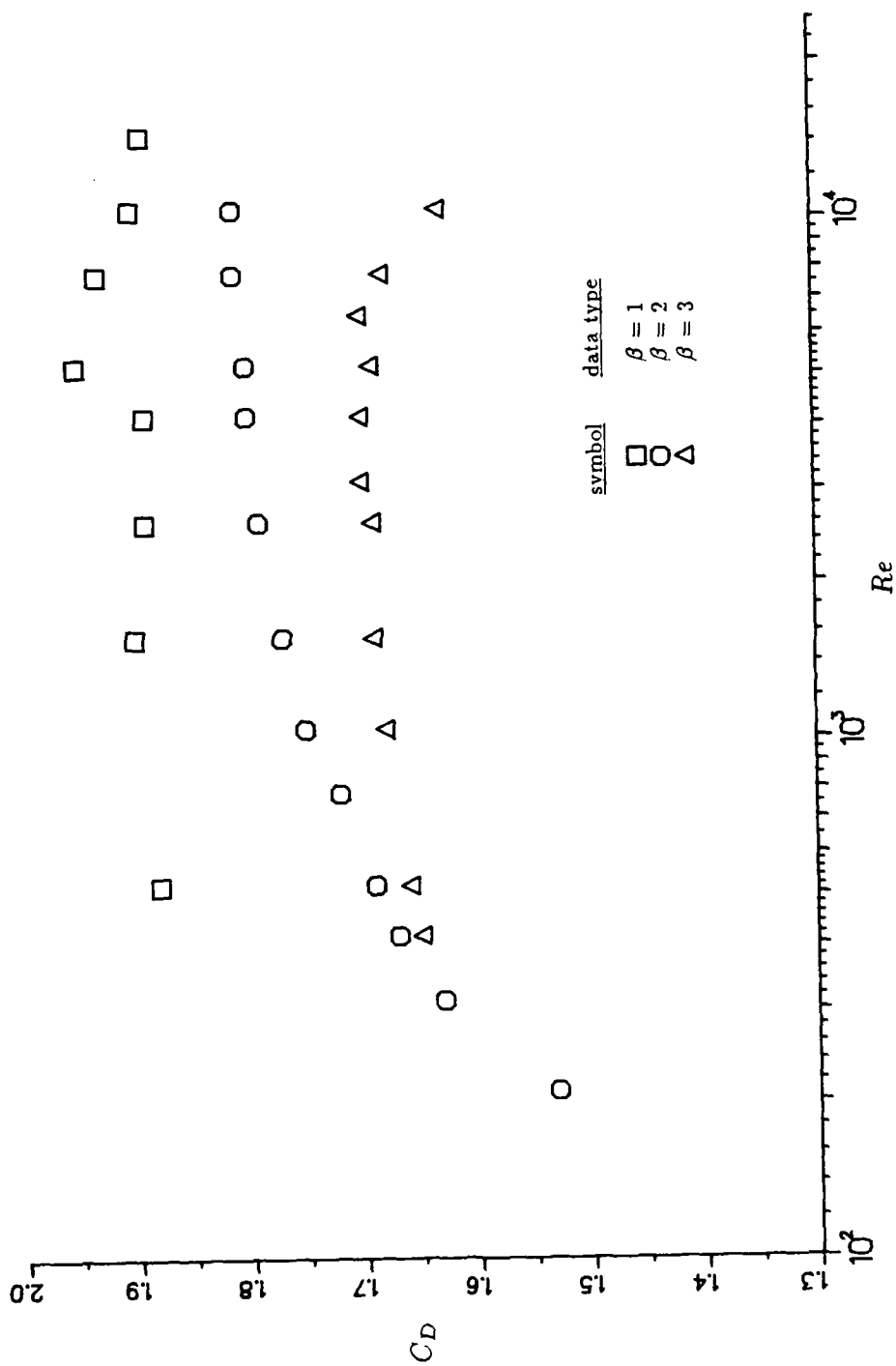FIGURE 7.7: Strouhal Number vs. Reynolds Number
for $\beta = 3$.

FIGURE 7.8: Variation in the Drag Coefficient with Cylinder Aspect Ratio.

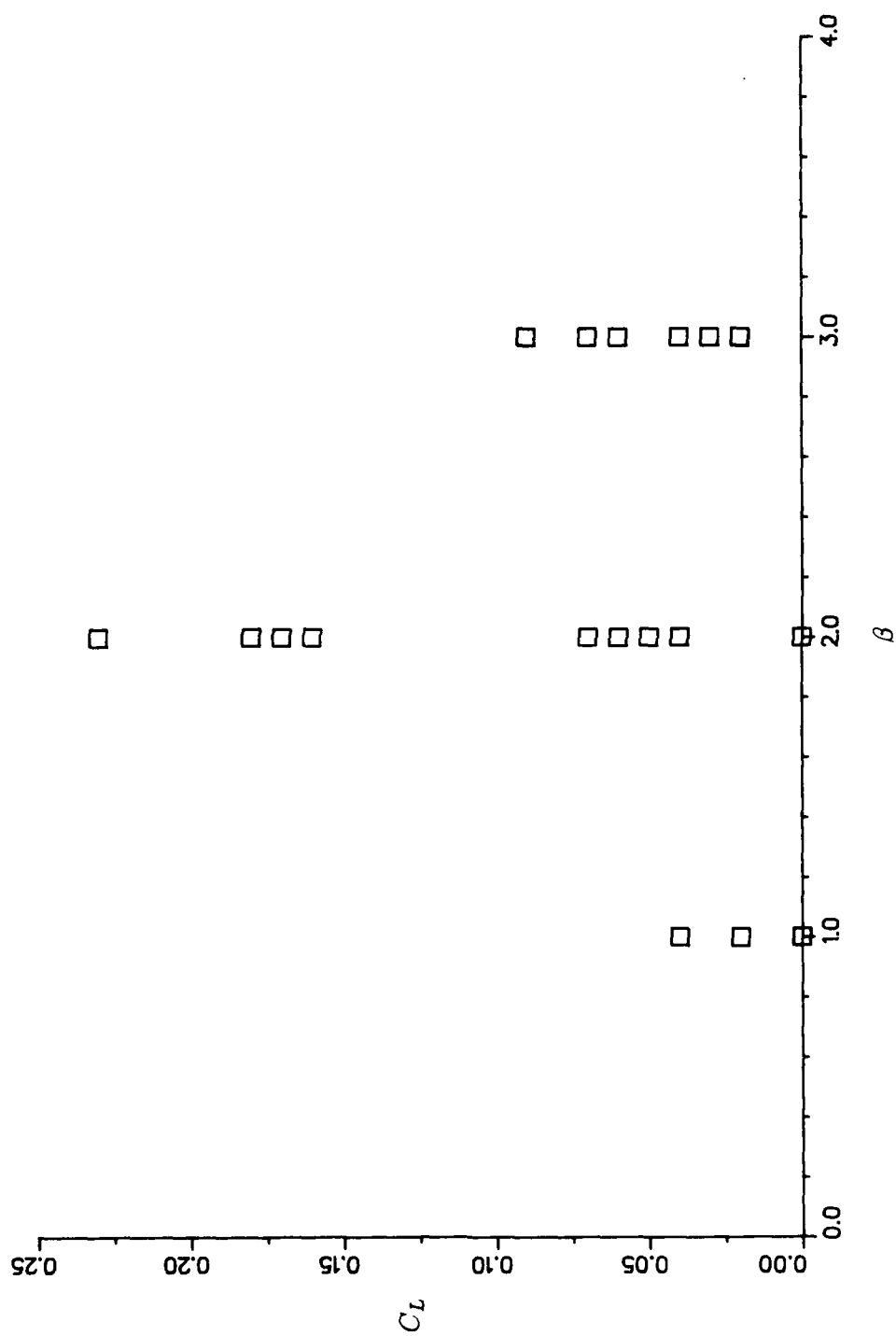FIGURE 7.9: Variation in the Drag Coefficient with Reynolds Number.

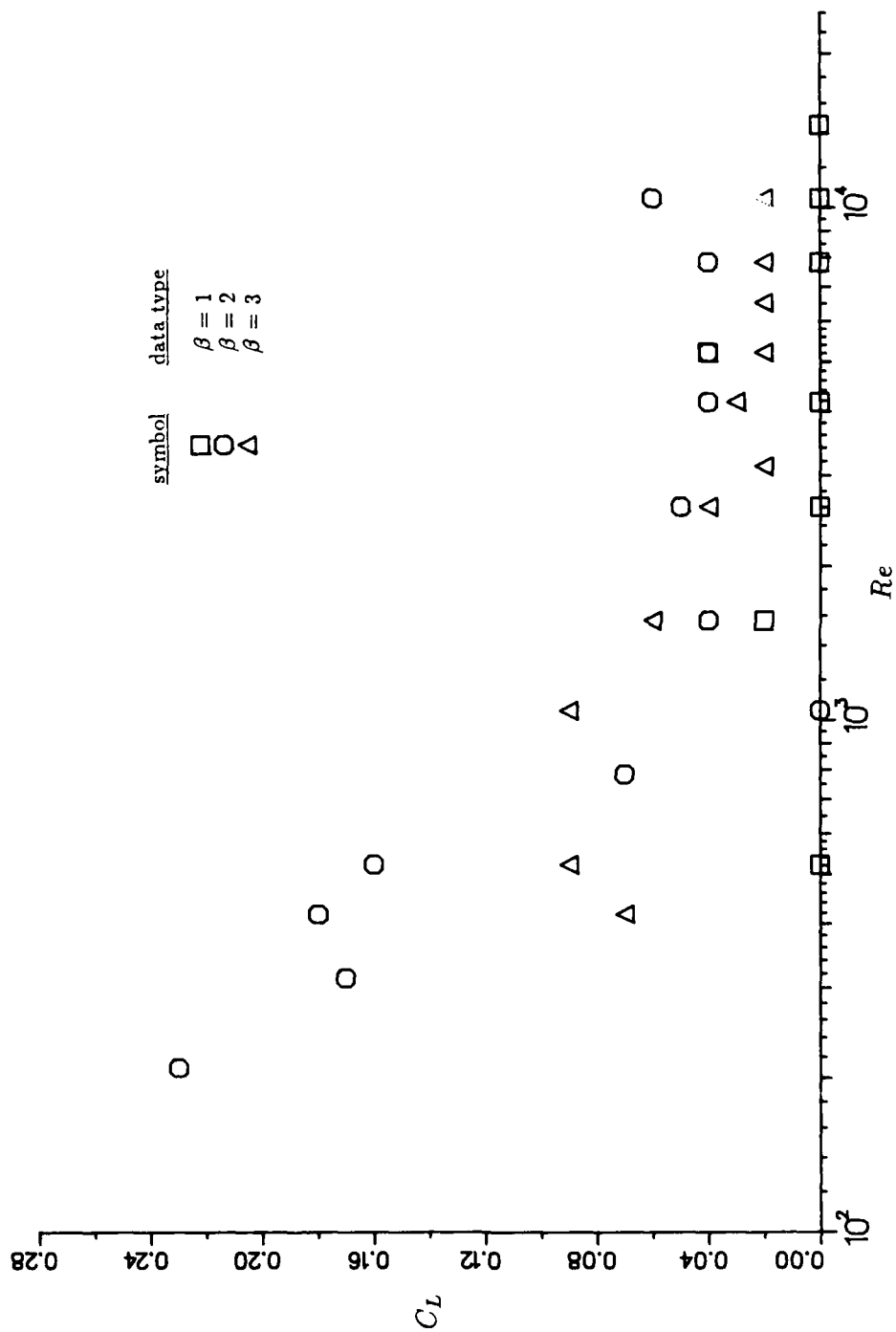FIGURE 7.10: Variation in the Lift Coefficient with Cylinder Aspect Ratio.

111

FIGURE 7.11: Variation in the Lift Coefficient with Reynolds Number.

CHAPTER VIII

CONCLUSIONS

This study proposed to demonstrate the ability to predict the phenomena of vortex shedding from various two–dimensional bodies. For every case tested with the exception of a flat plate on a ground plane, periodic vortex shedding was achieved.

For the initial case involving a flat plate in a uniform flow (Chapter V), the results were favorable. Predicted Strouhal numbers agreed well with experimental data. A calculation of pressures in the wake of the plate indicated a region behind the plate where the predicted pressures were much lower than the experimental data; however, the difference may be due to difficulties in experimentally measuring the pressures. Predictions of the drag also indicated deviations from the drag function provided by Roshko, but the accuracy of Roshko's function was unknown.

With respect to parameters affecting the solution of the finite–difference equations, some significant results were discovered. Refinement of the finite–difference grid yielded only a slight improvement in the prediction of pressure distributions, and actually hampered the prediction of Strouhal numbers. The inclusion of turbulence was found to have very little effect, and was subsequently excluded from the solution process.

112

The prediction of vortex shedding from a flat plate near a ground plane also yielded favorable results. The comparison of predicted Strouhal numbers with an empirically derived function demonstrated the ability to predict general trends in the shedding frequency. Quantitatively, there were significant differences in the prediction and the empirical function; however, this may be attributable to the fact that the prediction was two-dimensional while the function was derived for a three-dimensional case. Also, the expected increase in the aerodynamic force coefficients as the body approached the ground plane were accurately predicted.

Finally, the prediction of vortex shedding from rectangular cylinders was successful. Strouhal numbers for cylinders of differing aspects ratios were predicted with reasonable accuracy. This prediction also properly included the discontinuity in the plots of Strouhal number versus Reynolds number for cylinders with aspect ratios in the range $2 \leq \beta \leq 3$. Unfortunately, the flow pattern that gives rise to this discontinuity was not clearly apparent. Predictions of the drag coefficient on the cylinder compare well with previous studies; however, the lift coefficient behaves in a manner contrary to prior indications.

BIBLIOGRAPHY

Birkhoff, Garrett and Zarantonello, E. H. (1957). Jets, Wakes, and Cavities. Academic Press Inc., New York.

Calvert, J. R. (1967). "Experiments on the Flow Past an Inclined Disk," Journal of Fluid Mechanics 29, pp. 691–703.

Carroll, George W. (1980). "Experimental and Theoretical Investigation of Three-Dimensional Turbulent Mixing in Jets and Ducts," Ph. D. Thesis, University of London.

Carroll, G. W., Maxwell, T. T., and Sun, R. L. (1985). "Flow Over Radiator and Condenser — 2 Dimensional." American Computing Inc., Alabama. Manual.

Daily, James W. and Harleman, Donald R. F. (1966). Fluid Dynamics. Addison-Wesley Publishing Company, Reading, Massachusetts.

Davis, R. W. and Moore, E. F. (1982). "A Numerical Study of Vortex Shedding From Rectangles," Journal of Fluid Mechanics 116, pp. 475–506.

Ericsson, L. E. and Reding, J. P. (1981). "Steady and Unsteady Vortex-Induced Asymmetric Loads on Slender Vehicles," Journal of Spacecraft and Rockets 18, pp. 97–109.

Griffin, Owen M. (1981). "OTEC Cold Water Pipe Design for Problems Caused by Vortex-Excited Oscillations," Ocean Engineering 8, pp. 129–209.

Griffin, Owen M. (1985). "Vortex Shedding From Bluff Bodies in a Shear Flow: A Review," Journal of Fluids Engineering 107, pp. 298–306.

Karamcheti, Krishnamurty (1980). Principles of Ideal-Fluid Aerodynamics. Robert E. Krieger Publishing Company, Malabar, Florida.

Laneville, A. and Yong, Lü Zhi (1983). "Mean Flow Patterns Around Two-Dimensional Rectangular Cylinders and Their Interpretation," Wind Engineering 1983, Proceedings of the Sixth International Conference on Wind Engineering.

Matty, Rosemary R. (1979). "Vortex Shedding From Square Plates Near a Ground Plane: An Experimental Study," M. S. Thesis, Texas Tech University.

Nallasamy, M. (1985). "A Critical Evaluation of Various Turbulence Models as Applied to Internal Fluid Flows," NASA Technical Paper 2474.

Okajima, Atsushi (1982). "Strouhal Numbers of Rectangular Cylinders," Journal of Fluid Mechanics 123, pp. 379–398.

Patankar, Suhas V. (1980). Numerical Heat Transfer and Fluid Flow. Hemisphere Publishing Corporation, New York.

Podolny, Walter Jr. and Scalzi, John B. (1976). Construction and Design of Cable-Stayed Bridges. John Wiley and Sons, New York.

Rajabi, F., Zedan, M. F., and Mangiavacchi, A. (1984). "Vortex Shedding Induced Dynamic Response of Marine Risers," Journal of Energy Resources Technology 106, pp. 214–221.

Roache, Patrick J. (1976). Computational Fluid Dynamics. Hermosa Publishers, Albuquerque.

Rodi, Wolfgang (1984). Turbulence Models and Their Application in Hydraulics — A State of the Art Review, Second Revised Edition. International Association for Hydraulic Research, The Netherlands.

Roshko, Anatol (1953). "On the Development of Turbulent Wakes From Vortex Streets," NACA Technical Note 2913.

Roshko, Anatol (1954). "A New Hodograph for Free-Streamline Theory," NACA Technical Note 3168.

Roshko, Anatol (1954). "On the Drag and Shedding Frequency of Two-Dimensional Bluff Bodies," NACA Technical Note 3169.

Sarpkaya, T. (1979). "Vortex-Induced Oscillations: A Selective Review," Journal of Applied Mechanics 46, pp. 241–258.

Schlichting, Hermann (1979). Boundary-Layer Theory, Seventh Edition. McGraw-Hill Book Company, New York.

Sirovich, L. and Lim, C. (1985). "Comparison of Experiment with the Dynamics of the von Kármán Vortex Trail," Studies of Vortex Dominated Flows, Proceedings of the Symposium on Vortex Dominated Flows Held July 9-11, 1985, at NASA Langley Research Center, Hampton, Virginia, pp. 44–60.

Stone, Herbert L. (1968). "Iterative Solution of Implicit Approximations of Multidimensional Partial Differential Equations," SIAM Journal on Numerical Analysis 5, pp. 530–558.

Strickland, James H., Matty, Rosemary R., and Barton, Gregory H. (1980). "Vortex Shedding From Square Plates Perpendicular to a Ground Plane," AIAA Journal 18, pp. 715–716.

Swanson, J. C. and Spaulding, M. L. (1978). "Three Dimensional Numerical Model of Vortex Shedding From a Circular Cylinder," Nonsteady Fluid Dynamics: The Winter Annual Meeting of the American Society of Mechanical Engineers, December 10–15, 1978, San Francisco. The American Society of Mechanical Engineers, New York.

Van Dyke, Milton (1982). An Album of Fluid Motion. The Parabolic Press, Stanford, California.

White, Frank M. (1979). Fluid Mechanics. McGraw–Hill Book Company, New York.

Younis, B. A. (1988). "On Modeling the Vortex Shedding From Bluff Bodies in Laminar and Turbulent Streams," Presented at the Seventh International Conference on Offshore Mechanics and Arctic Engineering, Houston, Texas, February 7–12, 1988.
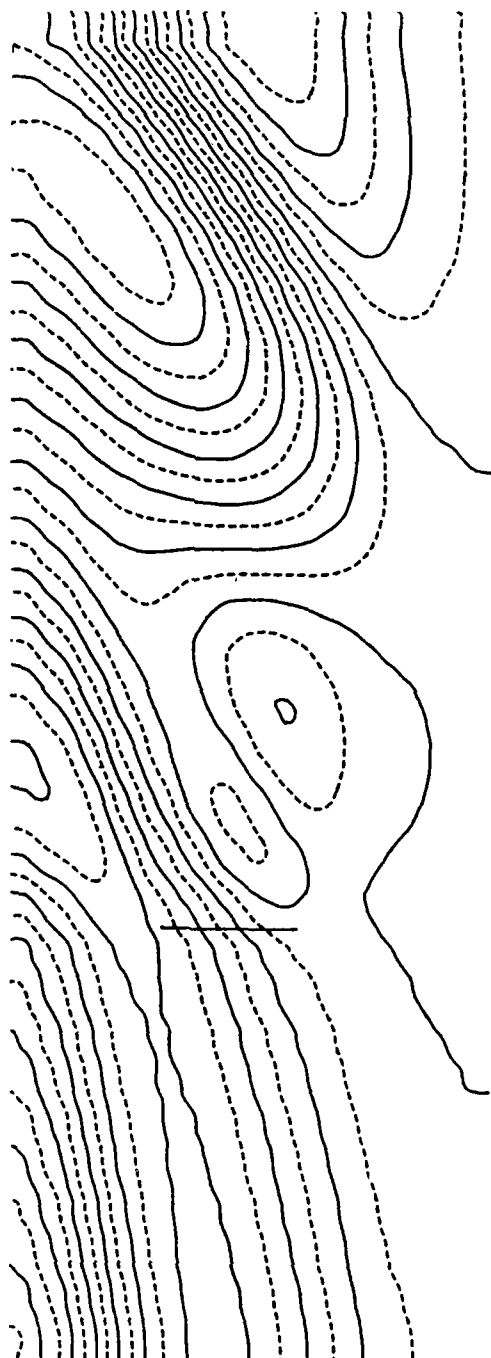
APPENDIX

PLOTS OF STREAMLINES

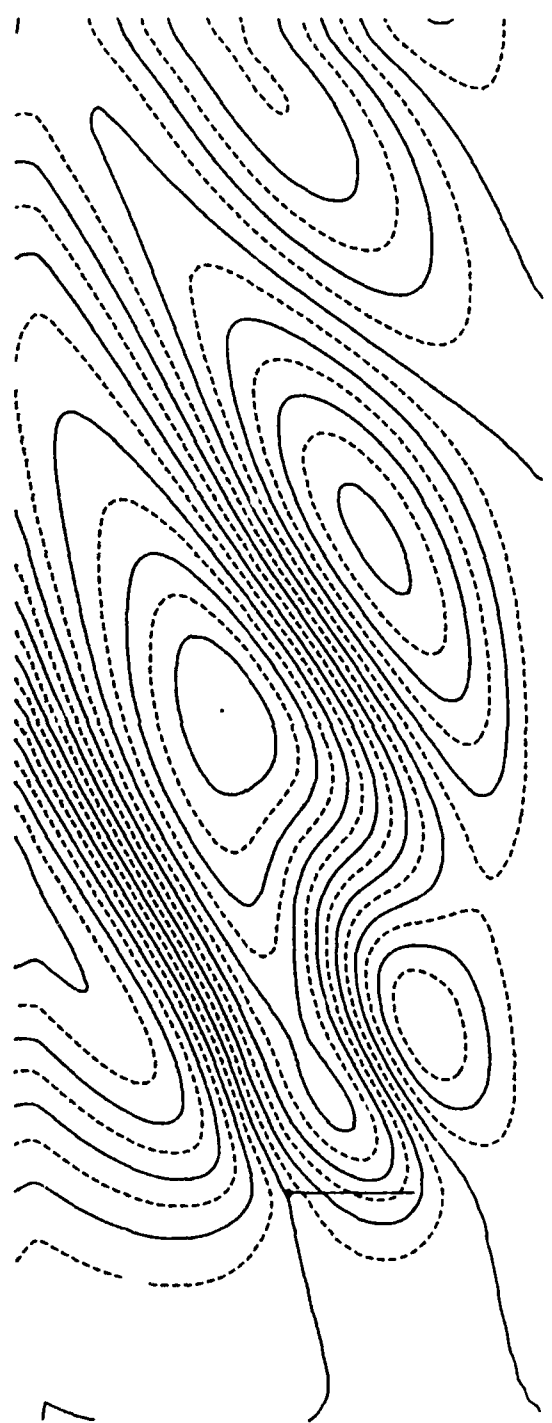FIGURE A.1: Streamlines for a Flat Plate.

FIGURE A.2: Streamlines for a Flat Plate
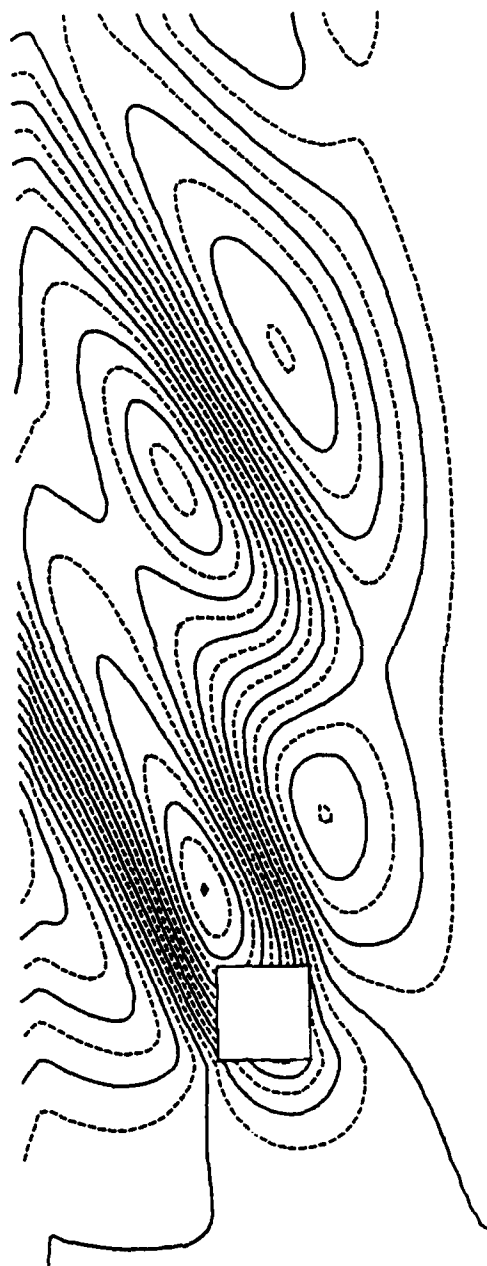Near a Ground Plane ($\lambda = 1$).

FIGURE A.3: Streamlines for a Rectangular Cylinder with $\beta = 1$.
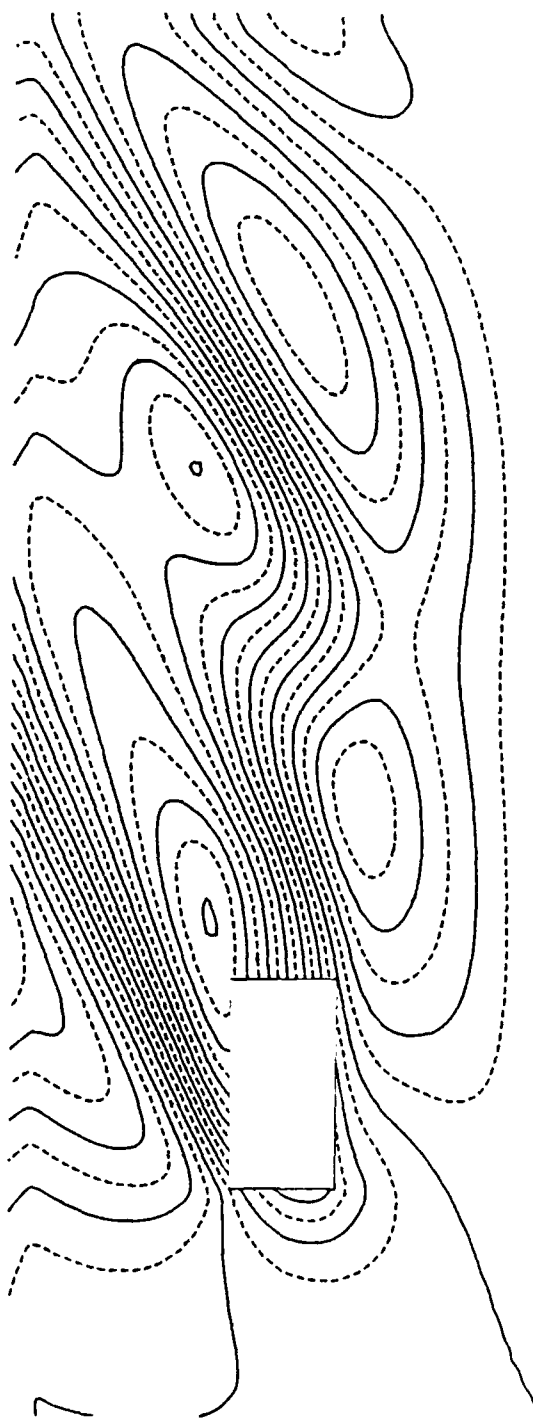
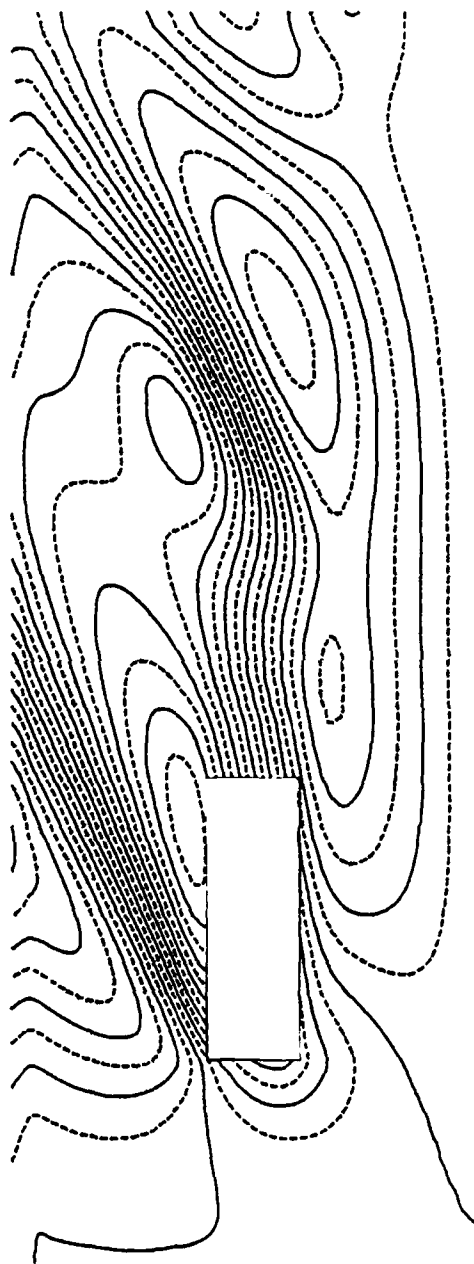FIGURE A.4: Streamlines for a Rectangular Cylinder
with $\beta = 2$.

FIGURE A.5: Streamlines for a Rectangular Cylinder with $\beta = 3$.